https://doi.org/10.15388/vu.thesis.827
https://orcid.org/0000-0001-6829-3549

VILNIUS UNIVERSITY
CENTER FOR PHYSICAL SCIENCES AND TECHNOLOGY

Andrea Zelioli

Growth and Investigation of A_3B_5 Quantum Structures for VECSELs

DOCTORAL DISSERTATION

Natural Sciences,
Physics (N 002)

VILNIUS 2025

This dissertation was prepared between 2021 and 2025 at State Research Institute Center for Physical Sciences and Technology

Academic Supervisor:
Assoc. Prof. Dr. Renata Butkutė (State Research Institute Center for Physical Sciences and Technology, Natural Sciences, Physics – N 002).

Dissertation Defense Panel:

Chairman – Prof. Dr. Ramūnas Aleksiejūnas (Vilnius University, Natural Sciences, Physics – N 002).

Members:
Dr. Arūnas Kadys (Vilnius University, Technological Sciences, Materials engineering – T 008),
Prof. Dr. Nerija Žurauskienė (State Research Institute Center for Physical Sciences and Technology, Natural Sciences, Physics – N 002),
Prof. Dr. Tadas Malinauskas (Vilnius University, Technological Sciences, Materials engineering – T 008),
Prof. Dr. Jiao Yuqing (Eindhoven University of Technology, Technological Sciences, Materials engineering – T 008).

The dissertation shall be defended at a public meeting of the Dissertation Defense Panel at 14:00 on 2025/10/06 in conference hall A101 of the Center for Physical Sciences and Technology
Address: Saulėtekio av. 3, NFTMC, Conference Hall A101, Vilnius, Lithuania.
Tel. +370 5 264 8884; email: office@ftmc.lt

The text of this dissertation can be accessed at the Vilnius University Library, as well as on the website of Vilnius University: www.vu.lt/naujienos/ivykiu-kalendorius.

https://doi.org/10.15388/vu.thesis.827
https://orcid.org/0000-0001-6829-3549

VILNIAUS UNIVERSITETAS
FIZINIŲ IR TECHNOLOGIJOS MOKSLŲ CENTRAS

Andrea Zelioli

A_3B_5 kvantinių darinių formavimas ir tyrimas VECSEL tipo lazeriams

DAKTARO DISERTACIJA

Gamtos mokslai,
Fizika (N 002)

VILNIUS 2025

Disertacija rengta 2021–2025 metais Valstybiniame mokslinių tyrimų institute Fizinių ir technologijos mokslų centre

Mokslinė vadovė:
doc. dr. Renata Butkutė (Fizinių ir technologijos mokslų centras, gamtos mokslai, fizika – N 002).

Gynimo taryba:

Pirmininkas – prof. dr. Ramūnas Aleksiejūnas (Vilniaus universitetas, gamtos mokslai, fizika – N 002).

Nariai:
dr. Arūnas Kadys (Vilniaus universitetas, technologijos mokslai, medžiagų inžinerija – T 008),
prof. dr. Nerija Žurauskienė (Fizinių ir technologijos mokslų centras, gamtos mokslai, fizika – N 002),
prof. dr. Tadas Malinauskas (Vilniaus universitetas, technologijos mokslai, medžiagų inžinerija – T 008),
prof. dr. Jiao Yuqing (Eindhoveno technologijos universitetas, technologijos mokslai, medžiagų inžinerija – T 008).

Disertacija ginama viešame Gynimo tarybos posėdyje 2025 m spalio 6 d. 14 val. Valstybinio mokslinių tyrimų instituto Fizinių ir technologijos mokslų centro konferencijų saleie A101.
Adresas:
Saulėtekio al. 3, Vilnius, tel. +37052648884; el. paštas: office@ftmc.lt
Disertaciją galima peržiūrėti Vilniaus universiteto bibliotekoje ir VU interneto svetainėje adresu: https://www.vu.lt/naujienos/ivykiu-kalendorius

ACKNOWLEDGEMENTS

This dissertation would not have been possible without the people who have supported me along the way. I am deeply grateful to the *BisButkutukas* group for making these years both productive and enjoyable. I especially thank my colleague Aivaras Špokas for his friendship, collaboration, and for always being ready to discuss ideas, no matter how small or complex. My deepest gratitude goes to my supervisor Renata Butkutė, whose guidance, patience, and encouragement have shaped not only this work, but also my growth as a researcher.

I also owe my heartfelt thanks to my family. Your love, understanding, and endless support have carried me through the challenges of these many years of study. Without you, this achievement would not have been possible.

Contents

LIST OF ABBREVIATIONS

Δ_{SO} Spin-Orbit Splitting Energy

µPL Micro-Photoluminescence

1D One-dimensional

AFM Atomic Force Microscopy

BAC Band Anticrossing

BandiT Band-edge Thermometry

BEP Beam Equivalent Pressure

BEPR Beam Equivalent Pressure Ratio

BFM Beam Flux Monitor

CW Continuous Wave

DBR Distributed Bragg Reflector

DFT Density Functional Theory

DIC Differential Interference Contrast

FWHM Full Width at Half Maximum

g-r Generation-Recombination

HH Heavy Hole

HR-TEM High-Resolution Transmission Electron Microscopy

HT High Temperature

IQE Internal Quantum Efficiency

IR Infrared

LD Laser Diode

LED Light Emitting Diode

LH Light Hole

LT Low Temperature

MBE Molecular Beam Epitaxy

MD Misfit Dislocations

MOVPE Metal Organic Vapor Phase Epitaxy

MQW Multiple Quantum Well

NIR Near-Infrared

PGB Parabolically Graded Barrier

PL Photoluminescence

QD Quantum Dot

QW Quantum Well

RHEED Reflection High-Energy Electron Diffraction

RTPL Room-Temperature Photoluminescence

SI Semi-Insulating

SWIR Short-Wave Infrared

TAAR Trap-assisted Auger Recombination

TDPL Temperature-Dependent Photoluminescence

TEM Transmission Electron Microscopy

UHV Ultra-High Vacuum

VCSEL Vertical-Cavity Surface-Emitting Laser

VECSEL Vertical-External-Cavity Surface-Emitting Laser

XRD X-ray Diffraction

INTRODUCTION

Vertical-External-Cavity Surface-Emitting Lasers (VECSELs) are a class of optically pumped semiconductor lasers that have attracted significant interest due to their combination of high beam quality, wavelength tunability, and power scalability. Unlike electrically pumped Vertical-Cavity Surface-Emitting Lasers (VCSELs), which are limited by the need for top- and bottom-contact Distributed Bragg Reflectors (DBRs) and by a constrained emission area, VECSELs employ an external cavity mirror instead of the top DBR. This geometry removes the need for current injection through the lasing path, enables optical pumping, and provides direct access to the cavity for advanced optical functionalities.

One of the key advantages of VECSELs is their scalability in output power. Optical pumping allows for a larger gain area, enabling output powers from hundreds of milliwatts to beyond 100 W, while preserving diffraction-limited beam quality. Their external cavity design also facilitates straightforward integration of intracavity components, such as saturable absorbers for mode-locking, nonlinear crystals for frequency conversion, and multiple gain chips for beam combining and power scaling. These features make VECSELs highly attractive for applications in industrial processing, biomedical imaging, optical communication, quantum information technologies, and laser display systems.

From a materials perspective, the most widely used VECSEL structures for Near-Infrared (NIR) emission employ InGaAs/GaAs Multiple Quantum Wells (MQWs) as the active region, positioned at the antinodes of the standing optical field. Alternating GaAs/AlAs layers are typically chosen for the DBR mirrors due to their high refractive index contrast and excellent lattice matching. InGaAs-based VECSELs operate reliably in the 920–1100 nm spectral range. For example, 976 nm VECSELs are commonly used for frequency-doubling to 488 nm or as pump sources for erbium-doped fiber amplifiers (EDFAs).

However, extending emission wavelengths further into the infrared requires higher In content in the InGaAs Quantum Wells (QWs), which increases lattice mismatch with GaAs substrates. The resulting strain accumulation promotes dislocation formation, intro-

ducing non-radiative recombination centers that reduce efficiency and generate localized heating, ultimately limiting output power and device stability. Various strain-compensation strategies have been investigated, including the incorporation of GaAsP layers or dilute nitrides, but these approaches introduce added complexity and growth challenges.

GaAsBi has therefore been proposed as a promising alternative gain medium. Incorporating Bi into GaAs reduces the bandgap by approximately 60–90 meV per percent of Bi, enabling emission beyond 1100 nm with much lower strain compared to In-rich InGaAs. Moreover, GaAsBi exhibits large spin–orbit splitting, which can suppress Auger recombination and inter-valence band absorption when the Bi content exceeds 10.5 %, thereby improving efficiency. GaAsBi is also less sensitive to temperature variations, providing a route toward thermally stable NIR sources.

Nonetheless, the growth of GaAsBi QWs is challenging. High Bi incorporation requires low substrate temperatures and precise As/Ga flux ratios during Molecular Beam Epitaxy (MBE) growth. These conditions often lead to increased defect densities, alloy disorder, and reduced luminescence efficiency. Extensive optimization of the growth parameters is therefore essential. A critical part of this work is the systematic investigation of the optical and material quality of GaAsBi MQWs for VECSEL applications, focusing on Internal Quantum Efficiency (IQE) characterization and the identification of recombination mechanisms, particularly trap-assisted and other non-radiative channels.

In summary, while VECSELs offer compelling advantages, wavelength flexibility, high power scalability, excellent beam quality, and cavity accessibility their performance depends strongly on the quality of the epitaxial structures. For InGaAs-based devices, strain management remains the main challenge, while for GaAsBi-based designs, reducing defect-related losses is critical. The work presented in this dissertation addresses both aspects, advancing the development of efficient and thermally stable VECSELs across the NIR spectrum.

Goal of the Research

The main goal of this work is the optimization of GaAsBi-based MQWs for application in NIR VECSELs emitting in the 1000–1200 nm range. To achieve this goal, the following steps were defined:

1. Optimization of InGaAs-based MQWs growth by addressing three main aspects: the effects of post-growth annealing, the mitigation of lattice-mismatch-induced dislocation formation, and the reduction of carrier thermalization in the wells.

2. Optimization of technological parameters for GaAsBi-based MQWs and device growth. This includes identifying a suitable growth window that enables precise control of Bi incorporation and determining the optimal conditions for fabricating complete devices.

3. Development of a reliable method to evaluate the IQE of GaAsBi structures, enabling a detailed investigation of the dominant recombination pathways in this material system.

4. Fabrication and testing of Laser Diodes (LDs) based on GaAsBi MQWs with different barrier geometries, in order to assess their suitability and performance for VECSEL applications.

5. Design, growth, and characterization of complete VECSEL structures based on both InGaAs and GaAsBi MQWs, followed by testing within the capabilities of the available experimental setup.

Novelty

1. I demonstrated that spatially resolved Room-Temperature Photoluminescence (RTPL) mapping is an effective method for detecting and analyzing Misfit Dislocationss (MDs) in MQW structures.

2. I investigated stress accumulation in strained MQW systems and introduced a novel alternating-barrier-thickness design,

enabling the realization of thinner and more efficient VECSELs.

3. I identified the dominant recombination channels in GaAsBi and proposed a modified ABC model for more accurate IQE determination.

4. I fabricated LDs with two different barrier designs, revealing the current leakage mechanisms associated with Low Temperature (LT)-grown GaAsBi and GaAs barriers.

5. I designed, grew, and characterized the first GaAsBi-based VECSEL, demonstrating lasing from a large pumped area without the need for additional cooling.

Statements to be Defended

1. Precise control of indium content and well thickness in InGaAs MQW structures epitaxially grown on GaAs enables high emission uniformity across large substrate areas, demonstrating their feasibility for wafer-scale photonic device production.

2. Reproducible incorporation of up to 10 % bismuth into the GaAs lattice can be achieved in multiple quantum well structures grown by molecular beam epitaxy under temperature-limited kinetics.

3. An innovative design of GaAsBi-based MQWs with parabolically graded AlGaAs barriers, combined with thermal engineering, reduces the lasing threshold at room temperature by at least 30 % and enhances stimulated emission by more than an order of magnitude.

4. A novel VECSEL architecture employing GaAsBi QW pairs with alternating GaAs barrier thickness enables an increase in active device area, improves pumping efficiency, and simplifies heat management.

Contribution of the Author

The author contributed extensively to the design, growth, and simulation of the investigated structures, and was responsible for data analysis and interpretation. The author also participated in the preparation and discussion of all related manuscripts and actively disseminated the results through presentations at international conferences.

LIST OF PUBLICATIONS

On the Dissertation Topic

[A1] Pūkienė S., Jasinskas A., **Zelioli A.**, Stanionytė S., Bukauskas V., Čechavičius B. and Butkutė R. Influence of an ultra-thin buffer layer on the growth and properties of pseudomorphic GaAsBi layers. Lithuanian Journal of Physics, 62(2). 10.3952/physics.v62i2.4742

[A2] Armalytė S., Glemža J., Jonkus V., Pralgauskaitė S., Matukas J., Pūkienė S., **Zelioli A.**, Dudutienė E., Naujokaitis A. and Bičiūnas A. Low-Frequency Noise Characteristics of (Al, Ga)As and Ga(As, Bi) Quantum Well Structures for NIR Laser Diodes. Sensors 2023, 23, 2282. 10.3390/s23042282

[A3] Štaupienė A., **Zelioli A.**, Špokas A., Vaitkevičius A., Čechavičius B., Butkutė R., and Dudutienė E. Internal Quantum Efficiency of GaAsBi MQW structure for VECSELs. Applied Physics Letters 125, 221102 (2024), 10.1063/5.0234853

[A4] **Zelioli A.**, Žuvelis J., Cibulskaitė U., Špokas A., Dudutienė E., Vaitkevičius A., Stanionytė S., Čechavičius B., Butkutė R. Optimization of AlGaAs barrier for InGaAs quantum wells emitting in the near infrared. Lithuanian Journal of Physics. 64. (2024), 10.3952/physics.2024.64.4.5

[A5] Glemža J., Špokas A., **Zelioli A.**, Kamarauskas M., Bičiūnas A., Čechavičius B., Spigulis J., Chiu Y.-J., Pralgauskaitė S., Matukas J., Butkutė R. Quality Evaluation of NIR Laser Diodes for Medical Application using Low-frequency Noise Characterization. Infrared Physics and Technology (2025). 10.1016/j.infrared.2025.105794

[A6] Špokas A., **Zelioli A.**, Bičiūnas A., Čechavičius B., Glemža J., Pralgauskaitė S., Kamarauskas M., Bukauskas V., Spigulis J., Chiu Y.J., Matukas J., Butkutė R. Optimising (Al, Ga)(As, Bi) quantum well laser structures for

reflectance mode pulse oximetry. Micromachines (2025). 10.3390/mi16050506

[A7] **Zelioli A.**, Špokas A., Čechavičius B., Talaikis M., Stanionytė S., Vaitkevičius A., Čerškus A., Dudutienė E., Butkute R. (2024). In-depth investigation of emission homogeneity of InGaAs multiple quantum wells using spatially resolved spectroscopy. 10.21203/rs.3.rs-4642946/v1 . (Submitted)

Conference Presentations

[C1] **A. Zelioli**, A. Jasinskas, S. Pūkienė, L. Jočionis, B. Čechavičius, E. Dudutienė, R. Butkutė, *GaInAs/GaAs quantum structures for NIR VECSEL.* 17th International conference on Advanced properties and processes in optoelectronics materials and systems (Apropos 17), 2020, September 30–October 01, Vilnius, Lithuania. (Poster)

[C2] **A. Zelioli**, A. Jasinskas, S. Pūkienė, L. Jočionis, B. Čechavičius, R. Butkutė, *Vertical-external-cavity surface-emitting-laser design and caracterization for near-infrared wavelength.* FizTeCh: 11-oji Fizinių ir technologijos mokslų centro doktorantų ir jaunųjų mokslininkų konferencija, 2021, October 20–21, Vilnius, Lithuania. (Oral presentation)

[C3] **A. Zelioli**, A. Jasinskas, A. Gajauskaitė, S. Pūkienė, L. Jočionis, E. Dudutienė, B. Čechavičius, R. Butkutė, *Optimization of GaInAs/GaAs quantum well technology for applications in near infrared vertical-external-cavity surface-emitting lasers.* Open Readings 2021: 64th International Conference for Students of Physics and Natural Sciences, 2021, March 16–29, Vilnius, Lithuania. (Poster)

[C4] M. Jokubauskaitė, E. Dudutienė, **A. Zelioli**, A. Pukinskas, S. Pūkienė, B. Čechavičius, R. Butkutė, *Influence of the design of parabolic AlGaAs barriers on the optical properties of GaAsBi quantum wells.* Advanced properties and processes in optoelectronic materials and systems (APROPOS 18), 2022, October 05–07, Vilnius, Lithuania. (Poster)

[C5] **A. Zelioli**, A. Jasinskas, S. Pūkienė, S. Keraitytė, A. Naujokaitis, M. Skapas, M. Jokubauskaitė, E. Dudutienė, A. Suchodolskis, B. Čechavičius, R. Butkutė, *Developement of GaAsBi/GaAs MQW technology for applications in NIR VECSELs.* Advanced materials and technologies: 24th International Conference-School, 2022, August 22–26, Palanga, Lithuania. (Poster)

[C6] **A. Zelioli**, A. Jasinskas, S. Pūkienė, S. Keraitytė, A. Naujokaitis, M. Skapas, M. Jokubauskaitė, E. Dudutienė, A. Suchodolskis, B. Čechavičius, R. Butkutė, *Growth of series samples for optimization of MQW MBE parameters.* FizTeCh: 12-oji Fizinių ir technologijos mokslų centro doktorantų ir jaunųjų mokslininkų konferencija, 2022, October 19–20, Vilnius, Lithuania. (Poster)

[C7] **A. Zelioli**, A. Pukinskas, A. Jasinskas, S. Pūkienė, S. Keraitytė, A. Naujokaitis, M. Skapas, M. Jokubauskaitė, E. Dudutienė, A. Suchodolskis, B. Čechavičius, R. Butkutė, *Optimization of quantum well growth technology for applications in near infrared vertical-external-cavity surface-emitting lasers.* Open Readings 2022: 65th International Conference for Students of Physics and Natural Sciences, 2022, March 15–18, Vilnius, Lithuania. (Oral presentation)

[C8] **A. Zelioli**, A. Pukinskas, A. Jasinskas, S. Pūkienė, S. Keraitytė, A. Naujokaitis, M. Skapas, M. Jokubauskaitė, E. Dudutienė, A. Suchodolskis, B. Čechavičius, R. Butkutė, *Optimization of A3B5 quantum well growth technology for applications in near infrared vertical-external-cavity surface-emitting.* E-MRS Fall Meeting 2022, 2022, September 19–22, Warsaw, Poland. (Oral presentation)

[C9] A. Štaupienė, A. Špokas, **A. Zelioli**, B. Čechavičius, S. Stanionytė, E. Dudutienė, R. Butkutė, *Investigation of photoluminescence efficiency of GaAsBi/GaAs quantum well structures.* FizTeCh2023: 13-oji Fizinių ir technologijos mokslų centro doktorantų ir jaunųjų mokslininkų konferencija, 2023, October 18–19, Vilnius, Lithuania. (Poster)

[C10] A. Butkutė, A. Špokas, **A. Zelioli**, B. Čechavičius, A. Čerškus, E. Dudutienė, R. Butkutė, *Towards understanding*

of the light emission efficiency of GaAsBi quantum wells. Advanced materials and technologies: 25nd International Conference-School, 2023, August 21–25, Palanga, Lithuania. (Poster)

[C11] A. Špokas, **A. Zelioli**, K. Mažeika, A. Vaitkevičius, S. Stanionytė, B. Čechavičius, E. Dudutienė, R. Butkutė, *Optimization of GaAsBi rectangular QWs for emission at 1–1.2 μm.* Advanced materials and technologies: 25nd International Conference-School, 2023, August 21–25, Palanga, Lithuania. (Poster)

[C12] **A. Zelioli**, A. Pukinskas, S. Keraitytė, A. Vaitkevičius, S. Stanionytė, M. Jokubauskaitė, B. Čechavičius, A. Čerškus, E. Dudutienė, R. Butkutė, *Investigation of large area PL emission from InGaAs/GaAs multi-quantum wells for VECSEL fabrication.* Advanced materials and technologies: 25nd International Conference-School, 2023, August 21–25, Palanga, Lithuania. (Poster)

[C13] A. Špokas, **A. Zelioli**, K. Mažeika, A. Vaitkevičius, S. Stanionytė, A. Čerškus, B. Čechavičius, E. Dudutienė, R. Butkutė, *Development of GaAsBi MQWs technology for NIR emitters.* COST action CA20116 OPERA European network for innovative and advanced epitaxy: Workshop "Application-oriented material development", 2023, September 12–14, Bucharest-Magurele, Romania. (Poster)

[C14] **A. Zelioli**, A. Pukinskas, S. Keraitytė, A. Vaitkevičius, S. Stanionytė, M. Jokubauskaitė, B. Čechavičius, A. Čerškus, E. Dudutienė, R. Butkutė, *Photoluminescence mapping of InGaAs/GaAs multi-quantum well system for vecsel fabrication.* Open Readings 2023: 66th International Conference for Students of Physics and Natural Sciences, 2023, April 18–21, Vilnius, Lithuania. (Oral presentation)

[C15] A. Špokas, **A. Zelioli**, G. Petrusevičius, M. Iršėnas, A. Vaitkevičius, S. Stanionytė, A. Čerškus, B. Čechavičius, E. Dudutienė, R. Butkutė, *GaAsBi stačiakampių kvantinių duobių auginimo technologijos optimizavimas artimosios infraraudonosios srities emiteriams.* 45-oji Lietuvos nacionalinė

fizikos konferencija, 2023, October 25–27, Vilnius, Lithuania. (Poster)

[C16] **A. Zelioli**, A. Špokas, K. Mažeika, M. Jokubauskaitė, A. Vaitkevičius, S. Stanionytė, B. Čechavičius, E. Dudutienė, R. Butkutė, *Mappings of large area PL emission from InGaAs/GaAs and GaAsBi/GaAs multi-quantum wells for VECSEL fabrication.* 45-oji Lietuvos nacionalinė fizikos konferencija, 2023, October 25–27, Vilnius, Lithuania. (Poster)

[C17] A. Špokas, G. Petrusevičius, **A. Zelioli**, A. Naujokaitis, M. Skapas, S. Stanionytė, M. Talaikis, A. Vaitkevičius, A. Suchodolskis, B. Čechavičius, E. Dudutienė, R. Butkutė, *Optimization of epitaxy conditions of InGaAs and GaAsBi multiple QuantumWell structures for applications in NIR VECSELs.* COST action CA20116 OPERA European network for innovative and advanced epitaxy: Workshop "Application-oriented material development", 2023, September 12–14, Bucharest-Magurele, Romania. (Poster)

[C18] E. Dudutienė, P. Šleiniūtė, M. Jokubauskaitė, A. Jasinskas, **A. Zelioli**, A. Pukinskas, S. Pūkienė, B. Čechavičius, S. Stanionytė, M. Skapas, A. Naujokaitis, R. Butkutė, *GaAsBi kvantinių struktūrų technologinių parametrų sąsajų su optinėmis savybėmis tyrimas.* Vienuoliktoji jaunųjų mokslininkų konferencija Fizinių ir technologijos mokslų tarpdalykiniai tyrimai, 2023, March 23, Vilnius, Lithuania. (Poster)

[C19] **A. Zelioli**, A. Špokas, G. Petrusevičius, K. Mažeika, M. Jokubauskaitė, A. Vaitkevičius, S. Stanionytė, B. Čechavičius, E. Dudutienė, R. Butkutė, *Minimization of the dislocation density in multiple quantum wells for the fabrication of nir vecsels.* FizTeCh2023: 13-oji Fizinių ir technologijos mokslų centro doktorantų ir jaunųjų mokslininkų konferencija, 2023, October 18–19, Vilnius, Lithuania. (Oral presentation)

[C20] **A. Zelioli**, A. Špokas, D. Gailevičius, E. Dudutienė, B. Čechavičius, A. Vaitkevičius, R. Butkutė, *Design, growth and characterization of Vertical-External-Cavity Surface-Emitting laser for NIR.* Apropos 19: Advanced properties and pro-

cesses in optoelectronic materials and systems, 2024, October 01–04, Vilnius, Lithuania. (Oral presentation)

[C21] **A. Zelioli**, A. Špokas, M. Krivičius, D. Gailevičius, E. Dudutienė, B. Čechavičius, R. Butkutė, *Design and fabrication of GaAsBi/GaAs and InGaAs/GaAs VECSELs for NIR emission.* 52nd "Jaszowiec" International School & Conference on the Physics of Semiconductors, 2024, June 15–21, Szczyrk, Poland. (Poster)

[C22] A. Štaupienė, A. Špokas, **A. Zelioli**, A. Vaitkevičius, B. Čechavičius, R. Butkutė, E. Dudutienė, *Internal quantum efficiency of GaAsBi/GaAs MQW structures.* FizTeCh2024: 14-oji Fizinių ir technologijos mokslų centro doktorantų ir jaunųjų mokslininkų konferencija, 2024, October 15–17, Vilnius, Lithuania. (Poster)

[C23] A. Štaupienė, M. Jokubauskaitė, A. Špokas, **A. Zelioli**, B. Čechavičius, E. Dudutienė, R. Butkutė, *Optical properties of InGaAs and GaAsBi quantum wells with graded AlGaAs barriers.* "Jaszowiec" 2024: 52nd International School & Conference on the Physics of Semiconductors, 2024, June 15–21, Szczyrk, Poland. (Poster)

[C24] M. Jokubauskaitė, A. Štaupienė, A. Špokas, **A. Zelioli**, E. Dudutienė, B. Čechavičius, R. Butkutė, *Influence of AlGaAs barrier design on photoluminescence of GaAsBi quantum structures.* Open Readings 2024: 67th International Conference for Students of Physics and Natural Sciences, 2024, April 23–26, Vilnius, Lithuania. (Poster)

[C25] A. Štaupienė, A. Špokas, **A. Zelioli**, B. Čechavičius, A. Vaitkevičius, E. Dudutienė, R. Butkutė, *Daugybinių GaAsBi kvantinių duobių skirtų galingiems lazeriams fotoliuminescencijos tyrimas.* 12-toji jaunųjų mokslininkų konferencija „Fizinių ir technologijos mokslų tarpdalykiniai tyrimai“, 2024, May 14, Vilnius, Lithuania. (Poster)

[C26] A. Štaupienė, A. Špokas, **A. Zelioli**, A. Vaitkevičius, R. Butkutė, E. Dudutienė, *Luminescence properties of GaAsBi MQWs for VECSELs.* Apropos 19: Advanced properties and processes in optoelectronic materials and systems, 2024, October 01–04, Vilnius, Lithuania. (Poster)

[C27] E. Dudutienė, M. Jokubauskaitė, A. Štaupienė, A. Špokas, **A. Zelioli**, B. Čechavičius, R. Butkutė, *Influence of different confinement on optical properties of single GaAsBi/AlGaAs quantum wells.* E-MRS 2024 Spring Meeting, 2024, May 27–31, Strasbourg, France. (Poster)

[C28] A. Štaupienė, M. Jokubauskaitė, A. Špokas, **A. Zelioli**, B. Čechavičius, S. Stanionytė, E. Dudutienė, R. Butkutė, *The influence of graded AlGaAs barriers on optical properties of GaAsBi single quantum wells.* OPERA: European Workshop on Innovative and Advanced Epitaxy, 2024, June 11–14, Vilnius, Lithuania. (Poster)

[C29] M. Jokubauskaitė, A. Štaupienė, E. Dudutienė, A. Špokas, **A. Zelioli**, B. Čechavičius, R. Butkutė, *Relation between photoluminescence intensity of InGaAs quantum wells and design of AlGaAs barriers.* FizTeCh2024: 14-oji Fizinių ir technologijos mokslų centro doktorantų ir jaunųjų mokslininkų konferencija, 2024, October 15–17, Vilnius, Lithuania. (Poster)

[C30] A. Štaupienė, A. Špokas, **A. Zelioli**, A. Vaitkevičius, R. Butkutė, E. Dudutienė, *Emission efficiency investigation of GaAsBi-based VECSEL.* Advanced materials and technologies: 26th International Conference-School, 2024, August 26–30, Palanga, Lithuania. (Poster)

[C31] A. Špokas, **A. Zelioli**, A. Bičiūnas, M. Kamarauskas, A. Čerškus, B. Čechavičius, E. Dudutienė, R. Butkutė, *GaAsBi.* Advanced materials and technologies: 26th International Conference-School, 2024, August 26–30, Palanga, Lithuania. (Oral presentation)

[C32] A. Štaupienė, A. Špokas, **A. Zelioli**, B. Čechavičius, S. Stanionytė, A. Vaitkevičius, E. Dudutienė, R. Butkutė, *Internal quantum efficiency of GaAsBi/GaAs quantum wells.* Open Readings 2024: 67th International Conference for Students of Physics and Natural Sciences, 2024, April 23–26, Vilnius, Lithuania. (Oral presentation)

[C33] A. Špokas, **A. Zelioli**, A. Bičiūnas, B. Čechavičius, A. Vaitkevičius, V. Bukauskas, M. Kamarauskas, E. Dudutienė,

R. Butkutė, *GaAsBi NIR emitters for integrated biosensors in wearable technology.* FizTeCh2024: 14-oji Fizinių ir technologijos mokslų centro doktorantų ir jaunųjų mokslininkų konferencija, 2024, October 15–17, Vilnius, Lithuania. (Poster)

[C34] A. Špokas, **A. Zelioli**, A. Bičiūnas, A. Čerškus, B. Čechavičius, A. Vaitkevičius, M. Kamarauskas, E. Dudutienė, R. Butkutė, *GaAsBi emitters grown using temperature limited MBE regime.* OPERA: European Workshop on Innovative and Advanced Epitaxy, 2024, June 11–14, Vilnius, Lithuania. (Oral presentation)

[C35] A. Špokas, **A. Zelioli**, A. Bičiūnas, A. Čerškus, B. Čechavičius, A. Vaitkevičius, E. Dudutienė, M. Kamarauskas, R. Butkutė, *GaAsBi based NIR emitters for blood analyte monitoring.* Open Readings 2024: 67th International Conference for Students of Physics and Natural Sciences, 2024, April 23–26, Vilnius, Lithuania. (Oral presentation)

[C36] A. Špokas, **A. Zelioli**, A. Bičiūnas, B. Čechavičius, A. Vaitkevičius, V. Bukauskas, M. Kamarauskas, E. Dudutienė, R. Butkutė, *Application focused GaAsBi based NIR emitters grown on AlAs sacrificial layer.* Apropos 19: Advanced properties and processes in optoelectronic materials and systems, 2024, October 01–04, Vilnius, Lithuania. (Oral presentation)

[C37] A. Špokas, **A. Zelioli**, A. Bičiūnas, A. Čerškus, B. Čechavičius, M. Iršėnas, A. Vaitkevičius, E. Dudutienė, M. Kamarauskas, R. Butkutė, *Enhancing luminescence of GaAsBi quantum structures for NIR emitters.* "Jaszowiec" 2024: 52nd International School & Conference on the Physics of Semiconductors, 2024, June 15–21, Szczyrk, Poland. (Oral presentation)

[C38] **A. Zelioli**, A. Špokas, D. Gailevičius, E. Dudutienė, B. Čechavičius, A. Vaitkevičius, R. Butkutė, *Fabrication of the first GaAsBi based vertical-external-cavity surface-emitting laser for NIR.* FizTeCh2024: 14-oji Fizinių ir technologijos mokslų centro doktorantų ir jaunųjų mokslininkų konferen-

cija, 2024, October 15–17, Vilnius, Lithuania. (Oral presentation)

[C39] **A. Zelioli**, A. Špokas, G. Petrusevičius, B. Čechavičius, E. Dudutienė, R. Butkutė, *Investigation of the use of AlGaAs/InGaAs quantum well for NIR emitters.* Open Readings 2024: 67th International Conference for Students of Physics and Natural Sciences, 2024, April 23–26, Vilnius, Lithuania. (Poster)

[C40] **A. Zelioli**, A. Špokas, M. Krivičius, D. Gailevičius, E. Dudutienė, B. Čechavičius, R. Butkutė, *Growth of A3-B5 heterostructures for vertical-external-cavity surface-emitting-laser designed for NIR emission.* OPERA: European Workshop on Innovative and Advanced Epitaxy, 2024, June 11–14, Vilnius, Lithuania. (Oral presentation)

[C41] **A. Zelioli**, J. Žuvelis, U. Cibulskaitė, A. Špokas, E. Dudutienė, A. Vaitkevičius, S. Stanionytė, B. Čechavičius, R. Butkutė, *Optimization of AlGaAs barriers in InGaAs quantum wells for enhanced near-infrared emission.* OPERA: European Conference on Innovative and Advanced Epitaxy, 2025, May 19–23, Pisa, Italy. (Oral presentation)

[C42] A. Špokas, **A. Zelioli**, A. Vaitkevičius, B. Čechavičius, E. Dudutienė, A. Bičiūnas, V. Bukauskas, M. Kamarauskas, R. Butkutė, *Development of application focused bismuth containing NIR electrically pumped emitters.* Open Readings 2025: 68th International Conference for Students of Physics and Natural Sciences, 2025, May 13–16, Vilnius, Lithuania. (Oral presentation)

[C43] **A. Zelioli**, A. Špokas, A. Štaupienė, E. Dudutienė, A. Suchodolskis, B. Čechavičius, M. Talaikis, G. Kontenis, D. Gailevičius, R. Butkutė, *Design and growth of GaAsBi and InGaAs based vertical-external-cavity surface-emitting-lasers.* EuroMBE 2025: 22nd European Molecular Beam Epitaxy Workshop, 2025, March 09–13, Auron, France. (Oral presentation)

[C44] A. Špokas, **A. Zelioli**, A. Vaitkevičius, A. Bičiūnas, E. Dudutienė, B. Čechavičius, M. Skapas, A. Čerškus, M. Talaikis, P.

Wojnar, V. Deibuk, R. Butkutė, *Segregation-driven formation of Bi-QDs in GaAsBi layered structures.* OPERA: European Conference on Innovative and Advanced Epitaxy, 2025, May 19–23, Pisa, Italy. (Oral presentation)

[C45] A. Špokas, **A. Zelioli**, V. Bukauskas, M. Kamarauskas, E. Dudutienė, B. Čechavičius, A. Bičiūnas, J. Spigulis, Y. Chiu, R. Butkutė, *NIR diode emitters for applications in biophotonics.* EuroMBE 2025: 22nd European Molecular Beam Epitaxy Workshop, 2025, March 09–13, Auron, France. (Poster)

[C46] **A. Zelioli**, A. Špokas, A. Štaupienė, M. Talaikis, M. Skapas, D. Gailevičius, A. Suchodolskis, A. Čerškus, S. Stanionytė, A. Vaitkevičius, B. Čechavičius, R. Butkutė, *Design of vertical-external-cavity surface-emitting lasers for near-infrared emission.* Open Readings 2025: 68th International Conference for Students of Physics and Natural Sciences, 2025, May 13–16, Vilnius, Lithuania. (Oral presentation)

[C47] E. Dudutienė, A. Štaupienė, A. Špokas, **A. Zelioli**, R. Butkutė, *Bismuth quantum dots in annealed parabolically graded GaAsBi/AlGaAs quantum well structures.* E-MRS 2025 Spring Meeting, 2025, May 26–30, Strasbourg, France. (Poster)

[C48] E. Dudutienė, A. Štaupienė, A. Špokas, **A. Zelioli**, R. Butkutė, *Effect of growth and annealing on emission from parabolic GaAsBi/AlGaAs quantum wells.* OPERA: European Conference on Innovative and Advanced Epitaxy, 2025, May 19–23, Pisa, Italy. (Oral presentation)

[C49] A. Špokas, **A. Zelioli**, A. Bičiūnas, B. Čechavičius, V. Bukauskas, E. Dudutienė, M. Kamarauskas, R. Butkutė, *Strategies for improvement of GaAsBi quantum well-based laser performance for emission above 1000 nm.* OPERA: European Conference on Innovative and Advanced Epitaxy, 2025, May 19–23, Pisa, Italy. (Oral presentation)

[C50] A. Štaupienė, **A. Zelioli**, A. Špokas, B. Čechavičius, R. Butkutė, E. Dudutienė, *The evaluation of photoluminescence efficiency of GaAsBi quantum.* Open Readings 2025: 68th

International Conference for Students of Physics and Natural Sciences, 2025, May 13–16, Vilnius, Lithuania. (Oral presentation)

[C51] A. Štaupienė, **A. Zelioli**, A. Špokas, B. Čechavičius, R. Butkutė, E. Dudutienė, *Quantitative IQE analysis of GaAsBi/GaAs MQWs.* OPERA: European Conference on Innovative and Advanced Epitaxy, 2025, May 19–23, Pisa, Italy. (Oral presentation)

[C52] A. Štaupienė, A. Špokas, **A. Zelioli**, B. Čechavičius, R. Butkutė, E. Dudutienė, *Photoluminescence investigation of the annealing effects on GaAsBi quantum wells with parabolic AlGaAs barriers.* EuroMBE 2025: 22nd European Molecular Beam Epitaxy Workshop, 2025, March 09–13, Auron, France. (Poster)

[C53] J. Glemža, S. Pralgauskaitė, J. Matukas, S. Pūkienė, **A. Zelioli**, A. Bičiūnas, B. Čechavičius, V. Nargelienė, R. Butkutė, *Low frequency noise study for developing of AlGaAs and GaAsBi QW structures for NIR LD.* 24th International Microwave and Radar Conference (MIKON), 2022, September 12–14, Gdansk, Poland. (Poster)

[C54] A. Špokas, **A. Zelioli**, B. Čechavičius, A. Vaitkevičius, E. Dudutienė, R. Butkutė, *Optimizing the temperature limited growth of GaAsBi for NIR emitters.* MOC2024: 29th Microoptics Conference, 2024, September 29–October 02, Kaohsiung, Taiwan. (Poster)

[C55] **A. Zelioli**, A. Špokas, K. Mažeika, Čechavičius B., Talaikis M., Stanionytė S., Vaitkevičius A., Čerškus A., Dudutienė E., Butkutė R., *Optimization of the gain region for large area InGaAs based NIR VECSELs.* 30th OptoElectronics and Communications Conference / International Conference on Photonics in Switching and Computing (OECC/PSC), 2025, June 29–July 03, Sapporo, Japan. (Poster)

1. LITERATURE REVIEW

1.1. Gallium Arsenide Bismide

This chapter summarizes key published results on the growth and characterization of GaAsBi and InGaAs materials, including a review of the current state-of-the-art in GaAsBi-based LDs.
Subsequently, the design strategies for VECSELs will be discussed, highlighting the most relevant results and the main limitations reported across published works.

1.1.1. Brief History

Gallium arsenide bismide (GaAsBi) is a promising III–V semiconductor alloy that has attracted significant research interest due to its potential applications in optoelectronic devices such as laser diodes, photodetectors, and solar cells. The incorporation of bismuth (Bi) into GaAs introduces unique material properties, including a substantial reduction in bandgap energy and enhanced spin–orbit splitting, making GaAsBi particularly attractive for long-wavelength infrared and telecommunication applications [1,2].
Research into GaAsBi began in the early 1990s, when efforts were made to incorporate heavy group-V elements into III–V semiconductors in order to engineer their band structures for improved optical and electronic performance [3]. Initial studies primarily focused on Metal Organic Vapor Phase Epitaxy (MOVPE) growth, and in 1998 the first successful synthesis of GaAsBi was reported [4]. Growth was performed at low substrate temperatures (around 365 °C), achieving a Bi incorporation of approximately 2 %. However, a key limitation of this method is the restricted Bi content achievable; the highest reported value using MOVPE is 3.7% [5].
To address this limitation, researchers turned to MBE techniques, which offer better control over growth parameters. Incorporating Bi is particularly challenging due to its tendency to segregate and form metallic droplets on the surface. Early MBE efforts success-

fully incorporated small amounts of Bi into GaAs, resulting in a bandgap reduction of approximately 80–90 meV per atomic percent of Bi [2].
Throughout the 2000s, advancements in epitaxial growth enabled the fabrication of GaAsBi with higher Bi content and improved crystalline quality. Optimal growth conditions, including low substrate temperatures and carefully controlled As/Ga and Bi flux ratios, were identified to enhance Bi incorporation while minimizing defects [3]. By the 2010s, experimental work confirmed theoretical predictions, showing that GaAsBi exhibits a large bowing parameter and strong bandgap reduction, reinforcing its potential for near-infrared optoelectronic applications [1].
Recent efforts have focused on refining the growth process to further increase Bi incorporation and reduce structural defects, thereby enhancing the performance and reliability of GaAsBi-based devices. As research progresses, GaAsBi continues to be a key material of interest for next-generation optoelectronic and photonic technologies.

1.1.2. Properties

In this section, we discuss three key aspects of GaAsBi properties: bandgap reduction, temperature stability, and the Band Anticrossing (BAC) effect. These phenomena not only determine the optical and electronic behavior of the alloy but also strongly influence its performance in device applications.

Bandgap Properties

One of the most distinctive features of GaAsBi is the pronounced reduction of its bandgap with increasing Bi content. Experimental studies have shown that the incorporation of Bi atoms into GaAs lowers the bandgap by approximately 60–90 meV per percent of Bi. Figure 1.1 shows experimental measurements reported by several groups [6, 7]. This strong bandgap reduction arises from two main effects:

- Perturbation of the GaAs valence band by the introduction of localized Bi states.
- Mixing of the extended GaAs states with these localized states.

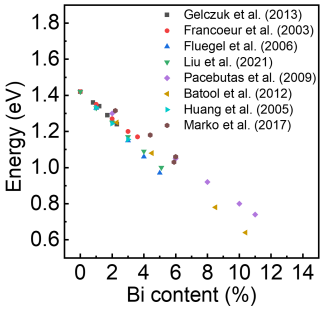

Figure 1.1: Energy bandgap of GaAsBi as a function of Bi content measured by different groups. Data points are taken from [8], [9], [6], [10], [11], [7], [12], and [13] (listed in order from top to bottom in the legend).

A widely used model to describe the GaAsBi bandgap E_{GaAsBi} is the empirical bowing equation:

$$E_{\mathrm{GaAsBi}} = (1-x)E_{\mathrm{GaAs}} + xE_{\mathrm{GaBi}} - b\,x(1-x), \tag{1.1}$$

where x is the Bi mole fraction, E_{GaAs} and E_{GaBi} are the bandgaps of GaAs and the hypothetical zinc-blende GaBi, respectively, and b is the bowing parameter [14]. Detailed Photoluminescence (PL) studies have confirmed the nonlinear dependence described in Equation 1.1, and the fitting parameters indicate a strong deviation from a simple linear interpolation between GaAs and GaBi [2].
Further refinements introduce a composition-dependent bowing parameter:

$$b(x) = \frac{\alpha}{1+\beta x}, \tag{1.2}$$

which, when substituted back into Equation 1.1, provides a more accurate description of experimental data. Here, α and β are fitting parameters that describe the variation of the bowing parameter with Bi content in GaAsBi [14]. This refined model emphasizes the critical role of Bi-induced perturbations in shaping the electronic structure of the alloy.

Temperature Stability

A major advantage of GaAsBi over conventional GaAs is its enhanced temperature stability. In many semiconductor lasers and photodetectors, temperature-induced variations in the bandgap can

degrade device performance. GaAsBi alloys, however, exhibit a significantly lower temperature coefficient of the bandgap. Measurements indicate a shift of approximately 0.1 meV K^{-1}, compared to around 0.35 meV K^{-1} for GaAs. Figure 1.2 shows the bandgap of GaAsBi measured as a function of temperature, alongside the bandgap of GaAs bulk for comparison [15]. This improved temper-

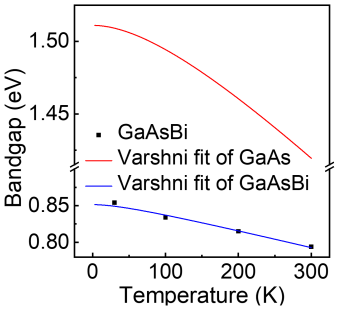

Figure 1.2: Temperature dependence of the bandgap for GaAsBi, measured by our group using photoreflectance (blue), and calculated bandgap for GaAs using parameters from [16] (red).

ature stability is primarily attributed to the localized states introduced by Bi incorporation. These states tend to pin the valence band maximum, making the bandgap less sensitive to thermal effects such as lattice expansion and electron–phonon interactions. Additionally, Bi reduces the overall strength of electron–phonon coupling, further stabilizing the optical properties of the material [17].
From a device perspective, this temperature insensitivity is particularly valuable for the development of uncooled lasers and photodetectors, especially in optical communication systems, where wavelength stability is critical [18].

Band Anticrossing Effect

The BAC model has been widely used to explain the unusual band structure behavior observed in GaAsBi. According to this model, the localized states introduced by Bi interact strongly with the extended valence band states of the GaAs host matrix, resulting in a significant restructuring of the valence band. This interaction is

described by the following expression:

$$E_{-}(k) = \frac{1}{2}\left(E_{VB} + E_{Bi} - \sqrt{(E_{VB} - E_{Bi})^2 + 4C^2}\right), \qquad (1.3)$$

where E_{VB} is the energy of the GaAs valence band edge, E_{Bi} is the energy level of the localized Bi states, and C is the coupling parameter that quantifies the interaction strength [19]. Equation 1.3 captures how the Bi states effectively repel the GaAs valence band states, resulting in a lowering of the bandgap.

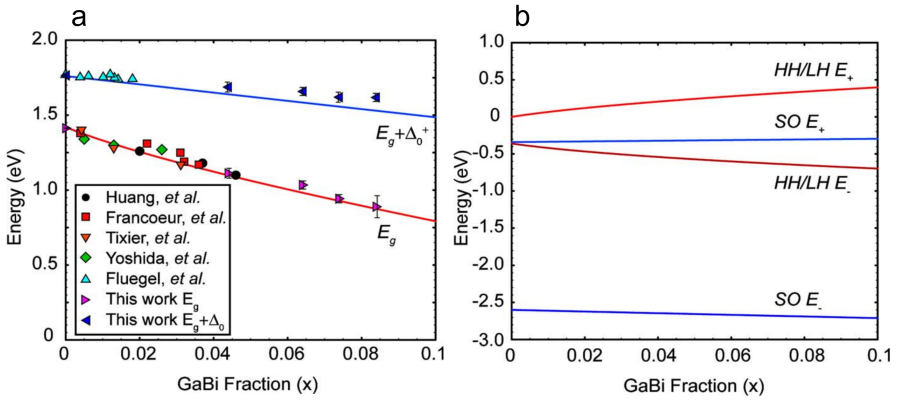

Figure 1.3: (a) $GaAs_{1-x}Bi_x$ bandgap values along with experimental data from [2, 9, 12]; (b) calculated positions of the E_+ and E_- bands (associated with heavy, light, and spin-orbit split-off bands) as determined by the VBAC model as a function of Bi content. Figure adapted from [19].

Impact on Spin-Orbit Splitting

Another important consequence of the BAC interaction is the enhancement of the Spin-Orbit Splitting Energy (Δ_{SO}). As the Bi content increases, Δ_{SO} can eventually exceed the bandgap energy itself. This inversion has significant implications for carrier recombination dynamics: specifically, it can suppress nonradiative Auger recombination processes that are typically detrimental to laser performance [6]. This suppression is one of the main reasons why GaAsBi is considered a strong candidate for high-efficiency, high-temperature light-emitting applications [20].
Both theoretical predictions and experimental data support the

BAC model in GaAsBi. Density Functional Theory (DFT) calculations reveal that the strong perturbation induced by Bi leads to a substantial anticrossing interaction in the valence band [21]. Experimentally, the evolution of the band structure with increasing Bi content has been studied through techniques such as PL spectroscopy and photoreflectance. The results, shown in Figure 1.3, closely match the predictions of the BAC model [2, 22].

1.1.3. Growth Techniques

The growth of GaAsBi by MBE is particularly challenging due to the low miscibility of Bi in GaAs and the strong tendency of Bi atoms to segregate at the growth surface. Successful synthesis requires precise control of growth kinetics, surface reconstructions, and substrate temperature.
Optimization of GaAsBi growth depends on careful adjustment of several parameters:

- As/Ga flux ratio: Near-stoichiometric or slightly As-rich conditions are required. Excessive As flux suppresses Bi incorporation, while Ga-rich conditions promote Ga–Bi droplet formation [23].
- Bi flux: An increased Bi flux initially enhances Bi incorporation, but beyond a critical threshold, Bi saturates at the surface and segregates into droplets [14].
- Growth rate: Slower growth rates promote Bi incorporation by increasing surface residence time, but also raise the risk of surface segregation and defect formation.
- Substrate temperature: Efficient Bi incorporation requires relatively low growth temperatures (typically 280–350 °C) [14].

Efficient Bi incorporation without droplet formation requires near-stoichiometric conditions, as demonstrated in early studies [24]. Figure 1.4 illustrates the impact of the As/Ga flux ratio on Bi incorporation and surface roughness. *in situ* Reflection High-Energy Electron Diffraction (RHEED) is commonly employed to monitor surface conditions. A transition from a streaky (2×1) to a spotty

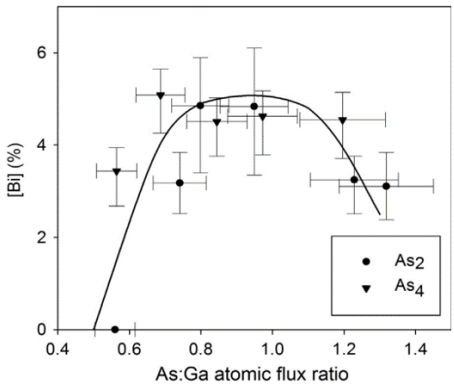

Figure 1.4: Bismuth incorporation for various As:Ga atomic flux ratios using As_2 (solid circles) and As_4 (solid triangles). To account for the approximate 50 % desorption of As_4 during growth, the As_4:Ga ratios have been halved [25, 26]. A spline curve, fitted to both data sets, is included as a guide to the eye. Figure adapted from [27].

(2×1) pattern indicates the onset of Ga-rich conditions and an increased risk of droplet formation. Surface reconstructions also affect the number of available bonding sites, thereby influencing Bi incorporation probability. The dependence of surface reconstruction patterns on As/Ga flux ratio and substrate temperature is shown in Figure 1.5(b). Lower substrate temperatures enhance Bi incorporation by suppressing desorption, but reduced adatom mobility at these temperatures can lead to higher defect densities and Bi compositional inhomogeneity. Therefore, the optimal growth temperature represents a balance between efficient Bi incorporation and sufficient surface diffusion to maintain crystalline quality [23].
A distinctive feature of GaAsBi MBE growth is the dual role of Bi on the surface. Under As-rich conditions, Bi acts as a quasi-wetting layer, behaving like a surfactant that improves surface smoothness. Once a critical coverage is reached Bi atoms may act as an anti-surfactant, leading to the formation of Ga-Bi droplets [29, 30].
The formation of droplets is a key challenge in GaAsBi growth. As the Bi coverage increases, the large atomic size mismatch between Bi and As induces strain that cannot be fully accommodated by the lattice. This leads to the nucleation of droplets, particularly under Ga-rich conditions where excess Ga further facilitates droplet formation [30]. Several studies have demonstrated that careful control

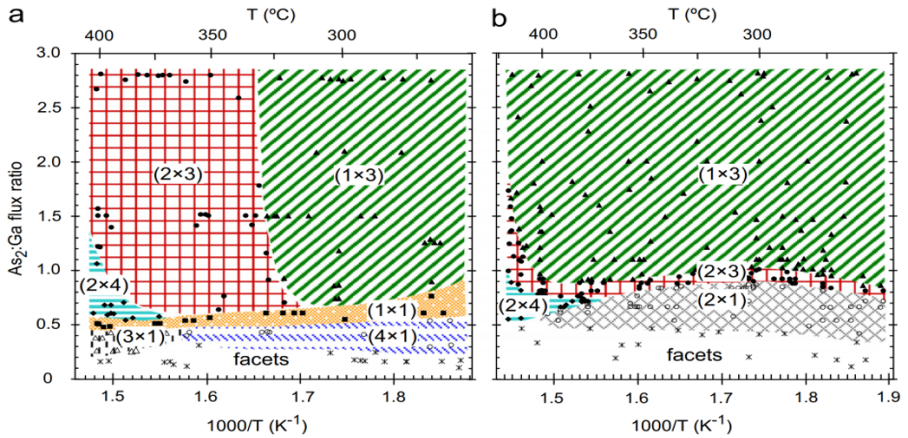

Figure 1.5: Surface reconstruction maps for (a) GaAs (001) and (b) $GaAs_{1-x}Bi_x$ (001) for substrate temperatures from 250 °C to 425 °C and As_2:Ga flux ratios from 0 to 3 (As_2:Ga Beam Equivalent Pressure (BEP) ratio from 0 to 9.4). The $GaAs_{1-x}Bi_x$ surface was grown with an incident Bi BEP of 3×10^{-9} Torr. Figure adapted from [28].

of the As/Ga flux ratio, along with moderated Bi flux, is crucial to suppressing droplet formation.
Post-growth treatments such as annealing can partially alleviate droplet issues, improving surface smoothness and crystalline quality [31]. Thus, successful MBE growth of GaAsBi is achieved through a careful and dynamic balance of growth kinetics, surface reconstruction, flux ratios, and temperature control, essential for producing high-quality layers suitable for advanced optoelectronic applications.

1.2. Laser Diodes

Recent progress in electrically pumped GaAsBi QW laser diodes has advanced their potential for practical NIR applications. Both Continuous Wave (CW) and pulsed lasing from GaAsBi active regions have been demonstrated, with emission wavelengths ranging from approximately 950 nm to beyond 1.1 µm [18, 32–34]. These results highlight the promise of GaAsBi for telecom-relevant wavelengths on cost-effective GaAs substrates, making them attractive for uncooled laser applications.

Early GaAsBi laser diode designs employed simple single QWs embedded within AlGaAs barriers, grown either by MBE or MOVPE. Initial demonstrations reported pulsed room-temperature lasing with around 2 % Bi incorporation. More recent structures have achieved higher Bi contents (5–6 %), enabling emission wavelengths up to approximately 1.14 µm under electrical injection [18, 33]. These improvements were made possible by critical growth optimizations, including precise control of substrate temperature, V/III flux ratio, and arsenic overpressure, which are essential to preserve crystalline quality and minimize defect densities.

Performance metrics of GaAsBi laser diodes are encouraging. Internal quantum efficiencies are comparable to those of conventional GaAs-based devices, while optical gain measurements reveal moderate internal optical losses (typically 10–15 cm^{-1}), consistent with good waveguide quality [32]. Increasing the Bi fraction systematically redshifts the emission wavelength but can also introduce localized and extended tail states that influence carrier dynamics. Design strategies such as the inclusion of electron-blocking layers have proven effective in reducing carrier leakage and maintaining low threshold currents.

A distinct advantage of GaAsBi-based lasers is their reduced temperature sensitivity. The smaller bandgap temperature coefficient results in lower wavelength shifts ($d\lambda/dT$) compared to standard GaAs lasers. For instance, $GaAs_{0.97}Bi_{0.03}$ lasers exhibited a coefficient of approximately 0.16 $nm\,K^{-1}$, about half the value observed in conventional GaAs diodes [18]. Furthermore, the condition where the Δ_{SO} exceeds the bandgap in GaAsBi suppresses Auger recombination, thereby enhancing thermal stability and efficiency [32, 33].

Despite these advances, challenges remain. Incorporating Bi contents above 6 % exacerbates miscibility problems and defect formation, demanding rigorous flux control and often requiring post-growth treatments. Nevertheless, continued progress in epitaxial growth and device design is steadily pushing GaAsBi laser performance towards the technologically important telecom windows at 1.3–1.55 µm. With ongoing improvements in material quality and device engineering, GaAsBi lasers are strong candidates for future cost-effective data and telecommunication systems operating with relaxed cooling requirements.

1.3. Vertical-External-Cavity Surface-Emitting Laser

VECSELs have emerged as a highly versatile class of semiconductor lasers, combining the advantages of semiconductor gain media with those of external solid-state resonator architectures. This section provides an overview of their key properties, benefits, limitations, and structural considerations.

1.3.1. Main Advantages

VECSELs offer several notable advantages that make them attractive for a wide range of applications:

- Wavelength versatility: The semiconductor gain medium can be engineered to cover a broad spectral range, extending from the visible to the mid-infrared [35].
- High beam quality: Owing to their large, optically pumped gain area, VECSELs can operate with nearly diffraction-limited beam quality ($M^2 \approx 1$), outperforming edge-emitting lasers [35].
- Power scalability: Continuous-wave power levels exceeding 100 W have been demonstrated, supported by efficient heat dissipation using external heat spreaders or flip-chip bonding [36].
- Ultrafast pulse generation: Sub-picosecond pulses at GHz repetition rates can be produced, enabling applications such as frequency combs and ultrafast spectroscopy [37].
- Intracavity nonlinear optics: The open cavity design facilitates efficient intracavity frequency conversion, enabling compact sources across the visible and ultraviolet spectral regions [38].

1.3.2. Main Disadvantages

Despite their many strengths, VECSELs also face several challenges:

- Thermal management: Heat extraction is a major limitation due to the thin gain region, necessitating advanced cooling approaches such as intracavity heat spreaders or flip-chip bonding [39].
- Fabrication complexity: High-quality gain structures, typically incorporating MQWs or Quantum Dots (QDs), require precise control over strain, composition, and thickness during growth [40].
- Electrical pumping limitations: While optically pumped devices are mature, electrically pumped VECSELs remain challenging because of the difficulty of achieving uniform carrier injection across a wide active area [41].
- Optical losses and cavity stability: The external cavity configuration introduces alignment sensitivities and potential parasitic losses, which can reduce efficiency and compromise wavelength stability [42].

1.3.3. Description of the Structure

A typical optically pumped VECSEL consists of a semiconductor gain mirror and an external cavity mirror. The gain mirror incorporates MQWs embedded in a semiconductor matrix and positioned within an optical microcavity. A schematic of a VECSEL chip is shown in Figure 1.6, where the layered structure is illustrated on top and the conduction band profile with the lasing standing wave is shown below. The main components of the structure are:

- DBR: a high-reflectivity bottom mirror that provides optical feedback.
- Active region: a gain section containing MQWs or QDs placed at the antinodes of the standing optical wave to maximize light–matter interaction.
- Window layer: a transparent layer that suppresses surface recombination and ensures carrier confinement [35].

The external cavity is formed between the gain mirror and an output coupler, enabling wavelength tuning via intracavity filters or a semiconductor saturable absorber mirror [43]. Achieving high performance requires careful optimization of these structural elements.

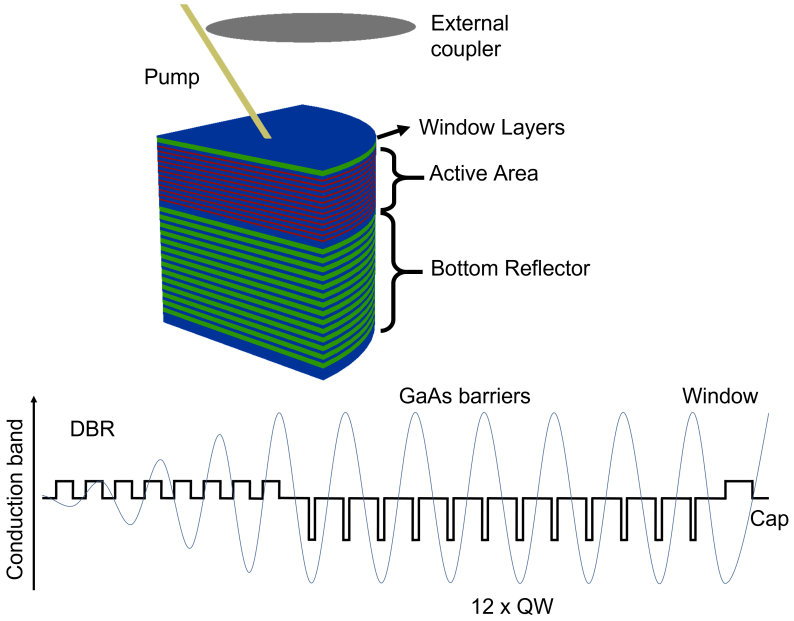

Figure 1.6: Schematic of a VECSEL structure. Top: layered structure in a lasing configuration with the main components highlighted. Bottom: conduction band profile of the chip with the lasing standing wave. For clarity, the drawing is not to scale.

1.3.4. Distributed Bragg Reflector

The DBR is a crucial part of the VECSEL structure, consisting of alternating layers with different refractive indices that form a high-reflectivity mirror. Materials used for the DBR should combine a large refractive index contrast, which minimizes the total thickness, with lattice matching to avoid defect generation. GaAs/AlAs DBRs provide high reflectivity together with good thermal conductivity, while AlGaAs-based DBRs are often used for shorter wavelengths [40].
The DBR operates as a quarter-wavelength mirror, with each layer thickness defined as:

$$d = \frac{\lambda}{4n}, \tag{1.4}$$

where λ is the target wavelength and n is the refractive index of the material. Refractive indices for GaAs and AlAs are typically obtained from empirical models.

1.3.5. Gain Region and Window

The gain region is composed of MQWs designed for efficient carrier confinement and optical amplification. The barriers separating the wells are adjusted so that the QWs coincide with the antinodes of the standing optical field. Their thickness is given by:

$$d_{\text{barrier}} = \frac{\lambda}{2n_{\text{barrier}}} - d_{\text{QW}}, \tag{1.5}$$

where n_{barrier} is the refractive index of the barrier material and d_{QW} is the quantum well thickness. The final barrier thickness is fine-tuned to align the optical field distribution with the active region.
The window layer acts as both an optical confinement and a protective layer. Its thickness follows:

$$d_{\text{window}} = \frac{\lambda}{2n_{\text{window}}}, \tag{1.6}$$

where n_{window} is the refractive index of the window material. A thin capping layer is typically added to prevent oxidation of the AlAs window, ensuring long-term stability.
The total chip thickness can be expressed as:

$$d_{\text{chip}} = d_{\text{DBR}} + d_{\text{gain}} + d_{\text{window}} + d_{\text{cap}}, \tag{1.7}$$

where each contribution is tailored to the target wavelength. Through precise engineering of these layers, VECSELs achieve high output power, wavelength tunability, and efficient thermal management.

1.3.6. InGaAs for VECSEL

Indium gallium arsenide (InGaAs) is a ternary III–V semiconductor alloy composed of indium arsenide (InAs) and gallium arsenide (GaAs). It is widely recognized for its favorable optoelectronic properties. InGaAs exhibits a direct band gap tunable from 1.424 eV to 0.35 eV at room temperature, depending on the indium content, covering the NIR spectral range. This makes it a key material for high-performance photodetectors used in Short-Wave Infrared (SWIR) imaging and telecommunications.

InGaAs/GaAs MQWs in particular are widely employed in photodetectors, photovoltaic devices, Light Emitting Diodes (LEDs), and NIR lasers due to their efficiency and spectral versatility [44–47]. For MBE-grown emitters, the main challenges are indium segregation and lattice mismatch dislocations, both of which can degrade device performance.

Indium segregation refers to the non-uniform distribution of indium atoms within the alloy during growth, resulting in compositional inhomogeneity. This process is strongly influenced by the lower surface diffusivity of indium compared to gallium and arsenic, which promotes clustering of indium atoms. In InGaAs QWs, segregation effects are enhanced at higher growth temperatures, leading to increased inhomogeneity [48, 49].

Strain also plays a critical role: the larger atomic size of indium compared to gallium introduces lattice mismatch, which promotes segregation and can induce piezoelectric effects in indium-rich regions [50, 51]. At elevated growth temperatures, the sticking coefficient of indium decreases, increasing desorption and further contributing to compositional non-uniformity [52–54].

The consequences of indium segregation include band gap fluctuations and strain relaxation. Indium-rich regions reduce the band gap locally, introducing spectral inhomogeneity and redshifts in absorption [52, 55, 56]. Strain relaxation may further generate interfacial defects such as dislocations, acting as non-radiative recombination centers that lower PL intensity and device efficiency.

Several techniques have been explored to suppress indium segregation. Lowering the growth temperature and increasing arsenic overpressure reduce segregation by kinetically limiting indium migration, though this often weakens PL intensity and crystalline quality [52]. Reduced growth rates (around 400 $\mathrm{nm\,h^{-1}}$) improve interface sharpness and optical properties [57, 58]. In some cases, pre-adsorption of indium on the GaAs surface has been used to stabilize the composition during steady-state growth [54, 59].

A second major limitation is the lattice mismatch between InGaAs and GaAs, which can generate misfit dislocations when the critical thickness is exceeded for a given indium content [60]. These dislocations act as non-radiative centers, lowering PL intensity, decreasing efficiency, and introducing localized heating in devices [61–65].

To mitigate these effects, strain compensation is often used. For InGaAs/GaAs QWs, GaAsP layers can be incorporated to counterbalance the compressive strain. However, this approach introduces another lattice-mismatched compound, adding complexity and possible interfacial defects [63, 66]. Alternatively, diluted nitrides can be employed: incorporating a small nitrogen fraction (typically <2 %) reduces the required indium concentration for a given band gap, thereby lowering lattice mismatch. Nevertheless, nitrogen incorporation often introduces point defects, which remain a significant drawback [67–70].

2. METHODS

2.1. Molecular Beam Epitaxy Equipment

MBE is an advanced epitaxial growth technique that enables the fabrication of semiconductor structures and devices with atomic-level precision. The process operates under Ultra-High Vacuum (UHV) conditions (approximately 1×10^{-10} Torr), which minimizes contamination and allows precise control over material composition and epitaxial layer thickness.
The system used in this work is a solid-source MBE Veeco GENxplor R&D model, equipped with effusion cells for gallium, aluminum, indium, bismuth, silicon, and beryllium, as well as a specially designed arsenic source producing a pure As_2 flux. The system comprises three interconnected UHV chambers designed for substrate preparation, epitaxial growth, and *in situ* characteriza-

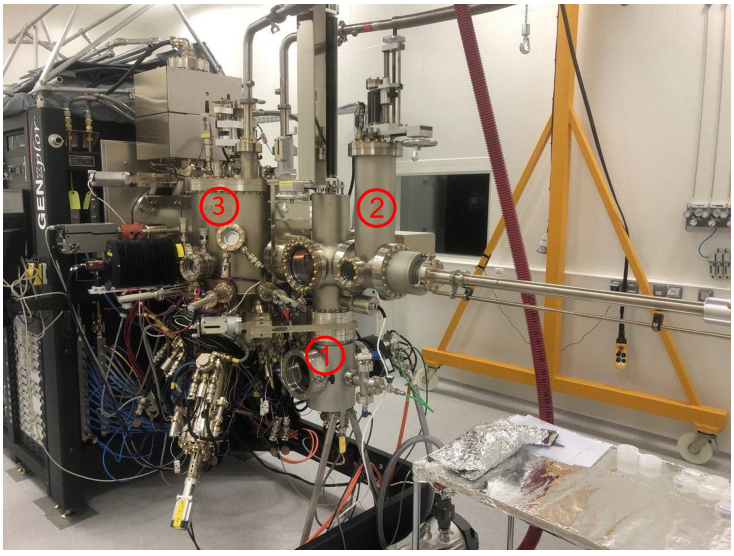

Figure 2.1: Picture of the MBE Veeco GENxplor R&D system used. The numbers indicate the different chambers of the machine: (1) loadlock, (2) buffer chamber, (3) growth chamber.

tion. Figure 2.1 shows: (1) the loadlock, used for substrate insertion without breaking vacuum in the growth chamber; (2) the buffer chamber, where sample storage and additional preparation take place; and (3) the growth chamber, where epitaxial deposition and *in situ* monitoring are performed.

2.1.1. *in situ* Characterization

Reflection High-Energy Electron Diffraction

RHEED is a key *in situ* technique for monitoring surface morphology, crystalline quality, and growth dynamics in real time. A high-energy electron beam (10–30 keV) is directed at the substrate at a shallow angle (1–3 °), as shown in Figure 2.2. Because of this grazing incidence, the electrons interact mainly with the surface atomic layers, producing a diffraction pattern highly sensitive to surface conditions. Streaky patterns typically indicate smooth two-dimensional layer growth, while spotty patterns reveal rough, three-dimensional island growth. Rapid interpretation of these patterns enables immediate adjustment of growth conditions, such as substrate temperature or flux ratios, which is essential for maintaining epitaxial film quality.

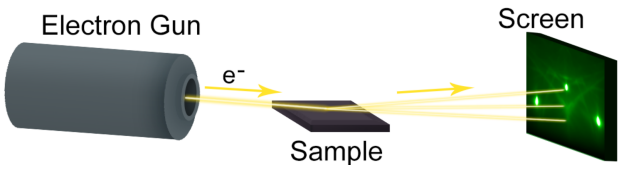

Figure 2.2: Sketch of a RHEED system, taken from [71].

Beam Flux Monitor

The Beam Flux Monitor (BFM) used in this work is a Bayard–Alpert ionization gauge. It measures the flux of atomic or molecular beams from the effusion cells by ionizing the beam species, collecting the ions, and measuring the resulting ion current. Since the current is proportional to the beam flux, the BFM provides accurate, real-time monitoring of deposition rates. This feedback is crucial for controlling layer thickness and composition, directly impacting the quality of grown quantum structures.

Band-Edge Thermometry

Band-edge Thermometry (BandiT) is an optical *in situ* technique used to measure substrate temperature and monitor composition during growth. It operates by detecting the spectral position of the fundamental absorption edge (band edge), which shifts with both temperature and material composition. Because it is contact-free, it provides precise substrate temperature control and real-time composition feedback, ensuring reproducibility and accuracy of epitaxial layers.

2.1.2. Sample Preparation

Proper substrate preparation is critical for achieving atomically clean surfaces and high-quality epitaxy. Substrates are first loaded into the loadlock (Figure 2.1(1)), where they undergo annealing at 200 °C for 2 hours. The temperature is slowly ramped to preserve vacuum conditions. Afterward, the substrates are transferred to the buffer chamber (Figure 2.1(2)) for a second annealing step at 300 °C for 1 hour. The final annealing is carried out in the growth chamber (Figure 2.1(3)), where native GaAs oxide is removed by heating the substrate above 580 °C under As flux. Complete deoxidation and the appearance of the characteristic 2×4 GaAs surface reconstruction typically occur at 650–700 °C. Following this step, the substrate temperature is lowered to 580–630 °C, and a GaAs buffer layer with a thickness of 150–500 nm is deposited to improve surface quality.

2.2. `Nextnano`^{3} Calculations

To model the electronic band structure of QW heterostructures, simulations were carried out using the `Nextnano`^{3} package. This software performs full-band quantum mechanical simulations within the $\mathbf{k} \cdot \mathbf{p}$ formalism and effective mass approximation. In this work, one-dimensional simulations along the growth axis (z-direction) were conducted using an 8×8 $\mathbf{k} \cdot \mathbf{p}$ Hamiltonian, including the conduction band minimum at the Γ point and both Heavy Hole (HH) and Light Hole (LH) valence bands. Excitonic effects and the temperature dependence of the band gap were incorporated, as well as strain effects. The simulations provided energy

levels, wavefunctions, and potential profiles, offering insights into carrier confinement and optical transition energies crucial for VECSEL optimization. Simulation parameters for GaAs, AlGaAs, and InGaAs were taken from the `Nextnano`[3] database, while GaAsBi parameters were extracted from the literature: band gap and Δ_{SO} from [72], elastic constants from [73], lattice constant from [74], and band offsets from [75].

2.3. Photoluminescence Spectroscopy System

PL spectroscopy is a non-destructive tool used to assess the optical quality of QW structures, revealing defects, inhomogeneities, and localized states. Three different configurations were used: RTPL, Micro-Photoluminescence (µPL), and Temperature-Dependent Photoluminescence (TDPL).

2.3.1. Room Temperature PL

RTPL mapping was performed using a diode-pumped solid-state laser (532 nm, $\sim$5 kW cm^{-2}) (1) focused to a $\sim$50 µm spot. Emission was collected with a 420 mm focal-length monochromator and detected using a thermoelectrically cooled InGaAs photodetector (5). Samples were mounted on motorized XY stages with 0.31 µm resolution (3), enabling large-area mapping of intensity and peak position. This method revealed sample uniformity, defect distributions, and strain relaxation. A photograph of the setup is shown in Figure 2.3.

2.3.2. µPL Setup

µPL was performed with a WITec Alpha 300S confocal microscope (Figure 2.4 (2)). Excitation was provided by a 665 nm CW laser diode (1), focused with a 100$\times$ objective (NA = 0.9) to a $\sim$1 µm spot. Emission was collected through the same objective and analyzed with an Andor Shamrock spectrometer (3) coupled to a cooled InGaAs camera (4). This configuration enabled high-resolution mapping of localized emission, sensitive to threading dislocations and non-radiative centers not resolvable with RTPL.

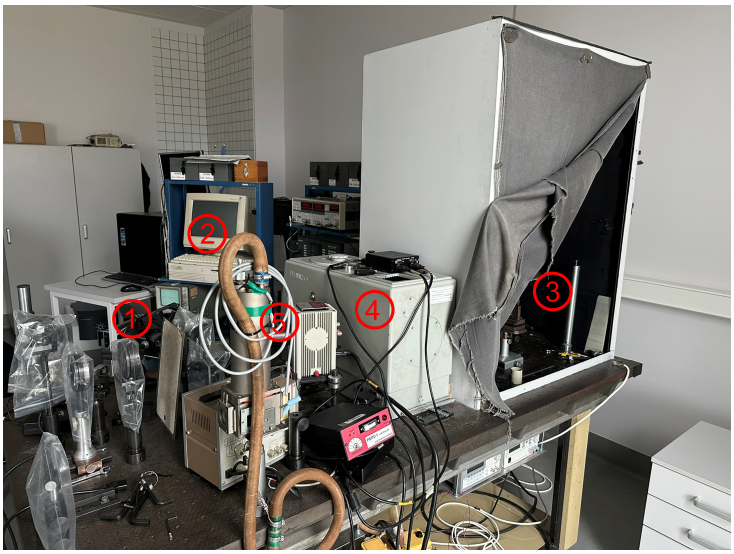

Figure 2.3: Picture of the RTPL setup used in this work. (1) diode-pumped solid-state laser (532 nm, ∼5 kW cm^{-2}), (2) CMAC used for data collection, (3) dark room where the samples were mounted on motorized XY stage, (4) monochromator, (5) detector used.

2.3.3. Temperature-Dependent PL

TDPL measurements were performed using the optical setup shown in Figure 2.5. The sample was mounted in a closed-cycle helium cryostat equipped with a temperature controller (4), allowing measurements over the range of 3.5–300 K. A diode-pumped solid-state (DPSS) laser emitting at 532 nm (1), with a maximum average power of 400 mW and a spot diameter of approximately 0.6 mm, was used as the excitation source. The laser was modulated at 193 Hz (2). To minimize sample heating, the excitation intensity was attenuated using a neutral-density gradient filter (3). PL signal was collected by a multi-lens system (5 and 6), passed through a long-pass filter (HWB760) (7), and dispersed by a monochromator (500 mm, 600 lines/ mm grating optimized for 1000 nm) (8). Detection was carried out with an InGaAs photodetector (9), either liquid-nitrogen cooled or thermoelectrically cooled, in combination with lock-in amplification.

Figure 2.4: Picture of the µPL setup used. (1) laser diode used for excitation, (2) confocal microscope, (3) spectrometer, (4) camera.

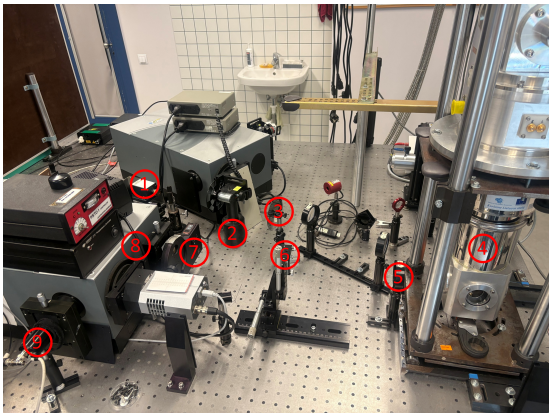

Figure 2.5: Picture of the TDPL setup used in this work. (1) Diode-pumped solid-state (DPSS) laser 532 nm, (2) chopper or modulator (for lock-in), (3) neutral-density gradient filter, (4) closed-cycle He cryostat coupled with temperature controler, (5) colimating lens (f = 100 mm), (6) focusing lens (f = 325 mm), (7) longpass filter, (8) monochromator (f = 500 mm), (9) InGaAs photodetector.

2.4. Reflectance Measurements

Reflectance spectra were measured with a spectroscopic ellipsometry system at normal incidence, consisting of a halogen lamp, monochromator, and photodetector with lock-in detection. Samples were mounted on a precision stage for stable positioning. Measurements were baseline-corrected using a silver mirror reference. This method was used to characterize key optical features such as the stop band of DBRs and cavity resonances in VECSEL structures, enabling verification of layer thicknesses and spectral alignment between the quantum well emission and cavity resonance.

2.5. Optical Setup for Lasing Measurements

The optical setup for VECSEL lasing characterization was developed at the Laser Research Center, Vilnius University. Samples were cleaved into 3×3 mm chips and mounted in a V-shaped external cavity configuration. The chips were attached to copper blocks with thermally conductive paste and cooled using a Peltier module, maintaining 16–22 °C during operation. Optical pumping was provided by an 808 nm diode laser, focused to a $\sim$300 µm spot normal to the surface. An external mirror (99 % reflectivity at 1064 nm, covering 1020–1080 nm) served as the output coupler. Emission was separated from residual pump light using a dichroic splitter and recorded with an Avantes AvaSpec-3648 spectrometer, covering 200–1100 nm.

3. RESULTS AND DISCUSSION

The following summarizes the main results obtained during the PhD research. These include:

- Annealing effects on InGaAs QWs.
- Lattice mismatch formation in InGaAs MQWs. Results from this study have been submitted for publication [A7].
- Use of AlGaAs as an electron-blocking layer for InGaAs QWs. Findings were published in [A4].
- Stress accumulation in GaAsBi MQWs, with partial results published in [A1].
- Optimization of growth parameters for GaAsBi MQWs.
- Effect of annealing on the emission properties of GaAsBi MQWs.
- Evaluation of the IQE of GaAsBi, published in [A3].
- LDs growth, processing, and characterization, published in [A6].
- LDs low-frequency noise characterization, published in [A2] and [A5].
- VECSEL design and growth.
- VECSEL characterization, reported and accepted for the ESA project Infrared (IR) Bi-based sources (Irbis), Contract No. 4000122271/NL/SC.

The samples grown and analyzed throughout this work vary significantly in terms of structure type, material system, and growth parameters. For this reason, different naming conventions were adopted in each section to reflect the specific differences emphasized for comparison.

3.1. InGaAs Optimization

The main advantage of using InGaAs for NIR emitters in this work is that it is a well-established material system with extensive literature, allowing for a reliable comparison of different designs.
To enable meaningful comparison with devices reported in the literature, it was first necessary to optimize InGaAs growth in our system. The main limitations of InGaAs, already discussed in subsection 1.3.6, are addressed here with particular focus on: indium segregation, lattice mismatch dislocations and carrier thermalization in InGaAs/GaAs QWs.

3.1.1. Substrate Temperature Effect

It has been demonstrated that in (Ga,In)(N,As) alloys, indium segregation increases with substrate temperature [52, 58]. In arsenide-based systems, the primary strategy to minimize segregation and achieve uniform In content is kinetic limitation.
Kinetic limitation can be achieved in two ways: (i) lowering the growth temperature or (ii) increasing the arsenic flux during growth. Since surface segregation involves exchange between surface and bulk atoms, reducing the substrate temperature suppresses the kinetics of this process. Similarly, a higher As flux promotes faster In incorporation by reducing the surface lifetime of indium atoms, thereby suppressing segregation.
However, both strategies also reduce crystalline quality, which can degrade device performance. In Ref. [52], it was shown that segregation can be almost completely suppressed at growth temperatures near 370 °C, but with a strong deterioration of crystal quality. The best results, as judged by PL intensity, were obtained at 510 °C. At higher temperatures (around 570 °C), significant indium desorption occurs, lowering the In content in the layer.
This poses a major challenge for device fabrication, since VECSEL structures also contain GaAs and AlAs layers, which require higher growth temperatures for optimal crystalline quality. In particular, the best results for AlAs are achieved at 600–720 °C [76–80].
To address this, the effect of barrier growth temperature and annealing temperature on InGaAs/GaAs and InGaAs/AlGaAs QWs was systematically studied. Four samples were grown: RQW+LT_GaAs, RQW+HT_GaAs, RQW+LT_AlGaAs, and

RQW+HT_AlGaAs. Each structure contained a single rectangular InGaAs QW with nominal indium content of 22.5 %. The barriers were either GaAs (RQW+LT_GaAs, RQW+HT_GaAs) or AlGaAs with 31 % Al and a GaAs cap (RQW+LT_AlGaAs, RQW+HT_AlGaAs). In the LT samples, barriers and caps were grown at 510 °C, while in the HT samples they were grown at 570 °C. A schematic of the four structures is shown in Figure 3.1. The PL spectra of the four samples are presented in Figure

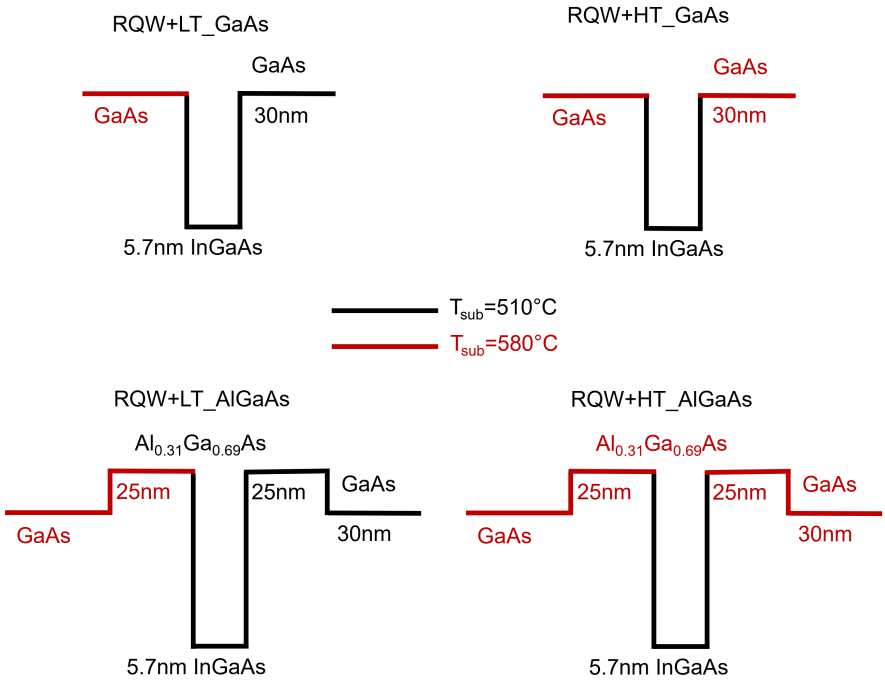

Figure 3.1: Schematic of the four samples grown to study the effect of substrate temperature on InGaAs QWs. Layers shown in red were grown at 570 °C, while those in black were grown at 510 °C.

3.2. In both GaAs and AlGaAs barrier cases, increasing the barrier growth temperature led to a blue shift in the emission energy and a reduction in intensity. This behavior is attributed to decreased crystalline quality and reduced indium incorporation caused by indium desorption.
From this series we conclude that, for device fabrication, it is more critical to optimize the growth of InGaAs itself rather than increasing the growth temperature of the successive barrier layers.

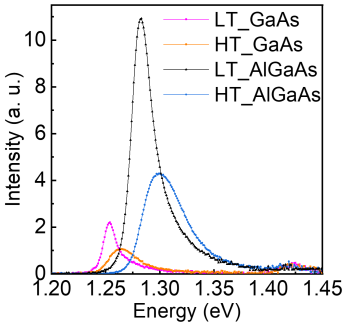

Figure 3.2: RTPL spectra of the four samples grown to study the effect of substrate temperature on InGaAs QWs. Samples with low-temperature caps (blue and black) correspond to RQW+LT_GaAs and RQW+LT_AlGaAs, while those with high-temperature caps (magenta and orange) correspond to RQW+HT_GaAs and RQW+HT_AlGaAs.

3.1.2. Dislocation Density Minimization

Minimizing dislocation density in InGaAs/GaAs MQWs is critical for achieving uniform emission and high optical efficiency in VECSEL structures. Dislocations act as non-radiative recombination centers, degrading the PL signal and contributing to localized heating. This section presents a detailed strain analysis and correlates it with dislocation formation across six MQW samples using theoretical modeling and photoluminescence measurements.
The samples are named according to their design type and indium content in the QWs. Structures labeled A feature barriers of uniform thickness, B refers to structures with alternating thin and thick barriers, while C corresponds to a triplet-well design.

Stress Calculation

The formation of MDs was analyzed using the Matthews–Blakeslee equilibrium model, which provides an estimate of the critical thickness T_{eq} above which strain relaxation occurs through MD formation. The critical thickness is given by

$$T_{\text{eq}} = \frac{1}{f} \cdot \frac{b(1-\nu/4)}{2\pi(1+\nu)} \ln\left(\frac{4T_{\text{eq}}}{b}\right), \tag{3.1}$$

where f is the lattice mismatch strain between the InGaAs and

GaAs layers, $\nu = 0.311$ is the Poisson ratio for GaAs, and b is the Burgers vector. In zinc blende III–V semiconductors such as GaAs and InGaAs, dislocations typically propagate along [110] directions within (111) slip planes. For the case of 60 ° dislocations, which dominate strain relaxation in these systems, the Burgers vector is defined as

$$b = \frac{a_0}{\sqrt{2}} = \frac{5.6531 \text{ Å}}{\sqrt{2}} \approx 3.996 \text{ Å}, \tag{3.2}$$

where $a_0 = 5.6531$ Å is the lattice constant of GaAs [60].
The lattice mismatch strain f was calculated using Vegard's law for the $In_xGa_{1-x}As$ alloy:

$$f = \frac{a_x - a_0}{a_0}, \quad a_x = 6.0583 - 0.405(1 - x). \tag{3.3}$$

In MQW structures, the total strain is distributed between the wells and barriers. The average strain is expressed as

$$\langle f \rangle = f \cdot \frac{N t_w}{N t_w + (N-1) t_b}, \tag{3.4}$$

where N is the number of quantum wells, t_w is the well thickness, and t_b is the average barrier thickness. The corresponding equilibrium strain is derived from the critical thickness T_{eq} obtained in Equation 3.1 and the total thickness of the MQW region T_{MQW}:

$$\langle f_{\text{eq}} \rangle = f \cdot \frac{T_{\text{eq}}}{T_{\text{MQW}}}. \tag{3.5}$$

The excess strain responsible for dislocation formation is then given by

$$\langle f_{\text{ex}} \rangle = \langle f \rangle - \langle f_{\text{eq}} \rangle. \tag{3.6}$$

The quantum well and barrier thicknesses, along with indium contents, were determined by X-ray Diffraction (XRD). For instance, sample Bx0240 incorporates 12 QWs arranged in 6 pairs, with alternating barrier thicknesses of 7.3 nm and 119 nm, giving an effective average barrier thickness of 67.2 nm. In comparison, sample Cx0240 contains triplets of QWs separated by 10 nm barriers, with thicker separating barriers of 125 nm. The results of the strain analysis are summarized in Table 3.1.
As shown in Table 3.1, sample Bx0240 clearly demonstrates reduced average and excess strain due to the inclusion of thick intermediate barriers, despite having the same indium content as Ax0241.

Table 3.1: Strain and critical thickness analysis of the investigated samples. Samples labeled with "A" feature thin barriers, "B" samples adopt a coupled-well design, and "C" samples use a triplet-well design. The number following "x" indicates the In content in the MQWs.

Sample	In (%)	t_w (nm)	t_b (nm)	N wells	$\langle f \rangle$ (%)	T_{eq} (nm)	f_{eq} (%)	$\langle f_{\mathrm{ex}} \rangle$ (%)
Ax0183	18.3	6.6	7.0	12	0.667	17.61	0.148	0.518
Ax0225	22.5	4.6	7.1	12	0.669	13.61	0.165	0.504
Ax0232	23.2	5.0	7.1	12	0.724	13.10	0.158	0.566
Ax0256	25.6	5.0	7.0	12	0.805	11.57	0.155	0.650
Ax0241	24.1	4.2	7.3	12	0.667	12.49	0.165	0.502
Bx0240	24.0	4.1	67.2	12	0.106	12.55	0.027	0.079
Cx0240	24.0	7.0	38.8	9	0.291	12.55	0.058	0.233

Figure 3.3 plots the excess strain as a function of the number of QWs for different design strategies. The model indicates that only structures with one to three wells remain below the critical strain threshold, whereas for larger numbers of wells the strain invariably exceeds the critical limit, regardless of the design.
The model was originally developed for “thick” QWs around 10 nm and barriers up to 50 nm. Because the present samples employ thinner wells and, in some cases, significantly thicker barriers, experimental validation was performed. The investigated samples were grown under conditions optimized for high-quality InGaAs layers: GaAs was deposited at a rate of 720 $\mathrm{nm\,h^{-1}}$, while InGaAs growth rates ranged between 790 $\mathrm{nm\,h^{-1}}$ and 940 $\mathrm{nm\,h^{-1}}$. During InGaAs deposition, the Beam Equivalent Pressure Ratios (BEPRs) of As to Ga and As to In were maintained at 11 and 12, respectively. Each structure was capped with a 20 nm GaAs layer to ensure surface protection. These calibrated conditions were based on previous studies and verified to provide reproducible material quality in our system.

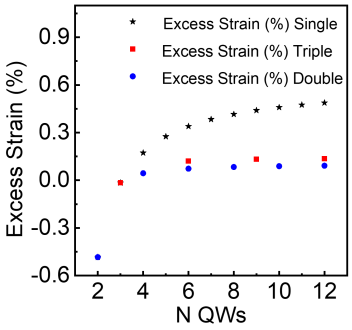

Figure 3.3: Excess strain as a function of the number of QWs for different MQW designs. Black stars represent a structure with uniform barriers of 119 nm. Blue dots correspond to an alternating barrier design with thin (7 nm) and thick (119 nm) barriers. Red squares indicate a triplet design, where two 7 nm barriers are separated by a thicker 199 nm barrier.

RTPL Map

After growth, PL spectra were measured for each sample and the maxima of the spectra were identified. The intensity of the emission at the energy corresponding to the maximum of each sample was then mapped to evaluate the homogeneity of the emission. The maps obtained are shown in Figure 3.4.
In all maps except for Figure 3.4(f), lines of reduced emission are visible. The first step was to exclude the possibility that these features originated from spectral shifts along these lines. For each sample, PL spectra were measured at different positions. The results for one representative sample are shown in Figure 3.5. In all cases the behavior was consistent: the peak emission energy did not shift with position, while the emission intensity varied, as suggested by the maps.
In Figure 3.4(a), no intensity reduction lines are visible except in the top-right corner, while in Figure 3.4(f) they are absent altogether. To gain further insight, µPL mapping was performed.

µPL Map

µPL mapping provides higher spatial resolution and was used to verify the results obtained from RTPL. Selected maps are shown

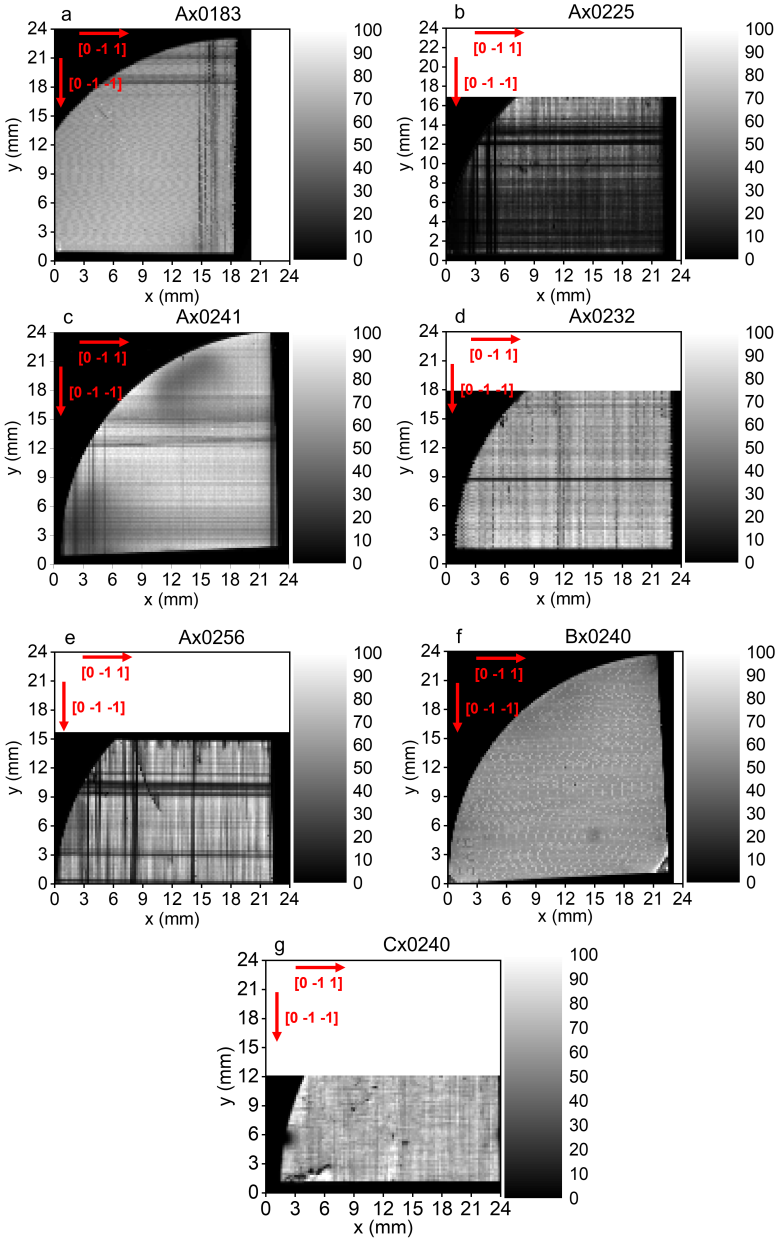

Figure 3.4: RTPL maps of seven samples with crystallographic directions highlighted. (a) to (e) MQWs with different In contents from 18 % up to 26 % separated by 7 nm barriers. (f) A pair of QWs separated by 119 nm barriers. (g) Triplets of QWs separated by 125 nm barriers.

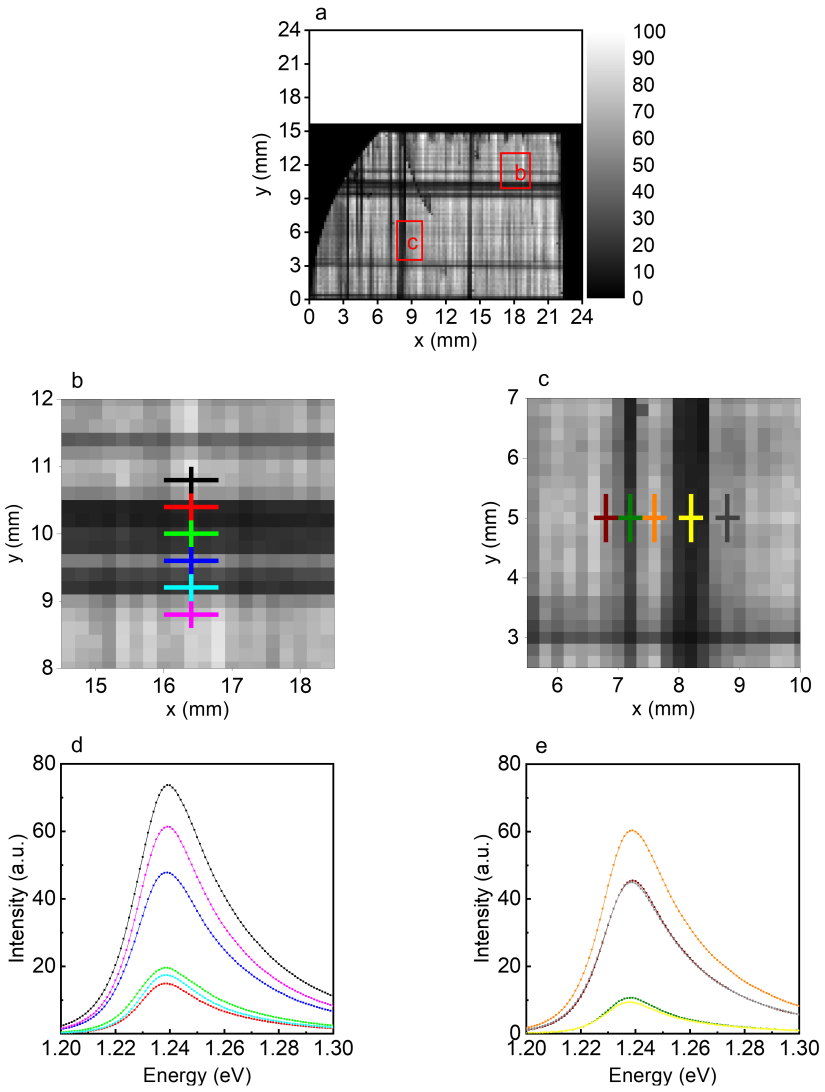

Figure 3.5: (a) RTPL map of sample Ax0256. The two rectangles indicate the regions analyzed in detail. (b) Zoomed-in view of the area $14.5 \leq x \leq 18.5$, $8 \leq y \leq 12$. (c) Zoomed-in view of the area $5.5 \leq x \leq 10$, $2.5 \leq y \leq 7$. (d) PL spectra measured along $x = 16.4$ for six different y values. Each spectrum was acquired at the spot marked by the cross of the corresponding color. (e) PL spectra measured along $y = 5$ for five different x values. Each spectrum was acquired at the spot marked by the cross of the corresponding color.

in Figure 3.6. They reveal sub-micrometer features unresolved in RTPL. For example, Ax0183 appears homogeneous in RTPL, but µPL mapping uncovers faint emission-suppression lines. These lines align with crystallographic directions [0-11] and [0-1-1], consistent with MD orientations.
The µPL map of sample Bx0240 in Figure 3.6(e) does not exhibit emission-suppression lines, confirming the RTPL observations and suggesting that this structure is essentially free of MDs, or at least that their density is drastically reduced compared to the other structures, such that they do not affect emission homogeneity.

AFM Map

Atomic Force Microscopy (AFM) imaging provides complementary surface morphology information correlated with dislocations [81]. Sample Ax0241 shows stepped surface topography and pits consistent with MDs, while Bx0240 exhibits a smoother profile, confirming that its barrier engineering suppresses dislocation propagation, as shown in Figure 3.7(Top). Additionally, Transmission Electron Microscopy (TEM) images taken from the edge of a double-QW design show no visible dislocations, while High-Resolution Transmission Electron Microscopy (HR-TEM) confirms a good crystalline structure, as shown in Figure 3.7(Bottom).

Conclusion

The analysis of these samples allowed us to verify the conditions for the validity of the strain model. The model correctly predicts the increase in strain during InGaAs growth on GaAs when the QWs are separated by thin barriers. For the In content, QW thickness, and barrier thickness used, the model predicts that the excess strain becomes greater than zero when the number of wells exceeds three, is zero for three wells, and remains below zero for one or two wells. When applied to coupled and triplet designs with thick barriers, the model predicts increasing $\langle f_{\mathrm{ex}} \rangle$ with the number of wells, implying MD formation. Our measurements confirm this behavior for triplet structures, while no dislocations are observed in coupled-well samples. This is likely because the thick barriers separating the pairs effectively reset the accumulated strain, a mechanism not

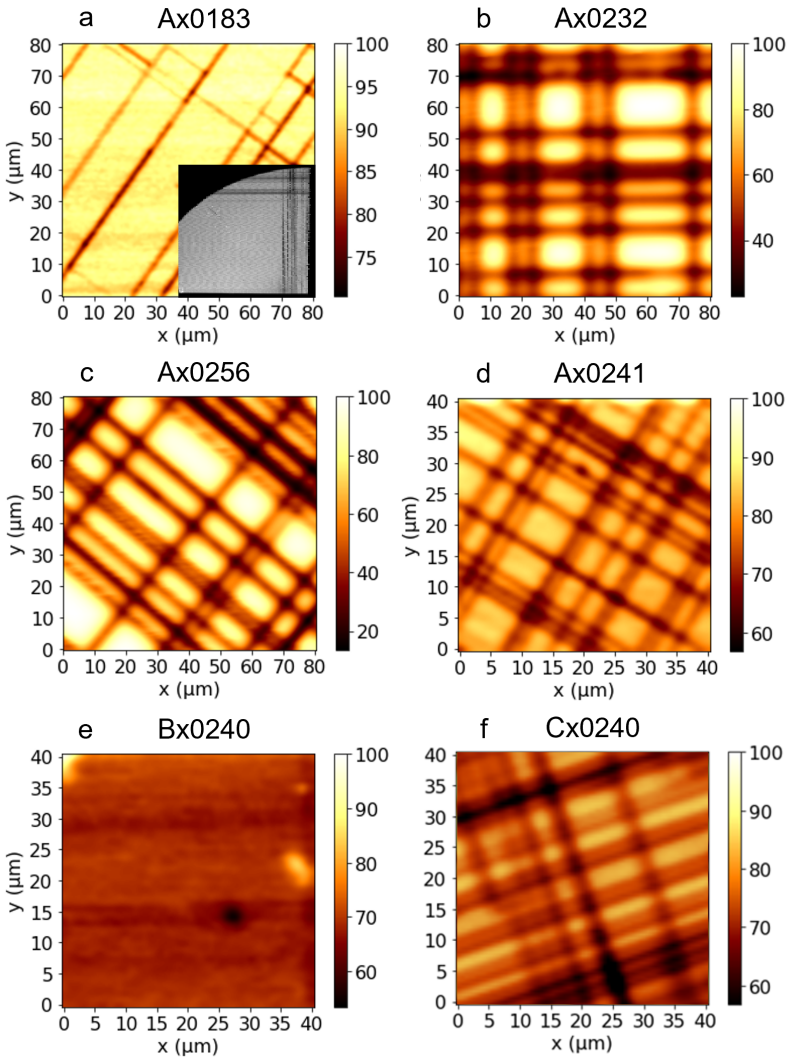

Figure 3.6: µPL measurements of five samples: Ax0183, Ax0232, Ax0256, Ax0241, and Bx0240. The scanned area for each map is 80×80 µm^2. The crystallographic directions along which the line features appear are [0 −1 −1] and [0 −1 1], as indicated in Figure 3.4. (a) Map of sample Ax0183; the inset shows the corresponding RTPL map with the µPL scan area highlighted by a rectangle. (b) Map of sample Ax0232. (c) Map of sample Ax0256. (d) Map of sample Ax0241. (e) Map of sample Bx0240.

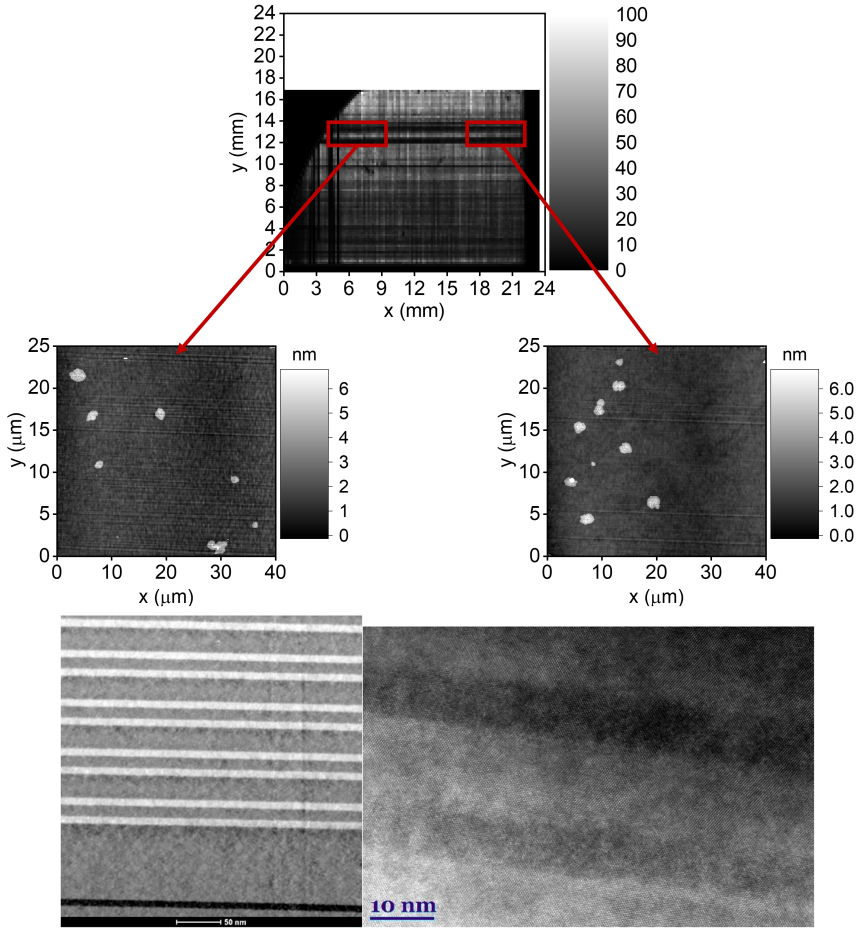

Figure 3.7: (Top) RTPL map of sample Ax0256 with two highlighted areas where AFM measurements were performed. (Bottom) TEM and HR-TEM images of a sample consisting of six pairs of QWs, taken from the edge, showing the MQW region along the growth direction.

accounted for in the model.
These results suggest that the thinnest InGaAs-based VECSEL structure that still ensures coupling between the QWs and the optical mode is one in which the wells are paired. Designs employing triplets of QWs are more prone to dislocation formation, which reduces the effective gain area and promotes hot-spot generation.

3.1.3. Carrier Thermalization and Barrier Design

To enhance carrier confinement and optical efficiency of InGaAs QWs for NIR emission, we investigated the influence of aluminum concentration in AlGaAs barriers. The objective was to determine the optimal Al content that maximizes radiative recombination efficiency while minimizing detrimental non-radiative processes.

Simulations

The structures were numerically studied using the `nextnano`[3] software package, which enables one-dimensional full-band quantum mechanical simulations along the growth axis. The band structure was calculated within an 8×8 Hamiltonian in the effective mass approximation. Only the conduction band minimum at the Γ point and the heavy-hole and light-hole valence band maxima were considered. Excitonic effects and the temperature dependence of the band gap were included in the calculations.
Four single-QW structures were designed with a fixed well thickness of 5.7 nm and an indium content of 20.8 %. The barriers consisted of either GaAs (sample A0) or $Al_xGa_{1-x}As$ with aluminum fractions of $x = 0.12$ (A12), $x = 0.20$ (A20), and $x = 0.30$ (A30). All barrier layers were 15 nm thick. The simulated band-edge profiles and confined energy levels are shown in Figure 3.8, where increasing aluminum concentration leads to progressively stronger quantum confinement.

Room Temperature Photoluminescence

The simulated structures were subsequently grown and characterized by RTPL. The measured spectra, shown in Figure 3.9, reveal

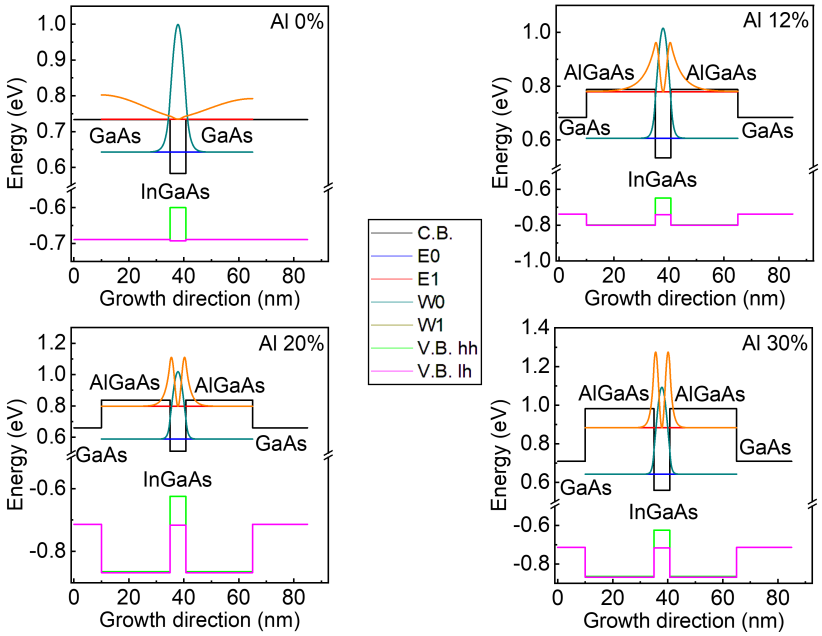

Figure 3.8: Calculated band-edge profiles and confined states for the four barrier designs: GaAs barriers (A0), $Al_{0.12}Ga_{0.88}As$ (A12), $Al_{0.20}Ga_{0.80}As$ (A20), and $Al_{0.30}Ga_{0.70}As$ (A30).

two main effects.
First, despite the different barrier compositions, the emission energy remains nearly unchanged across the four samples, in contrast to the expectations from band structure simulations. Second, although the inclusion of aluminum increases the emission intensity compared to the GaAs barrier reference (A0), further increasing the aluminum fraction beyond 12 % results in a decrease in intensity. This suggests that two competing processes are at play.

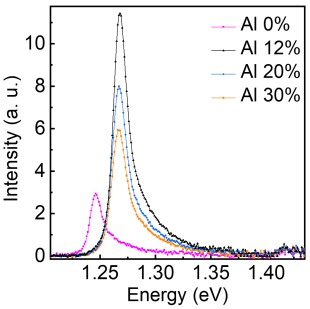

Figure 3.9: RTPL spectra of the four samples under identical excitation conditions.

Analysis of PL Peak Energies

To better understand the absence of energy shifts, experimental and simulated emission peak energies were compared, as summarized in Table 3.2. A discrepancy is evident in some samples, prompting consideration of three possible explanations.
The first possibility is imprecise calibration of the Al flux during MBE growth, which could have led to unintentional barrier compositions. However, this is unlikely since GaAs and AlGaAs exhibit excellent lattice matching, producing clear RHEED oscillations that allow reliable monitoring of Al content.
A second explanation is variation in QW thickness. Due to weak RHEED oscillations in InGaAs, small growth-rate errors are possible. For example, a 1.5 % deviation from the nominal thickness of 5.7 nm would yield a well thickness of approximately 5.8 nm, sufficient to influence transition energies. However, these thin single-QW structures are not suitable for confirmation via XRD.
A third explanation is variation in indium composition. A small

Table 3.2: Comparison of experimental and calculated PL emission energies with nominal and estimated indium content for different Al concentrations in the barrier.

Al content (%)	Experimental Emission (eV)	Calculated Emission (eV)	Nominal In (%)	Estimated In (%)
0	1.2452	1.2609	20.8	21.5
12	1.2675	1.2664	20.8	21.0
20	1.2674	1.2726	20.8	21.4
30	1.2667	1.2787	20.8	21.8

growth-rate error of 1.5 % could shift the In fraction from 20.8 % to about 22 %. This would produce a measurable redshift in the emission energy.
To evaluate these hypotheses, additional simulations were performed, varying both the QW thickness and indium content. The results, shown in Figure 3.10, suggest that sample A0 and A20 likely contained ∼21.5 % indium, A12 about 21.0 %, and A30 about 21.8 %.

Power-Dependent PL Intensity

To probe recombination mechanisms, excitation power-dependent PL was measured. The integrated intensity I was analyzed as a function of excitation power P in log–log scale and fitted with a power law $I \propto P^k$. For ideal radiative recombination $k \approx 1$. Sample A0 exhibited the exponent closest to unity, indicating radiative dominance. In contrast, A12, A20, and A30 showed progressively higher k values ($k_{A30} > k_{A20} > k_{A12} > 1$), reflecting stronger non-radiative contributions at higher Al contents and suggesting degradation of crystalline quality. These results do not explain why the higher-Al samples display stronger RTPL despite reduced crystalline quality, motivating further investigation with temperature-dependent measurements.

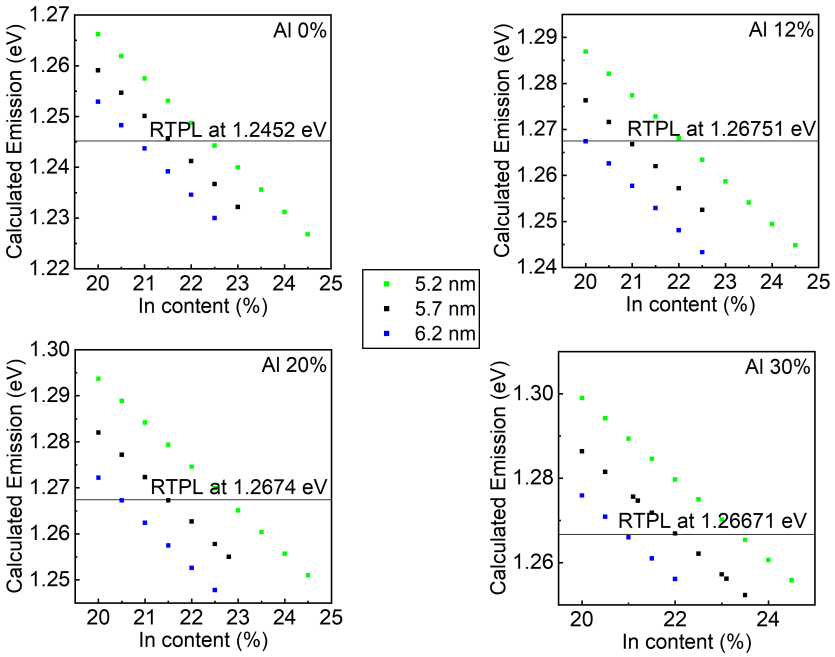

Figure 3.10: Simulated transition energies as a function of QW thickness and indium concentration, compared to experimental PL peak energies for different barrier compositions.

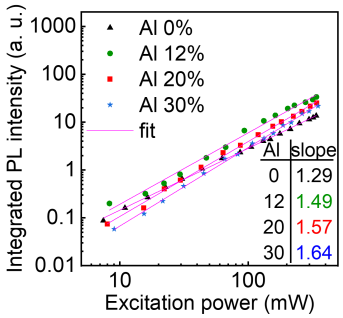

Figure 3.11: Integrated PL intensity as a function of excitation power, plotted on a double logarithmic scale. Measurements were performed on samples A0 (black triangles), A12 (green circles), A20 (red squares), and A30 (blue stars). A linear fit to the data is shown in red, with slope values listed in the inset table.

Temperature-Dependent PL

TDPL was performed between 4 K and 300 K using a reduced excitation density of 174 W cm^{-2} to suppress heating effects. Figure 3.12(a) shows the spectra of sample A12. The temperature evolution of the emission peak position, shown in Figure 3.12(b), was fitted with the Varshni relation:

$$E_g(T) = E_0 - \frac{\alpha T^2}{T + \beta} \tag{3.7}$$

where E_0 is the bandgap at 0 K, α describes the temperature coefficient of the bandgap, and β is an empirical parameter associated with phonon interactions [82]. The extracted fitting parameters are summarized in Table 3.3.
At low temperatures, the GaAs-barrier sample A0 exhibits the high-

Table 3.3: Fitting parameters of the Varshni relation for the TDPL peak shift of samples A0, A12, A20, and A30.

Sample	E_0 (eV)	α (meV/K)	β (K)
A0	1.332 ± 0.001	0.68 ± 0.04	428 ± 41
A12	1.350 ± 0.001	0.65 ± 0.04	
A20	1.354 ± 0.001	0.66 ± 0.04	
A30	1.350 ± 0.001	0.67 ± 0.04	

est intensity, consistent with the power-dependent PL analysis. Its intensity decreases rapidly above 75 K and converges with the Al-containing samples by around 200 K, as shown in Figure 3.12(c). At room temperature, A0 shows the weakest emission, while A12 exhibits the strongest, consistent with the RTPL results.

Conclusions

The combined simulations and experimental results show that increasing Al content in AlGaAs barriers enhances carrier confinement but simultaneously degrades crystalline quality through the introduction of additional non-radiative centers. The negative impact becomes more pronounced above 12 % Al.

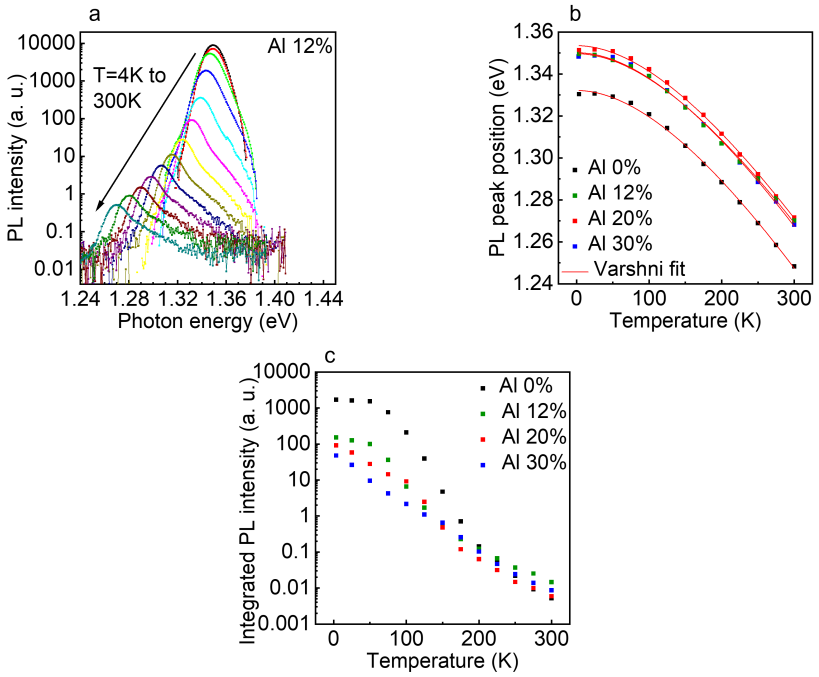

Figure 3.12: (a) TDPL spectra of sample A12 from 4 K to 300 K. (b) Temperature dependence of the TDPL peak position with Varshni fits, Equation 3.7. (c) Integrated intensity for samples A0, A12, A20, and A30 over the same temperature range measured with excitation power of 29 mW.

Sample A12 provides the best compromise, maintaining sufficient crystalline quality while improving carrier confinement to suppress thermal escape at elevated temperatures. Consequently, A12 achieves the highest room-temperature emission intensity. Nevertheless, in this work, GaAs barriers (A0) were used in device structures to prioritize crystalline quality in the gain region. The use of Al-containing barriers remains an attractive strategy to explore further for enhancing device lasing performance.

3.2. GaAsBi Growth Optimization

The second compound analyzed is GaAsBi. The main advantages of using GaAsBi for NIR emitters, introduced in Section 1.1, are its strong bandgap reduction, enabling emission at longer wavelengths without requiring excessively high Bi concentrations. In addition, GaAsBi exhibits a large spin–orbit splitting energy, which can suppress Auger recombination at longer wavelengths, furthermore, the incorporation of Bi provides improved temperature stability of the emission compared to conventional III–V alloys.
Unlike InGaAs, GaAsBi has not yet been demonstrated in VECSEL structures, and no reference devices are currently reported in the literature. Therefore, optimizing the growth and design of GaAsBi quantum structures in our system is essential to ensure high optical quality and to maximize the likelihood of successful device fabrication. In this work, we focus on four key aspects: the study of stress and dislocation formation, the effect of growth temperature on GaAsBi layers, the effect of annealing on emission properties, and the internal quantum efficiency of GaAsBi.

3.2.1. GaAsBi Stress and Dislocations

The first step was to analyze the excess stress arising from lattice mismatch. Since the lattice constant of GaBi is not precisely known, the lattice mismatch between GaAsBi and GaAs is difficult to calculate, making the evaluation of the critical thickness and accumulated stress in GaAsBi layers less straightforward. The mismatch for layers containing up to 3.1 % Bi has been calculated and the critical thickness estimated in the literature [2]. However, to achieve emission at wavelengths longer than 1 µm, a significantly higher Bi content must be introduced into the QW layers. It is therefore necessary to investigate the stress and its influence on dislocation formation at higher Bi concentrations.
GaAsBi layers 100 nm thick, with Bi contents up to 11.2 %, were grown on ultra-thin GaAs buffer layers to evaluate stress accumulation, relaxation thresholds, and surface morphology. The results of XRD characterization are shown in Figure 3.13. Figure 3.13(a) presents the rocking curves of the (004) reflection for layers with increasing Bi content. The vertical lines indicate the expected peak

positions for fully strained layers. Figures 3.13(b)–(d) show reciprocal space maps of the (115) reflection for layers containing 0.97 %, 3.1 %, and 11.2 % Bi. The red lines mark the fully strained (vertical) and fully relaxed (tilted) states. The slight offset of the measured peaks from the strained line confirms that the layers remain largely strained, with minimal relaxation even at the highest Bi content.
These results, published in [A1], confirmed that GaAsBi can accom-

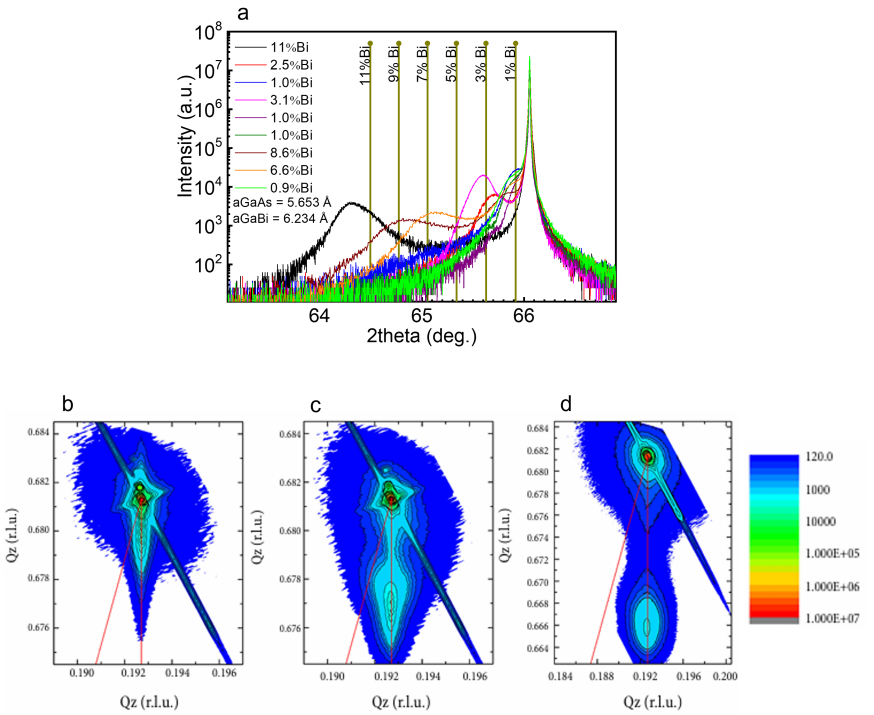

Figure 3.13: X-ray diffraction characterization of GaAsBi layers epitaxially grown on GaAs substrates. (a) XRD rocking curves of the (004) reflection for 100 nm-thick layers with Bi contents from 0.97 % to 11.2 %. Vertical lines indicate the positions expected for fully strained GaAsBi layers. (b)–(d) Reciprocal space maps of the (115) reflection for layers with 0.97 %, 3.1 %, and 11.2 % Bi, respectively.

modate relatively high Bi concentrations without significant relaxation. Following this study on thick layers, the stress behavior was further investigated in MQWs, using the same approach described in subsection 3.1.2 for InGaAs structures.

Heterostructures containing 5 to 12 GaAsBi MQWs with varying Bi contents were grown, using thin GaAs barriers of 7 nm thickness. The spatial homogeneity of the emission was examined by mapping the RTPL. Examples of two representative structures are shown in Figure 3.14, where (a) contains 12 QWs and (b) contains 5 QWs. In contrast to InGaAs-based MQWs, these GaAsBi structures do not exhibit lines of reduced emission in the maps. This indicates that the critical thickness for GaAsBi layers with Bi contents below 10 % is significantly higher than that of $In_{0.2}Ga_{0.8}As$ layers, consistent with the observations made for thick GaAsBi layers.

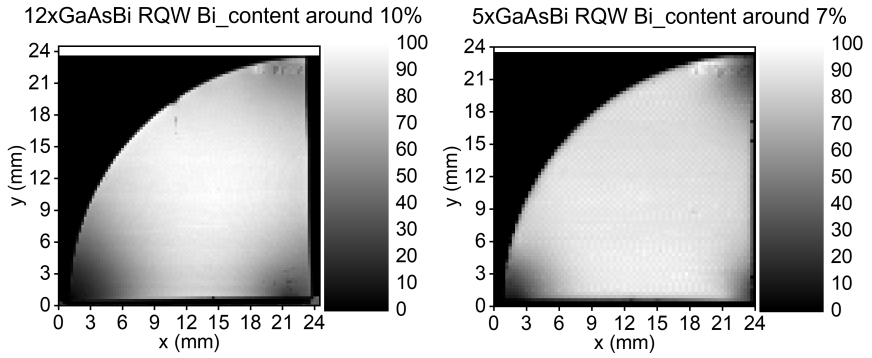

Figure 3.14: RTPL maps of GaAsBi MQWs. On the left a sample containing 12 QWs emitting at 1.084 eV (1143 nm), while on the right a sample containing 5 QWs emitting at 1.128 eV (1100 nm).

3.2.2. Growth Parameters Optimization

The incorporation of Bi into the GaAs lattice during epitaxial growth is primarily governed by three parameters: the fluxes of As, Ga, and Bi. Among these, the arsenic-to-gallium flux ratio and the substrate temperature play particularly critical roles.

Optimization of As_2/Ga Ratio and Bi Flux

The optimal arsenic-to-gallium flux ratio lies in the range 1.0–1.2, as shown in Figure 1.4, adapted from [83]. Calibrating this ratio is not straightforward because the beam flux monitor in the growth chamber measures the BEP at the filament located below the substrate. While BEP is proportional to the atomic flux, it also

depends on the chamber geometry and the position of the source relative to the measurement point. As a result, the measured BEP does not directly represent the flux incident on the wafer, requiring additional calculations for accurate calibration.
To optimize this ratio, a series of samples was grown, each containing three GaAsBi/GaAs QWs (5.5 nm thick) separated by 7 nm GaAs barriers. The BEPR and the Bi source base temperature (directly linked to Bi flux) were varied, while the GaAs growth rate and Ga flux were kept constant. The As flux was modulated by adjusting the valve opening. RTPL measurements were then performed to evaluate Bi incorporation. Figure 3.15 shows the emission energy as a function of the growth parameters: (a) versus As_2/Ga BEPR, and (b) versus Bi source temperature. The tip temperature was adjusted to maintain a fixed offset relative to the source base. No systematic trend was observed between emission energy and

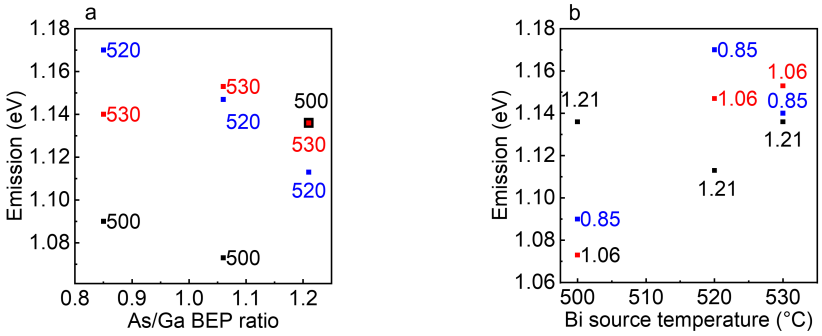

Figure 3.15: PL emission energy of samples grown under different conditions. (a) Dependence on the As_2/Ga BEPR. Numbers next to each point indicate the Bi source temperature: black for 500 °C, blue for 520 °C, and red for 530 °C. (b) Dependence on Bi source temperature. Numbers next to each point indicate the As_2/Ga BEPR: blue for 0.85, red for 1.06, and black for 1.21.

either parameter. This suggests that, within this regime, Bi incorporation is not limited by the As_2/Ga ratio or by Bi flux.

Comparison of Temperature Measurement Techniques

The next parameter investigated was substrate temperature. In our reactor, two methods are available for temperature monitoring: a thermocouple located between the heater and the sample holder,

and the BandiT system.
The thermocouple provides fast and stable temperature control through direct feedback to the heater. However, since it is not in direct contact with the wafer, it systematically overestimates the actual substrate temperature. In contrast, the BandiT system measures the absorption edge of the wafer and therefore directly probes the substrate temperature. Despite its advantages, this system has several limitations: it requires calibration that depends on the optical properties of the wafer, it cannot be used in a closed-loop feedback mode, readings are interrupted when the growth shutter is closed, and in our system it operates only in transmission mode, which relies on heater-emitted radiation and becomes unreliable at low temperatures.
Given these drawbacks, calibration of the thermocouple was pursued to allow reproducible device growth.

Growth Series Using Thermocouple Readings

To study the influence of growth temperature, another series of samples was fabricated, each consisting of three rectangular GaAsBi QWs (5.5 nm thick) separated by 7 nm GaAs barriers. The thermocouple setpoint was varied from 425 °C to 460 °C. The Bi source temperature was fixed at 510 °C, and the As_2/Ga BEPR was maintained in the range 1.03–1.08. The emission energy as a function of thermocouple temperature is shown in Figure 3.16.
No consistent dependence was observed. Samples grown at the

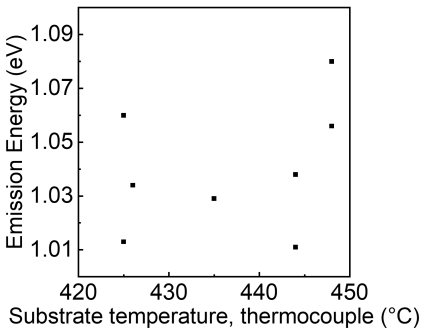

Figure 3.16: Emission energy of GaAsBi samples grown at different thermocouple setpoints, with constant Bi source temperature and As_2/Ga BEPR.

same nominal temperature showed large variations in emission en-

ergy, confirming that thermocouple readings alone are not sufficiently reliable for accurate growth optimization.

Temperature Monitoring with BandiT

Due to the limitations of thermocouple control, the BandiT system was used to re-evaluate the effect of growth temperature. The challenges of this method were addressed as follows: calibration was carried out using manufacturer-supplied parameters, operating in transmission mode to ensure the signal originated from the wafer bulk; direct feedback was not possible, but thermocouple setpoints were calibrated manually against BandiT readings before each growth; shutter-induced signal interruptions remained unresolved, with readings dropping to zero whenever the shutter was closed; and reliability at low temperatures was limited due to heater fluctuations.
Figure 3.17 shows a typical BandiT trace during the growth of a sample containing seven GaAsBi QWs. Each shutter closure causes the reading to fall to zero, after which the temperature signal recovers during barrier deposition. A slow overall drift is also visible. For each QW, the final BandiT value before shutter closure was

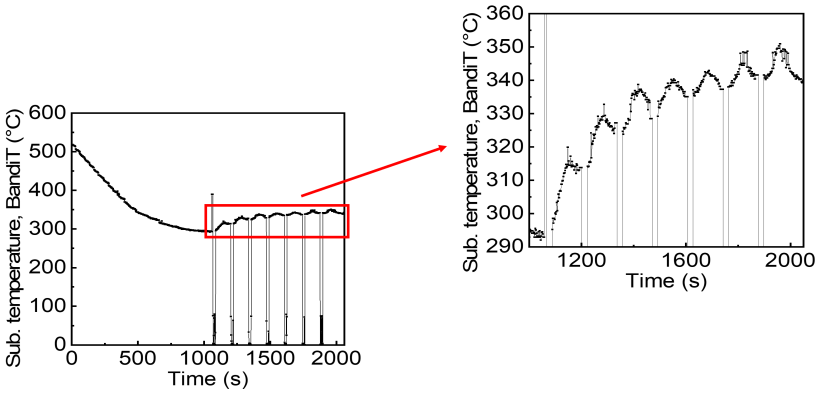

Figure 3.17: BandiT temperature trace during the growth of a seven-QW GaAsBi sample. Red boxes highlight zoomed-in regions around shutter closures.

recorded and correlated with the emission energy of the structure. Figure 3.18 shows these correlations for the first, second, and third QWs, as well as the average across all three. A strong linear dependence is observed in all cases. The slopes of the linear fits are

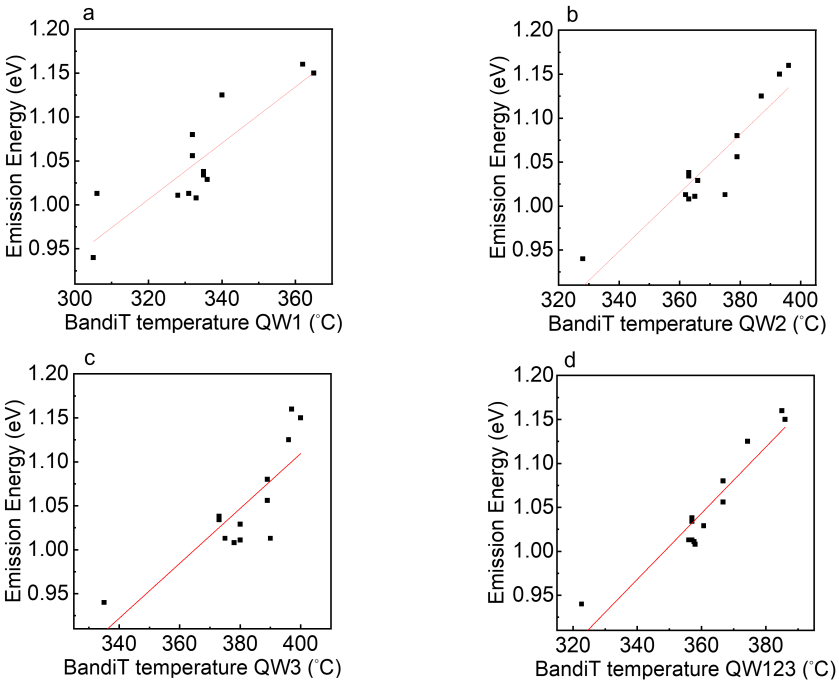

Figure 3.18: Emission energy of GaAsBi samples as a function of BandiT growth temperature. (a)–(c): Temperature before the first, second, and third QWs. (d): Average of all three. Red lines show linear fits.

Table 3.4: Linear fit parameters for the correlations in Figure 3.18. RSS is the residual sum of squares; Pearson coefficient r quantifies correlation strength; R^2 represents the variance explained; and adjusted R^2 accounts for the sample size and model complexity.

Fit	Intercept (eV)	Slope$\times 10^{-4}$ (eV°C^{-1})	RSS	Pearson r	R^2	Adj. R^2
1st QW	0.0 ± 0.2	32 ± 6	0.012	0.864	0.747	0.724
2nd QW	-0.2 ± 0.2	33 ± 4	0.007	0.924	0.854	0.841
3rd QW	-0.1 ± 0.2	31 ± 6	0.015	0.827	0.684	0.655
Average	-0.3 ± 0.2	38 ± 4	0.005	0.943	0.889	0.879

consistent, averaging $b = 0.0037 \pm 0.0004$ eV °C^{-1}. This confirms a strong temperature dependence of Bi incorporation, demonstrating that within our growth regime, Bi incorporation is limited by substrate temperature.
The same behavior is evident when plotting emission energy as a function of BandiT temperature for samples grown with different As_2/Ga ratios and Bi source temperatures. Figure 3.19 shows that regardless of these variations, the emission energy scales linearly with the growth temperature, further confirming that Bi incorporation is primarily temperature-limited.

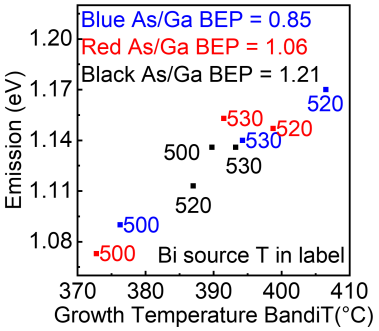

Figure 3.19: Emission energy as a function of BandiT growth temperature for samples grown under different conditions. Colors represent As_2/Ga BEPR values (blue: 0.85, red: 1.06, black: 1.21). Numbers next to each point indicate Bi source temperature.

Conclusion and Calibration Strategy

Based on the results, a calibration procedure was established to correlate thermocouple setpoints with target BandiT temperatures prior to growth. This approach enables precise and repeatable control of the substrate temperature, which in turn governs Bi incorporation and the resulting emission energy of GaAsBi QWs. At higher substrate temperatures (above 450 °C, BandiT reading), the temperature measurements became more stable, and no significant difference was observed during the growth of layers consisting of different compounds. Furthermore, the variation in measured temperature between different growths performed at the same nominal substrate temperature was minimal. In particular, thermocouple readings were found to systematically overestimate the actual substrate temperature by approximately 50 °C.

3.2.3. Annealing Temperature Effects

In complete device structures, such as LEDs, LDs, and VECSELs, the growth of the active region is followed by additional layers, including contact, waveguide, and window layers. These layers are typically composed of (Ga,Al)As, which require significantly higher growth temperatures than GaAsBi to achieve optimal crystalline quality. Consequently, it is important to evaluate the effect of post-growth temperature increases on the structural and optical properties of GaAsBi QWs.

A series of samples was grown, each consisting of two GaAsBi MQWs grown at 350 °C, capped by 7 nm GaAs at the same temperature, followed by an additional 7 nm GaAs layer deposited either at the same temperature or at 570 °C. The structural parameters of the investigated samples are summarized in Table 3.5. The corresponding RTPL spectra are shown in Figure 3.20.

Two key effects were observed. First, a blue shift of approximately 50 meV was detected in samples capped with High Temperature (HT) GaAs, indicating an intrinsic modification of the quantum wells. This shift is attributed to Bi segregation toward the upper interface of the QW, resulting in regions with a reduced Bi concentration and consequently a higher transition energy. Second, samples subjected to in-situ annealing exhibited more than a twofold increase in PL intensity. This enhancement is attributed to a reduction in non-radiative recombination, likely due to improved crystallinity of the LT GaAsBi layers following annealing, which reduces defect density.

These results highlight the need to account for the annealing-induced blue shift when designing emitters for specific wavelengths. Furthermore, as demonstrated in our published work [84], a further increase in annealing temperature can lead to the formation of Bi QDs through segregation. Since this work focuses on QW-based devices, subsequent overgrowth of layers above the MQW region was restricted to 570–580 °C.

3.2.4. GaAsBi Internal Quantum Efficiency

The IQE of GaAsBi/GaAs MQW structures was extensively investigated to assess their potential as gain media for VECSELs. The studied samples consisted of 12 QWs (5.5 nm thick). Sample 1

Table 3.5: Structural parameters of the VGA GaAsBi samples.

Sample	GaAsBi T (°C)	Cap T (°C)	QW thick. (nm)	Barrier (nm)
GaAsBi+HT_GaAs	350	570	5.5	7
GaAsBi+LT_GaAs	350	350	5.5	7

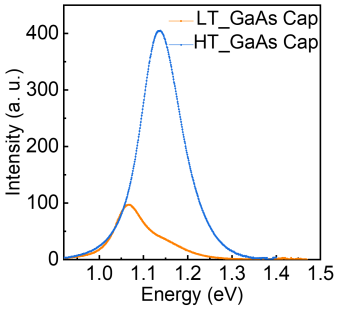

Figure 3.20: RTPL spectra of GaAsBi samples capped with low-temperature (LT) or high-temperature (HT) GaAs layers.

included alternating GaAs barriers of 7 nm and 150 nm to align the QW emission with the optical standing wave, whereas sample 2 used uniform 7 nm barriers. The GaAsBi layers were grown at 425 °C (sample 1) and 435 °C (sample 2). In both cases, the cap layers were grown at high temperature.

Photoluminescence and Carrier Localization

RTPL spectra revealed emission at 1.058 eV for sample 1 and 1.085 eV for sample 2, corresponding to Bi contents of 7.6 % and 7.1 %, respectively. TDPL measurements exhibited characteristic S-shaped energy shifts, indicative of strong carrier localization, which persisted up to 300 K. The TDPL peak energy and integrated PL intensity of sample 1 are shown in Figure 3.21. The data were fitted using the Varshni–Eliseev model [85]:

$$E_g(T) = E_0 - \frac{\alpha T^2}{\beta + T} - \frac{\sigma^2}{k_B T}, \tag{3.8}$$

yielding localization energies of 30 meV. Thermal quenching was analyzed using a double-activation Arrhenius model:

$$I(T) = \frac{I_0}{1 + a_1 \exp\left(-\frac{E_{a1}}{k_B T}\right) + a_2 \exp\left(-\frac{E_{a2}}{k_B T}\right)}, \tag{3.9}$$

which produced activation energies of $E_{a1} = 9.5 \pm 0.1$ meV and $E_{a2} = 45.9 \pm 1.1$ meV. The lower value is associated with non-radiative recombination via Bi pairs and clusters, while the higher value is attributed to structural inhomogeneities [86].

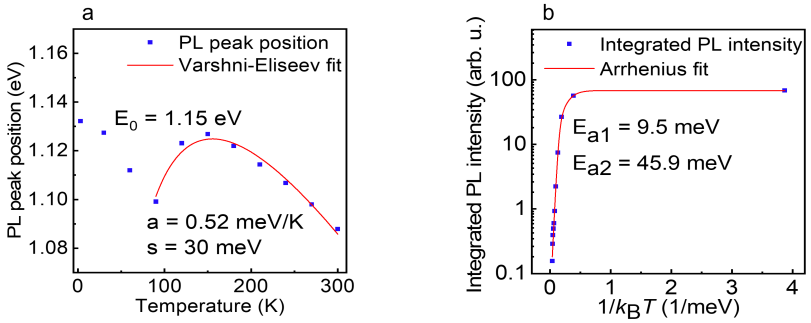

Figure 3.21: Results of TDPL measurements for sample 1. (a) Temperature dependence of the PL peak position with experimental data (symbols) and Varshni–Eliseev fit (solid curve, Equation 3.8). (b) Temperature dependence of the integrated PL intensity with experimental data (symbols) and Arrhenius fit (solid line, Equation 3.9).

IQE Estimation Methods

Multiple methods were used to estimate IQE, revealing significant discrepancies:

- HT/LT Method and Power-Normalized TDPL: These relative methods yielded very low IQE values (0.1–0.4 %), these methods are limited by the non-ideal assumptions and inaccuracies. These were measured with a 532 nm laser at a poer of 4 mW.
- Standard ABC Model [87]: Power-dependent PL under 532 nm excitation was fitted using the classical ABC rate equation. This approach produced high IQE values of around 21 % for both samples.

- Absolute IQE via Integrating Sphere: Using an 830 nm CW laser and an Edinburgh Instruments integrating sphere setup, the absolute IQE at a exitation power of 140 mW was measured to be as low as 0.010 % (sample 1) and 0.013 % (sample 2), highlighting the strong influence of non-radiative recombination caused by defects, alloy disorder, and Bi-induced strain.

Modified ABC Model

The ABC model estimates IQE from RTPL measurements as a function of excitation power by considering three recombination mechanisms: non-radiative recombination (An), radiative recombination (Bn^2), and Auger recombination (Cn^3) [87,88]. The internal quantum efficiency is defined as:

$$\text{IQE} = \frac{Bn^2}{An + Bn^2 + Cn^3} = \frac{Bn^2}{R}. \tag{3.10}$$

The total generation rate R can be linked to the integrated PL intensity I_{pl} as:

$$R = \frac{A\sqrt{I_{\text{pl}}}}{\sqrt{B\eta}} + \frac{I_{\text{pl}}}{\eta} + \frac{C\sqrt{I_{\text{pl}}^3}}{(B\eta)^{3/2}}, \tag{3.11}$$

where η is a proportionality constant that accounts for PL collection efficiency and excitation volume. Alternatively, R can be expressed as a function of laser excitation power:

$$R = xP_{\text{laser}}, \tag{3.12}$$

where $x = \frac{(1-R_{\text{F}})\alpha}{A_{\text{spot}}h\nu}$, with R_{F} being the Fresnel reflection coefficient, α the absorption coefficient, A_{spot} the laser spot area, and $h\nu$ the photon energy. Combining Equations (3.11) and (3.12) gives:

$$P_{\text{laser}} = \frac{A\sqrt{I_{\text{pl}}}}{x\sqrt{B\eta}} + \frac{I_{\text{pl}}}{x\eta} + \frac{C\sqrt{I_{\text{pl}}^3}}{x(B\eta)^{3/2}}. \tag{3.13}$$

By introducing fitting parameters $P_1 = \frac{A}{x\sqrt{B\eta}}$, $P_2 = \frac{1}{x\eta}$, $P_3 = \frac{C}{x(B\eta)^{3/2}}$, this becomes:

$$P_{\text{laser}} = P_1\sqrt{I_{\text{pl}}} + P_2 I_{\text{pl}} + P_3 I_{\text{pl}}^{3/2}, \tag{3.14}$$

and the internal quantum efficiency can be expressed as:

$$\mathrm{IQE} = \frac{P_2 I_{\mathrm{pl}}}{P_1\sqrt{I_{\mathrm{pl}}} + P_2 I_{\mathrm{pl}} + P_3 I_{\mathrm{pl}}^{3/2}} = \frac{I_{\mathrm{pl}} P_2}{P_{\mathrm{laser}}}. \tag{3.15}$$

Fitting experimental PL intensity versus excitation power with Equation (3.14) yields P_1, P_2, and P_3. For sample 1, the fitted values were $P_1 = 5.3 \pm 0.6$, $P_2 = 0.07 \pm 0.01$, and $P_3 = 1 \times 10^{-17}$, as shown in Figure 3.22(a). This fitting method was selected because of the lack of known values for A,B and C in GaAsBi.
However, a discrepancy remained between the absolute IQE values and those derived from the standard ABC model. To address this, a modified ABC model was introduced, which incorporates an additional trap-assisted recombination term ($B'n^2$). This term accounts for trap-assisted Auger recombination (TAAR), which is prominent in LT-grown structures. Since the Auger recombination term (Cn^3) was found to be negligible, 3.22(a), it was removed [89]. The modified expression becomes:

$$\mathrm{IQE} = \frac{Bn^2}{An + Bn^2 + B'n^2}. \tag{3.16}$$

The generation rate is reformulated as:

$$R = P_1\sqrt{I_{\mathrm{pl}}} + P_2 I_{\mathrm{pl}} + P_2' I_{\mathrm{pl}}, \tag{3.17}$$

and the internal quantum efficiency in terms of the fitted parameters becomes:

$$\mathrm{IQE} = \frac{P_2 I_{\mathrm{pl}}}{P_1\sqrt{I_{\mathrm{pl}}} + P_2 I_{\mathrm{pl}} + P_2' I_{\mathrm{pl}}} = \frac{I_{\mathrm{pl}} P_2}{P_{\mathrm{laser}}}. \tag{3.18}$$

This modification enabled consistency between power-dependent and absolute IQE values without altering the fitting quality of the PL-versus-power curves (Figure 3.22(c)). For sample 1, the trap-assisted recombination parameter P_2' was three orders of magnitude larger than the radiative parameter P_2, confirming the dominant role of trap-assisted recombination in these structures. The very low absolute IQE values highlight the prevalence of non-radiative pathways in GaAsBi MQWs grown at low temperature. While the standard ABC and Shockley–Read–Hall models capture key recombination mechanisms, they fail to reproduce realistic efficiencies.

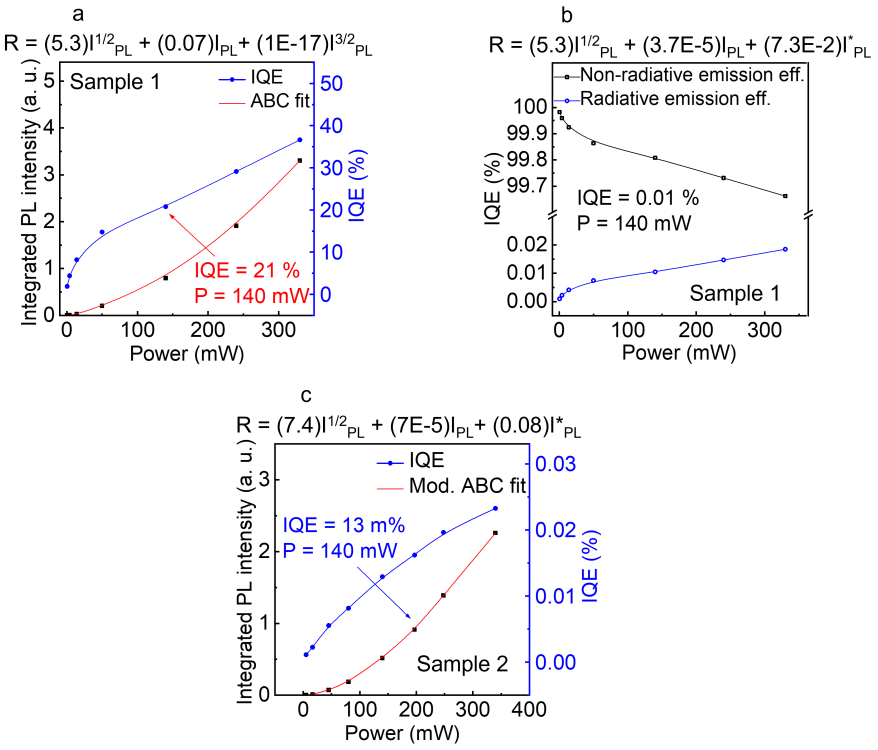

Figure 3.22: (a) Standard ABC model applied to sample 1: black markers are experimental data, red line is the fit from Equation 3.13, blue markers are IQE values from Equation 3.15. (b) Contribution of recombination mechanisms in sample 1 based on the modified ABC model. Black markers: non-radiative efficiency; blue markers: radiative efficiency from Equation 3.18. (c) Modified ABC model applied to sample 2: black markers are experimental data, red line is the fit from Equation 3.17, green markers are IQE values from Equation 3.18.

The modified ABC model resolves this discrepancy by accounting for trap-assisted processes. Further improvement of GaAsBi-based devices will depend on reducing defect densities through optimized growth and post-growth annealing. This model was also successfully tested on GaAsBi thick layers, confirming the high impact of trap-assisted recombination.

Summary

A growth window was established in which Bi incorporation is governed primarily by substrate temperature, allowing precise control of Bi content in GaAsBi layers. In our system, the optimal Bi source temperature was found to lie between 500–530 °C, with an As_2/Ga BEPR range of 0.85–1.2. For the remainder of this work, intermediate values of 510 °C and 1.0 were used.
It was further demonstrated that post-growth annealing at around 570 °C produces a blue shift in emission and an intensity increase, and will therefore be systematically applied in subsequent samples. The IQE of GaAsBi structures was measured and interpreted using the modified ABC model, which successfully explains the origin of their low efficiency by incorporating trap-assisted recombination effects.

3.2.5. Laser Diodes

The low IQE of GaAsBi-containing structures poses a significant challenge for laser fabrication. Nevertheless, given the capability within our team to process and characterize LDs, we proceeded with the fabrication of devices incorporating GaAsBi MQWs in order to evaluate whether their optical quality is sufficient to achieve lasing.

LD Growth

Two distinct active region geometries were designed and investigated: (i) standard rectangular quantum wells and (ii) Parabolically Graded Barrier (PGB) structures. Details on the growth of analogous parabolic grading can be found in [A2]. The fabricated structures were designated as RBi for rectangular GaAsBi QWs and PBi for parabolically confined GaAsBi QWs.
The band structures of both designs were simulated using `nextnano`^{3} software, employing a full-band, One-dimensional (1D)

quantum mechanical model along the growth axis. The 8×8 $\mathbf{k} \cdot \mathbf{p}$ method within the effective mass approximation was applied, including both HH and LH bands, as well as excitonic and temperature-dependent effects. Strain was neglected due to the approximate lattice matching between GaAsBi and GaAs at low Bi concentrations. Material parameters (bandgap, spin–orbit splitting, elastic constants, and offsets) were taken from established literature sources [72–75].

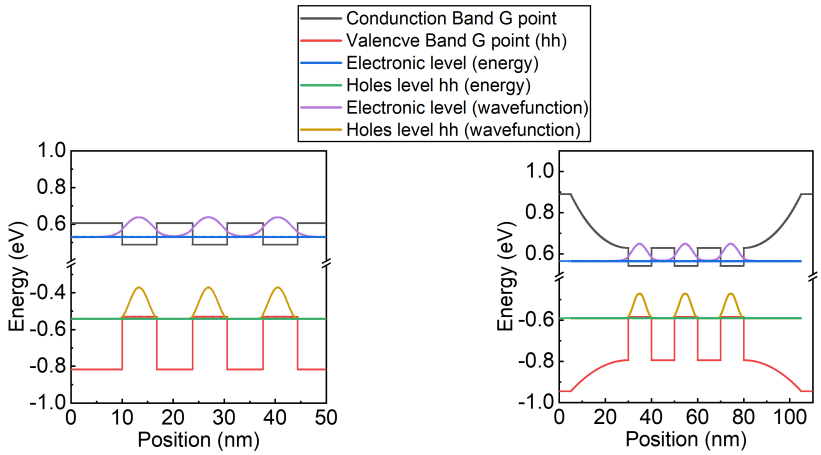

Figure 3.23: `nextnano3` simulations of two GaAsBi-based LD structures. Left: rectangular QW (RBi). Right: parabolically graded QW (PBi). The conduction band is shown in black, valence band in red, electron states in blue, heavy-hole states in green, electron wavefunctions in purple, and heavy-hole wavefunctions in ochre.

Figure 3.23 illustrates the simulated band structures. The RBi device comprises three 6.8 nm GaAsBi QWs separated by 7 nm GaAs barriers. The PBi structure contains three 10 nm GaAsBi QWs with 10 nm GaAs barriers, embedded in a parabolically graded AlGaAs potential where the Al concentration smoothly decreases from 30 % to 0 %. This design enhances carrier confinement and wavefunction localization.

The LDs were grown using the MBE system on Si-doped (100)-oriented n-GaAs substrates (350 µm, 2×10^{18} cm^{-3}). Substrate temperature was monitored in real time using a BandiT. Native oxide was desorbed at 650 °C for 10 minutes prior to growth. Standard procedures were employed for contact and cladding layers: highly

doped GaAs (n- and p-type), and $Al_{0.5}Ga_{0.5}As$ claddings doped to 5×10^{17} cm^{-3} , with growth rates between 650 and 1200 nm h^{-1}.
Due to the sensitivity of Bi incorporation, growth of GaAsBi QWs required additional steps: substrate cooling to 350–370 °C, stabilization of the As_2/Ga flux ratio, and Bi wetting layer deposition. RBi structures were grown at 350 °C, while PBi were grown at 370 °C. Bi pre-deposition was used to mitigate delayed incorporation effects [90]. Growth proceeded under Bi-rich conditions, with incorporation determined primarily by substrate temperature.
The RBi device also included a 1000 nm AlAs sacrificial layer for post-growth substrate removal and integration onto alternative platforms. Structural parameters are summarized in Table 3.6.

Table 3.6: Summary of GaAsBi-based laser diode structures.

Sample	QW Type	QW Thick. (nm)	Barrier Composition
RBi	Rectangular QWs	6.8	GaAs
PBi	QWs in PGB	10.0	GaAs + AlGaAs parab. (30 % → 0 %)

3.2.6. Processing and Characterization of GaAsBi-Based Laser Diodes

After MBE growth, the structures underwent standard cleaning: sequential acetone and isopropanol baths (80 °C, 10 min each), deionized water rinse, and drying on a 120 °C hotplate. AZ1518 photoresist was spin-coated at 4000 rpm for 30 s and baked at 100 °C for 60 s. The 4–5 µm wide device stripes were patterned by UV lithography at 75 mW/cm^2 and developed in a H_2O:AZ351B = 4:1 solution.
Mesas were etched using H_2O:H_2O_2:H_3PO_4 = 10:1:1 for 3 minutes, stopping in the Si-doped AlGaAs cladding. The resist was removed in acetone and isopropanol, followed by O_2 plasma cleaning.
For RBi devices, a modified process was applied due to the presence of the AlAs sacrificial layer, which prevented standard bottom contact deposition. An additional etch exposed the n-GaAs, enabling both contacts to be deposited from the top side. For PBi

devices, some substrates were mechanically and chemically thinned to 100 µm to enhance thermal dissipation.
Ohmic contacts were deposited by electron beam evaporation (VST TFDS-870). *p*-type: Ti (15 nm)/Au (180 nm); *n*-type: AuGe (140 nm)/Ni (25 nm)/Au (40 nm). Devices were cleaved into ∼500 µm bars forming Fabry–Pérot cavities.
The LDs were tested under pulsed operation (50 ns, 1 kHz) using an AVTECH AVRZ-5W-B generator. Output power was measured with a Thorlabs PM100D, and spectra with a 0.42 m VEB Carl Zeiss SPM-2 monochromator and TE-cooled InGaAs detector (IGA-030-TE2-H). *I*–*V* curves under CW were measured with a Keysight B2901 SMU.

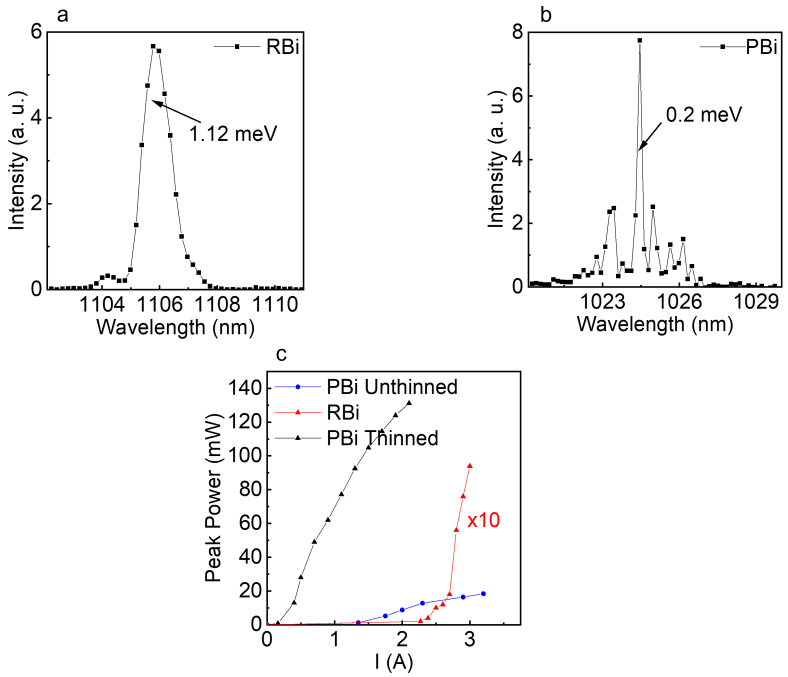

Figure 3.24: Lasing characterization of GaAsBi-based LDs. (a) RBi structure with Full Width at Half Maximum (FWHM) of the emission written. (b) PBi structurewith FWHM of the emission written. (c) Output power vs. injection current for RBi, PBi, and PBi with thinned substrate.

Lasing was achieved at 1106 nm for RBi and 1024 nm for PBi, Figures 3.24(a)–(b). The redshift of RBi is attributed to its higher Bi content (∼7 %) compared to PBi (∼5 %). The PBi device ex-

hibited superior performance, with a twofold higher peak output power (20 mW vs 10 mW at 3 A) and a significantly lower threshold current ($I_{\mathrm{th}} = 1.3$ A vs 2.5 A).
Further improvement was obtained for PBi after substrate thinning, where peak pulsed power exceeded 130 mW and threshold current decreased to 250 mA, Figure 3.24(c). The enhancement is attributed to improved thermal dissipation and reduced carrier losses by removing the defective GaAs substrate, which otherwise introduces trap states and leakage paths.
Low-frequency noise characterization of RBi devices revealed that GaAs antisite-related traps dominate, with activation energies of 0.31–0.33 eV across a wide injection range. Moreover, LT growth was found to promote the formation of Generation-Recombination (g-r) centers at QW–barrier interfaces. Variations in As_2/Ga BEPR between QWs and barriers further degrade interface quality by introducing transient growth phases during the initial monolayers, resulting in defect-related leakage paths. These effects are discussed in detail in [A2, A5, A6].
The main implication for VECSEL design is clear: low-temperature GaAs barriers inserted between GaAsBi QWs are defective and constitute a major limitation in LD performance. Nevertheless, the demonstration of lasing from GaAsBi QWs despite their intrinsically low IQE strongly supports the feasibility of GaAsBi-based VECSELs.

3.3. VECSEL

In the following, the step-by-step design and growth process of VECSEL chips is described. The focus is on four emission wavelengths: 976, 1030, 1060, and 1160 nm. For shorter emission wavelengths, InGaAs is used as the MQW compound, while for longer wavelengths GaAsBi is chosen. The main results presented were part of the ESA project IR Bi-based Sources (Irbis), Contract No. 4000122271/NL/SC, and have been verified by the project reviewer.

3.3.1. Distributed Bragg Reflector

The first step is the design and growth of the bottom DBR, on top of which the gain region and window layers are deposited.
The DBR is designed as a quarter-wavelength reflector, with layer thicknesses determined by the central wavelength of the photonic stopband, as expressed in Equation 1.4.

Design

For NIR DBRs, the standard material choice is GaAs as the high-index layer and AlAs as the low-index layer. Given their lattice constants of $a_{\mathrm{GaAs}} = 5.6532$ Å and $a_{\mathrm{AlAs}} = 5.6608$ Å, the mismatch is only 0.15 %. This small mismatch allows epitaxial growth without introducing stress-related defects, eliminating the need for strain-compensation layers [91].
Once the materials and their refractive indices are known, the maximum achievable stopband width for different central wavelengths can be calculated using Equation 3.19.

$$\frac{\Delta f_0}{f_0} = \frac{4}{\pi} \arcsin\left(\frac{n_2 - n_1}{n_2 + n_1}\right) \tag{3.19}$$

The next step is to calculate the refractive index of GaAs and AlAs at the target emission wavelengths. For GaAs, the Sellmeier equation provides a good approximation:

$$n(\lambda) = \sqrt{A + \frac{B}{1 - \frac{C^2}{\lambda^2}}} \tag{3.20}$$

where λ is the vacuum wavelength (in µm), and A, B, C are empirical coefficients. For GaAs, these are: $A = 8.950$, $B = 2.054$ and

$C^2 = 0.390$.
For greater accuracy, a higher-order expression is employed (Equation 3.21):

$$n^2(\lambda) = A + \sum_i \frac{B_i \lambda^2}{\lambda^2 - C_i^2} \tag{3.21}$$

For AlAs, the refractive index is calculated using the more complex expression in Equation 3.22, based on the Adachi model [92]:

$$n(\lambda) = \sqrt{A_0 \left[f(\chi) + \frac{f(\chi_{SO})}{2} \left(\frac{E_0}{E_0 + \Delta_{SO}} \right)^{\frac{3}{2}} \right] + B_0}$$

$$f(\chi) = \frac{2 - \sqrt{1+\chi} - \sqrt{1-\chi}}{\chi^2}, \quad \chi = \frac{hc}{\lambda E_0}, \quad \chi_{SO} = \frac{hc}{\lambda(E_0 + \Delta_{SO})} \tag{3.22}$$

Here, E_0 is the band gap at the Γ-point, and Δ_{SO} is the spin–orbit splitting energy.
Using the refractive indices of GaAs and AlAs, the physical thicknesses of the quarter-wave layers can be determined as:

$$d_{\mathrm{GaAs}} = \frac{\lambda}{4 n_{\mathrm{GaAs}}}, \quad d_{\mathrm{AlAs}} = \frac{\lambda}{4 n_{\mathrm{AlAs}}} \tag{3.23}$$

The results for the four target wavelengths are summarized in Table 3.7. The last design parameter to decide is the number of periods. The trade-off lies between stopband width and total thickness: thicker DBRs improve reflectivity but reduce thermal dissipation efficiency. Figure 3.25 shows the reflectance for different numbers of periods at 1060 nm. Beyond 30 periods, the stopband width increases only marginally. Therefore, 30 periods were selected as the baseline, balancing reflectivity with thermal management. Nevertheless, thinner DBRs with 20 periods may be explored in future designs.

Growth and Measurement

The growth of the DBRs was performed at high temperature to ensure the highest material quality. As substrates, full 2-inch Semi-Insulating (SI)-GaAs wafers were used. After growth, the wafer

Table 3.7: Refractive indices, quarter-wave thicknesses, and theoretical maximum bandwidths for GaAs/AlAs DBRs at different central wavelengths. Total thickness assumes 30 periods.

Parameter	976 nm	1030 nm	1060 nm	1160 nm
n_{GaAs}	3.5253	3.4926	3.4779	3.4413
n_{AlAs}	2.9680	2.9577	2.9526	2.9389
d_{GaAs} (nm)	69.21	73.73	76.20	84.27
d_{AlAs} (nm)	82.21	87.06	89.75	98.68
Total DBR thick. (nm)	4536.30	4841.70	4988.55	5490.00
Max bandwidth (nm)	106.79	108.88	110.37	116.42

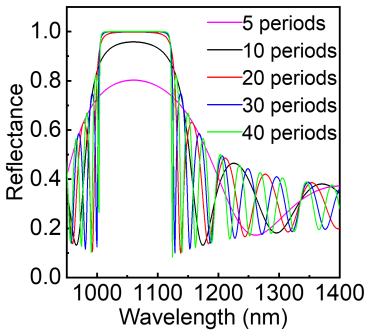

Figure 3.25: Calculated reflectance spectra of DBRs with central wavelength 1060 nm for different numbers of periods (5 to 40).

was cleaved into quarters: one quarter was taken out of the cleanroom for reflectance measurements, while the remaining three were retained as substrates for full VECSELs.
The total thickness of the DBRs ranges between 4.5 and 5.5 µm. As a result, depending on the exact growth rate, deposition times varied between 8 and 12 hours, requiring extremely stable fluxes. The sensitivity of the DBR central wavelength to growth rate precision is illustrated in Table 3.8. Assuming a 1.5 % error in layer thickness, the central wavelength shifts by up to 20 nm, highlighting the stringent accuracy required for growth calibration.
To improve growth accuracy, after determining the growth rates, a test DBR with 5 periods was grown and measured. The central wavelength of this calibration structure was compared with the cal-

Table 3.8: Effect of a 1.5 % increase in layer thickness on the central wavelength λ_0 of a GaAs/AlAs DBR.

Parameter	976 nm (nm)	1030 nm (nm)	1060 nm (nm)	1160 nm (nm)
d_{GaAs}	69.21	73.73	76.20	84.27
d_{AlAs}	82.21	87.06	89.75	98.68
$d_{\mathrm{GaAs}} + 1.5$ %	70.25	74.84	77.34	85.53
$d_{\mathrm{AlAs}} + 1.5$ %	83.44	88.37	91.10	100.16
λ_0 with $d_{\mathrm{GaAs}} + 1.5$ %	983.29	1037.74	1067.97	1168.72
λ_0 with $d_{\mathrm{AlAs}} + 1.5$ %	988.91	1043.50	1073.27	1174.16
λ_0 with both +1.5 %	995.25	1050.19	1079.57	1180.43

culated value, allowing adjustment of the deposition times of the subsequent layers if deviations were observed.
Another important consideration is the long-term stability of the DBRs. AlAs is prone to oxidation when exposed to air, forming an Al-oxide layer that degrades the optical properties of the mirror. To prevent this, the last layer of the DBR must always be GaAs. The thickness of this protective GaAs layer must be carefully included in the calculation of the first barrier of the gain region, since it effectively forms part of it.
Measured reflectance spectra of several DBRs with different central wavelengths are shown in Figure 3.26.

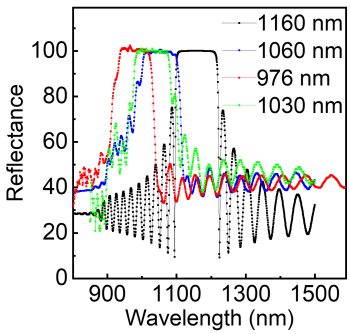

Figure 3.26: Measured reflectance spectra of four GaAs/AlAs DBRs with central wavelengths of 976, 1030, 1060, and 1160 nm.

3.3.2. Gain Region and Window Layer

The gain region is grown directly on top of the DBR and consists of 12 QWs. For the VECSELs emitting at 976 and 1030 nm, InGaAs QWs are used, while for 1060 and 1160 nm devices, GaAsBi serves as the active material.
The window layer is composed of AlAs, which both enhances light extraction and prevents carrier loss to the surface. However, due to the susceptibility of AlAs to oxidation, a GaAs cap is deposited on top to protect the structure.

Design of the Gain Region

Achieving lasing in VECSELs requires precise alignment of the quantum wells with the antinodes of the standing optical wave inside the cavity. Each QW must be positioned at an antinode to maximize overlap with the optical field. A schematic representation of this alignment is shown in Figure 3.27(a).
Because of the high reflectivity of the DBR, the first antinode is located at the DBR/spacer interface (see Figure 1.6). The second antinode must therefore coincide with the center of the first quantum well. This sets the condition for the spacer thickness, expressed in Equation 3.24:

$$\begin{aligned} d_{First}^{opt} &= \frac{\lambda}{2} - \frac{d_{QW}^{opt}}{2} = \lambda - \frac{d_{QW} \cdot n_{QW}}{2} \\ d_{First} &= \frac{d_{First}^{opt}}{n_{First}} = \frac{\lambda - d_{QW} \cdot n_{QW}}{2n_{First}} \end{aligned} \tag{3.24}$$

Between adjacent quantum wells, the field must undergo a half-wavelength shift, implying that the intermediate barrier thickness corresponds to an optical path of $\lambda/2$. This yields Equation 3.25:

$$\begin{aligned} d_{Inbetween}^{opt} &= \frac{\lambda}{2} - d_{QW}^{opt} = \frac{\lambda}{2} - d_{QW} \cdot n_{QW} \\ d_{Inbetween} &= \frac{d_{Inbetween}^{opt}}{n_{Inbetween}} = \frac{\lambda - 2d_{QW} \cdot n_{QW}}{2n_{Inbetween}} \end{aligned} \tag{3.25}$$

Finally, to maximize output coupling, the optical thickness of the last half well plus the final barrier must equal half a wavelength. This leads to Equation 3.26:

$$d_{Last}^{opt} = \frac{\lambda - d_{QW}^{opt}}{2} = \frac{\lambda - d_{QW} \cdot n_{QW}}{2}$$
$$d_{Last} = \frac{d_{Last}^{opt}}{n_{Last}} = \frac{\lambda - d_{QW} \cdot n_{QW}}{2n_{Last}} \tag{3.26}$$

To reduce the overall thickness of the gain region and improve thermal management, a modified design was introduced: pairs of quantum wells separated by a thin (7 nm) barrier, with thicker barriers between the pairs. In this geometry, the optical antinodes must align with the center of the thin barrier, leading to Equation 3.27, where d_b and n_b are the thickness and refractive index of the thin barrier:

$$d_{First} = d_{Last} = \frac{\lambda - d_b \cdot n_b - 2d_{QW} \cdot n_{QW}}{2n_{First}}$$
$$d_{Inbetween} = \frac{\lambda - 2d_b \cdot n_b - 4d_{QW} \cdot n_{QW}}{2n_{Inbetween}} \tag{3.27}$$

Since all barriers are GaAs, we take $n_{First} = n_{Inbetween} = n_{Last} = n_{GaAs}$. The final barrier values therefore depend only on the QW thickness and refractive index.
For InGaAs, the refractive index is evaluated using a Sellmeier-type model adapted for ternary alloys:

$$n(\lambda, x) = \sqrt{A + \frac{B\lambda^2}{\lambda^2 - C^2} + \frac{0.3223}{E_g(x)}} \tag{3.28}$$

where $E_g(x)$ is the composition-dependent band gap energy:

$$E_g(x) = E_g^{\mathrm{GaAs}} - 1.06x + 0.47x^2 \tag{3.29}$$

For GaAsBi, the refractive index can be estimated using the empirical relation from Bushell *et al.* [93]:

$$n = (3.87 \pm 0.03) - (0.31 \pm 0.02)\, E_g\,(\mathrm{eV}) \tag{3.30}$$

Figure 3.27 illustrates the two gain region designs, while Figure 3.28 compares refractive indices for GaAs, InGaAs, and GaAsBi.
The calculated thicknesses for the four gain regions are presented in Table 3.9. Note that multiple combinations of well thickness and

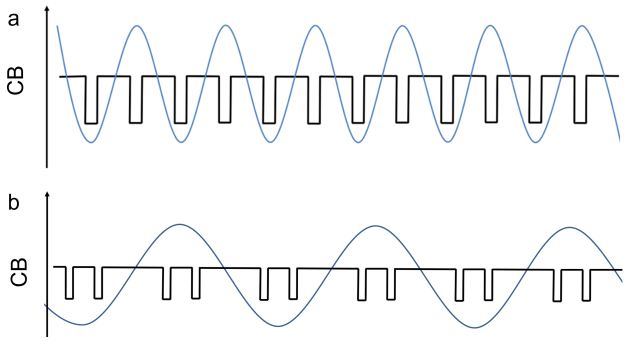

Figure 3.27: Sketch of the conduction band in two VECSEL gain region designs with the standing wave profile: (a) standard single QW design, (b) coupled QW pairs separated by thin barriers.

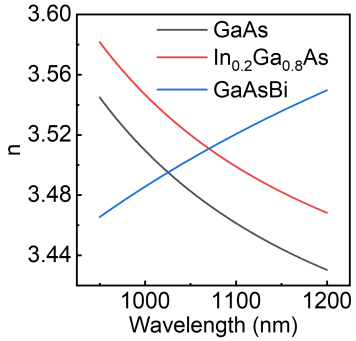

Figure 3.28: Calculated refractive indices of GaAs, InGaAs (20% In), and GaAsBi using Equations 3.20, 3.28, and 3.30.

alloy content can yield the same emission wavelength; the values listed correspond to structures that were actually grown. The last row illustrates the difference between the coupled-well and single-well designs.

Table 3.9: VECSEL gain region layer thicknesses for different emission wavelengths. The last row shows an example design with single quantum wells for comparison.

λ (nm)	Material	n_{QW}	d_{QW} (nm)	d_{thin} (nm)	d_{Between} (nm)	$d_{\mathrm{First/Last}}$ (nm)	d_{Total} (nm)
976	InGaAs	3.5626	5.7	7	123.34	130.88	988.86
1030	InGaAs	3.5339	7.6	12	119.58	133.52	1028.14
1060	GaAsBi	3.5074	5.5	7	134.30	143.34	1066.18
1160	GaAsBi	3.5387	5.5	7	150.23	159.39	1177.93
1160	GaAsBi	3.5387	5.5	–	162.89	165.72	2145.32

Design of the Window Layer

The design of the window layer is relatively straightforward. By construction, the last antinode of the optical field in the gain region coincides with the interface between the window and the final barrier. Since the next antinode must occur at the surface of the chip to maximize output coupling, the optical thickness of the window satisfies Equation 3.31:

$$\begin{aligned} d_{Window}^{opt} &= \frac{\lambda}{2} \\ d_{Window} &= \frac{d_{Window}^{opt}}{n_{Window}} = \frac{\lambda}{2n_{Window}} \end{aligned} \tag{3.31}$$

In our case, the window layer is AlAs, which requires protection against oxidation using a GaAs cap. Since the devices are barrier-pumped, the pump light is absorbed in GaAs. To minimize carrier loss in the cap, its thickness was reduced to 5 nm. Accounting for this layer modifies Equation 3.31, yielding Equation 3.32. Using this relation, the calculated AlAs window thicknesses for structures

capped with 5 nm GaAs are 158.5, 168.2, 173.6, and 191.5 nm for designs at 976, 1030, 1060, and 1160 nm, respectively.

$$d_{Window}^{opt} = \frac{\lambda}{2} - d_{Cap}^{opt}$$
$$d_{Window} = \frac{d_{Window}^{opt}}{n_{Window}} = \frac{\lambda - 2d_{Cap} \cdot n_{Cap}}{2n_{Window}} \tag{3.32}$$

Structures with this type of window and cap were fabricated. After more than a year, visible color changes were observed on the surface. Differential Interference Contrast (DIC) imaging revealed oxide-related surface features (Figure 3.29 (V4)), confirming that a 5 nm GaAs cap slows, but does not prevent, AlAs oxidation.
To determine the minimum GaAs thickness required for full protection, additional structures with 10 nm and 20 nm GaAs caps were grown and monitored. Their specifications are listed in Table 3.10. After two years, the 10 nm cap structure showed signs of oxidation, whereas the 20 nm cap maintained a pristine surface (Figures 3.29(V3) and (V4) respectively). Figure 3.29(V2) shows the DIC

Table 3.10: Window and cap layer specifications for VECSEL samples. Ages correspond to the images shown in Figure 3.29.

Sample	Window	Cap	Window Thick. (nm)	Cap Thick. (nm)	Age (years)
V1	AlAs	GaAs	140	20	2.5
V2	$Al_{30}Ga_{70}As$	GaAs	154	5	3
V3	AlAs	GaAs	162	10	2
V4	AlAs	GaAs	162	5	3

image of a sample with an $Al_{0.3}Ga_{0.7}As$ window capped by 5 nm GaAs. This structure remained free of oxidation after three years, suggesting that replacing pure AlAs with AlGaAs in the window can significantly improve long-term stability. Future studies will focus on determining the maximum Al content in AlGaAs windows that prevents oxidation-related degradation, as well as comparing the device performance of the different strategies. In the following, we focus on structures with AlAs windows capped by 20 nm GaAs.

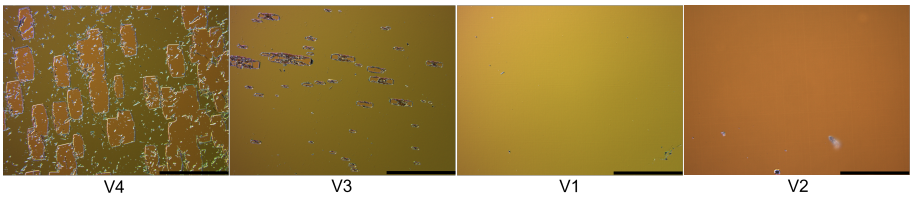

Figure 3.29: DIC images of the samples listed in Table 3.10, ordered from left to right: AlAs window with 5 nm GaAs cap (V4), 10 nm GaAs cap (V3), 20 nm GaAs cap (V1), and $Al_{0.3}Ga_{0.7}As$ window with 5 nm GaAs cap (V2). Sample ages range from 2.5 to 3 years.

For these, the calculated window thicknesses are 140.7, 150.5, 155.9, and 173.9 nm for 976, 1030, 1060, and 1160 nm, respectively.

MQW Growth

Before growing the full VECSEL devices, separate MQW regions were fabricated and characterized. For both InGaAs- and GaAsBi-based systems, preliminary samples consisted of 12 QWs separated by 7 nm GaAs barriers. This simplified design enabled faster growth than full structures with the thicker final barriers.

InGaAs MQW structures were grown at a thermocouple temperature of 580 °C, corresponding to approximately 510 °C as measured by BandiT. Growth rates of GaAs and InGaAs were calibrated at this temperature, enabling precise determination of the In content in the wells. The QW thickness was chosen to yield the target emission wavelength, which was verified by RTPL measurements after growth.

Once the optimal In content and well thickness were established, the appropriate barrier thicknesses for the final VECSEL devices were calculated using Equations 3.24, 3.25, and 3.26, or the modified model of Equation 3.27, depending on the selected design. These structures were then grown and characterized by RTPL spectra and mapping to provide reference data for subsequent devices.

For GaAsBi-based gain regions, the 12 QWs were grown at LT, adjusted according to the target emission wavelength. The final barrier was deposited at HT ∼570 °C (BandiT) to replicate the final device conditions and to account for the annealing-induced blueshift. A Bi wetting layer was deposited before the first QW to

improve layer quality. In thin-barrier designs, no additional Bi was required between wells, while in coupled-well designs with thicker barriers, a Bi wetting layer was redeposited before each pair to maintain uniformity.
All preliminary structures were characterized by RTPL spectra and spatial mapping. Based on these results, the final barrier thicknesses were determined, and complete VECSEL gain regions were grown and evaluated.

3.3.3. Full Device

Once the growth of all individual components has been optimized, the full VECSEL structure can be fabricated. Optimizing and characterizing each part separately is essential due to the considerable duration required for the complete device growth. Depending on the specific design and target emission wavelength, the growth of the full structure can take up to 20 hours, not including the additional time needed for source calibration and preparation.

Growth

The first step in VECSEL fabrication is the growth of the DBR, as described in Subsection 3.3.1. This process is carried out on a full 2-inch semi-insulating, double-side polished, EPI-ready SI-GaAs (100) substrate. Prior to initiating growth, the substrate undergoes thermal annealing to remove surface oxides, followed by the deposition of a 500 nm GaAs buffer layer to ensure high surface quality.
After DBR growth, the wafer is removed from the MBE system and divided into quarters. One quarter is typically reserved for optical characterization, while the remaining quarters can be reused as substrates for full VECSEL growth.
Upon reinsertion into the MBE system, these DBR quarters are annealed to eliminate any surface contamination and to desorb the oxide layer formed during air exposure. In this step, no additional buffer layer is deposited before proceeding with the growth of the gain region and window layer. Since the DBR is capped with a GaAs layer during its initial growth to prevent oxidation, the thickness of this cap must be taken into account and subtracted from the first barrier thickness to maintain correct optical spacing.

For both InGaAs- and GaAsBi-based VECSELs, the first barrier layer is grown at elevated temperature, approximately 600 °C as measured by BandiT, to optimize material quality. The substrate temperature is then lowered to the appropriate value for QW growth.
Following the MQW growth process described in the previous subsection, the growth sequence diverges depending on the material system. For InGaAs-based VECSELs, the substrate temperature is held constant, and the window and cap layers are grown immediately. In contrast, for GaAsBi-based structures, the substrate temperature is increased to match the calibration conditions, typically around 570 °C, before growing the window and cap layers. Once complete, the VECSEL quarters are extracted from the MBE system and characterized.

Characterization

All the grown VECSEL structures were characterized after growth using RTPL and reflectance measurements. The comparison between RTPL spectra and reflectance spectra is presented in Figure 3.30, in particular the difference between the reflectance spectra of the DBR and the VECSEL one is due to the absorption of the gain region.
In Figure 3.30(a) and (b) the spectra relative to two InGaAs-based VECSEL (emission at 975 and 1030 nm) are shown. While (c) and (d) show the spectra relative to two GaAsBi-based VECSELs (emission at 1060 and 1160 nm). The spectra, in eV, are then fitted using the Gaussian function, the results of the four fits are reported in Table 3.11, the center of the emission is obtained in eV and converted in nm for convenience.
The obtained emission matches well the center of the photonic stop-band of the DBR for all of the structures and is close to the target emission for the four designs. Furthermore the FWHM of the four samples is comparable, with values typical for InGaAs MQWs, while being much narrower than what is usually obtained from GaAsBi MQWs, where the typical value is around 100 meV.

AFM and DIC maps were measured to verify the surface quality of the structure. DIC maps are shown in Figure 3.29, while an example of an AFM map is shown in Figure 3.31, with measured

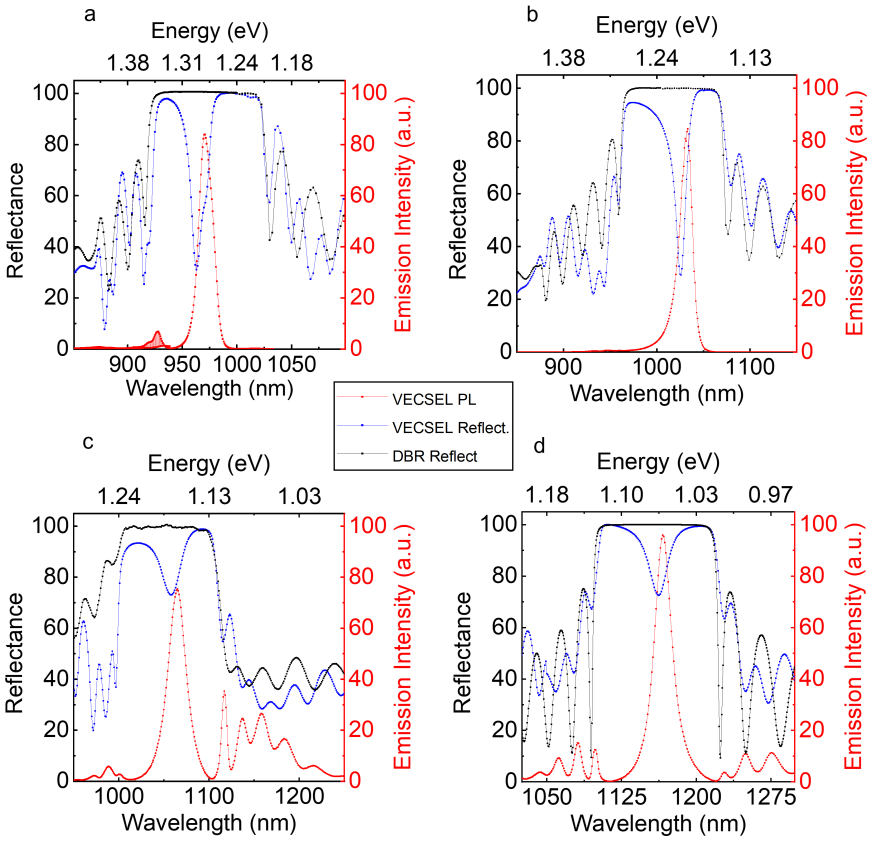

Figure 3.30: RTPL spectra (red curve) and reflectance (blue curve) of four full VECSEL compared with the reflectance spectra of respective DBR (in black). (a) InGaAs-based VECSEL emitting at 975 nm. (b) InGaAs-based VECSEL emitting at 1030 nm. (c) GaAsBi-based VECSEL emitting at 1060 nm. (d) GaAsBi-based VECSEL emitting at 1160 nm.

Table 3.11: Results of Gaussian fit on the RTPL spectra of the four VECSELs presented in Figure 3.30.

Sample	Center (eV)	Center (nm)	FWHM (meV)
VECSEL975	1.27607	971.24	19.82
VECSEL1030	1.20247	1031.08	19.66
VECSEL1060	1.16451	1064.12	22.50
VECSEL1160	1.06242	1166.37	21.14

roughness RMS(S_q) = 1.05 nm and (S_a) = 0.77 nm.

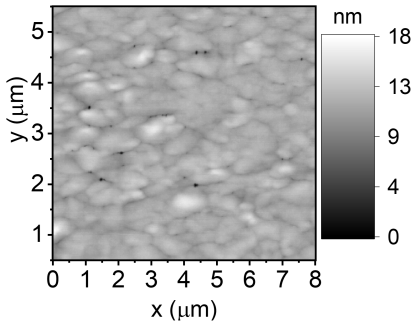

Figure 3.31: AFM map of an InGaAs-based VECSEL structure, measured roughness RMS(S_q) = 1.05 nm and (S_a) = 0.77 nm.

Furthermore, TDPL spectra were measured in the temperature range of 40–140 °C for both InGaAs- and GaAsBi-based VECSELs to investigate the temperature dependence of the emission energy and to verify the expected superior thermal stability of GaAsBi-based devices. Two representative series of spectra are shown in Figure 3.32.
It should be noted that the absolute intensity of the curves is not directly comparable. At higher temperatures, the emission intensity decreased significantly, particularly for the InGaAs-based VECSEL. To compensate for this, acquisition times were progressively increased with temperature. Additionally, for clarity and ease of comparison, the spectra have been scaled using a multiplication coefficient to offset the intensity differences.
The first notable observation is that, at elevated temperatures, a low-energy emission peak emerges in the InGaAs-based VECSEL.

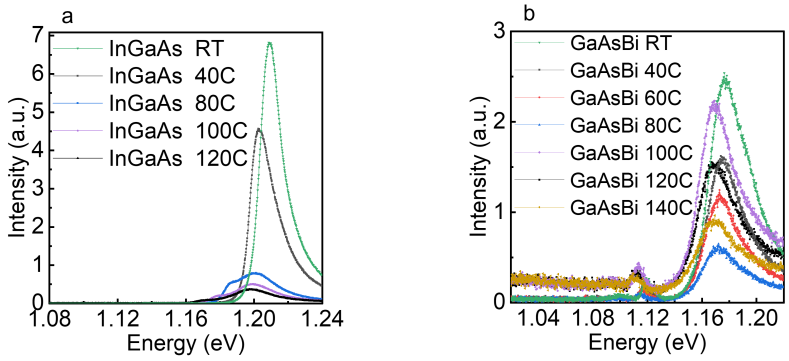

Figure 3.32: TDPL spectra of two VECSELs measured in the range 40–140 °C. (a) InGaAs-based VECSEL optimized for emission at 1030 nm. (b) GaAsBi-based VECSEL designed for 1060 nm emission.

This effect arises from the misalignment between the emission energy and the DBR stop band as temperature increases. Specifically, the emission wavelength shifts more rapidly with temperature than the photonic stop band of the DBR, leading to incomplete spectral overlap at higher temperatures.
Based on these spectra, the emission energy can be plotted as a function of temperature, as shown in Figure 3.33. The resulting data points are then fitted using a linear function. It is important to emphasize that, in general, the temperature dependence of the emission energy is not strictly linear. A more accurate description is provided by the Varshni equation [82]:

$$E(T) = E_0 - \frac{\alpha T^2}{T + \beta}, \tag{3.33}$$

where E_0 is the bandgap at 0 K, and α, β are empirical material parameters.
To justify the linear approximation over the measured range, we expand Eq. (3.33) about a reference temperature T_0 using a first-order Taylor expansion:

$$E(T) \approx E(T_0) + \left.\frac{dE}{dT}\right|_{T=T_0} (T - T_0). \tag{3.34}$$

The derivative of Eq. (3.33) can be evaluated using the quotient

rule:

$$\begin{aligned}\frac{d}{dT}\left(\frac{\alpha T^2}{T+\beta}\right) &= \frac{(T+\beta)(2\alpha T)-\alpha T^2}{(T+\beta)^2} \\ &= \frac{2\alpha T(T+\beta)-\alpha T^2}{(T+\beta)^2} \\ &= \frac{\alpha T[2(T+\beta)-T]}{(T+\beta)^2} \\ &= \frac{\alpha T(T+2\beta)}{(T+\beta)^2}\end{aligned} \tag{3.35}$$

Thus,

$$\frac{dE}{dT} = -\frac{\alpha T(T+2\beta)}{(T+\beta)^2}. \tag{3.36}$$

Evaluating this derivative at $T = T_0$ gives:

$$\left.\frac{dE}{dT}\right|_{T=T_0} = -\frac{\alpha T_0(T_0+2\beta)}{(T_0+\beta)^2}. \tag{3.37}$$

Substituting Eq. (3.37) into Eq. (3.34), we obtain the linearized form:

$$E(T) \approx E(T_0) - \left[\frac{\alpha T_0(T_0+2\beta)}{(T_0+\beta)^2}\right](T-T_0). \tag{3.38}$$

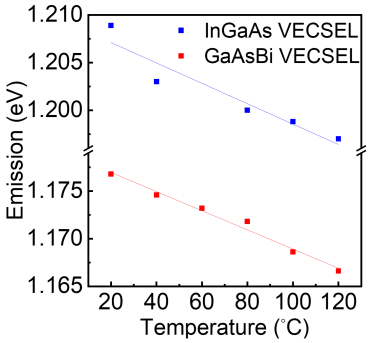

Figure 3.33: Emission energies extracted from Figure 3.32 as a function of temperature, fitted with a linear dependence.

Lasing Testing

Lasing tests of the VECSEL structures were performed in collaboration with the Laser Research Center at Vilnius University. The chips were mounted onto copper plates using thermally conductive paste and placed on Peltier modules for temperature control. During operation, the measured substrate temperatures ranged from 16 to 22 °C. The limited efficiency of this cooling approach was one of the main motivations for developing thinner VECSEL structures. In standard devices, a diamond heat spreader is typically bonded to the top surface of the chip to enable efficient thermal extraction. In contrast, the use of a Peltier module in contact with the unthinned backside of the wafer results in significantly reduced thermal management.

Optical pumping was carried out with an 808 nm semiconductor LD, focused to a 300 µm spot incident perpendicularly on the chip surface. It should be noted that, in the literature, lasing is typically reported only for devices with pumped areas up to 50 µm in diameter, in order to minimize the impact of surface inhomogeneities and thermally induced effects on the emission quality [94–96].

An external cavity mirror with 99 % reflectivity at 1064 nm was used. The mirror exhibited an effective reflectivity range of 1020–1080 nm, which imposed an additional limitation: structures designed for emission at 976 nm and 1160 nm fall outside this range, making lasing in those devices difficult to achieve. Moreover, due to aging effects, the 1030 nm structure could not be tested in this round. Although new samples have since been fabricated, testing is pending the installation of a new cavity mirror capable of covering the full emission wavelength range.

Emission from the devices was collected through a wavelength splitter, separating the pump from the signal, and recorded with an Avantes AvaSpec-3648 spectrometer operating across 200–1100 nm. Lasing was successfully demonstrated in both InGaAs- and GaAsBi-based VECSELs. The onset of lasing was marked by a pronounced narrowing of the emission spectra. For the InGaAs-based device, lasing occurred at a central wavelength of 973 nm, accompanied by the emergence of a secondary mode at 1005 nm (Figure 3.34).

A more detailed investigation was performed on the GaAsBi-based VECSEL. Lasing was observed near 1070 nm (Figure 3.35). Gaus-

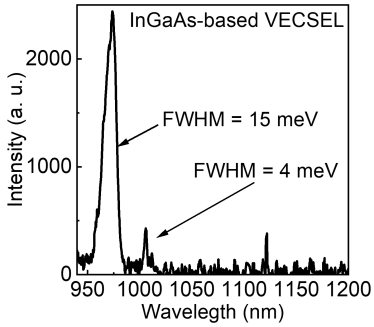

Figure 3.34: Lasing spectra of the InGaAs-based VECSEL designed for emission at 976 nm.

sian fitting of the emission peak at high pump powers yielded a FWHM of approximately 10 meV, substantially narrower than the broad PL linewidths typically measured in GaAsBi MQWs, which often exceed 100 meV. For this specific structure, the RTPL FWHM was 21 meV, confirming the strong spectral narrowing under lasing conditions.

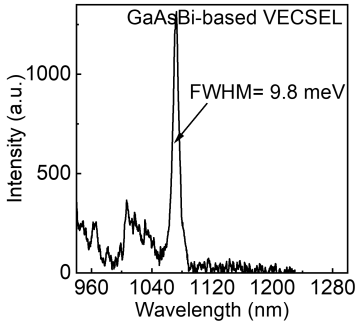

Figure 3.35: Lasing spectra of the GaAsBi-based VECSEL designed for emission at 1060 nm.

Power-dependent measurements were conducted on the same GaAsBi-based device, with pump powers ranging from 20 mW to 11.7 W (Figure 3.36). A lasing threshold of 280 ± 70 mW was identified. With increasing pump power, the emission peak redshifted slightly from 1070 nm to 1073 nm, an effect attributed to local heating in the active region. Importantly, the overall shift remained minimal, further demonstrating the excellent thermal stability of GaAsBi alloys.
Figure 3.37(a) shows the evolution of the emission wavelength and

FWHM with pump power, while Figure 3.37(b) displays the normalized integrated intensity. The sharp change in slope and narrowing of the spectrum confirm the transition to lasing.

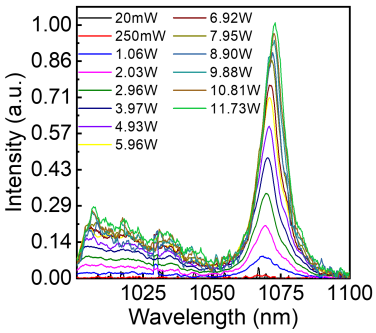

Figure 3.36: Lasing spectra of the GaAsBi-based VECSEL at different pump powers.

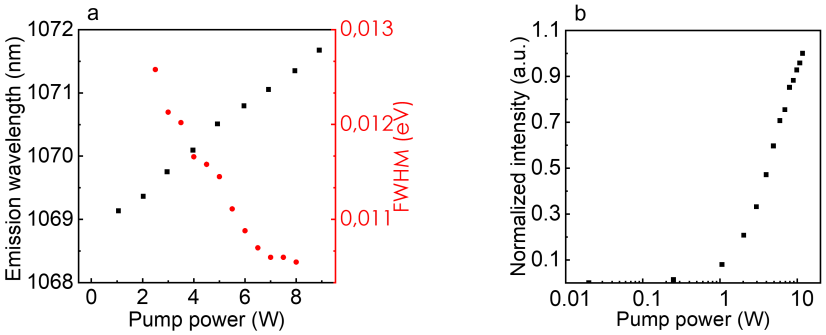

Figure 3.37: Data extracted from the spectra in Figure 3.36. (a) Emission wavelength and FWHM versus pump power. (b) Normalized integrated intensity versus pump power.

CONCLUSIONS

In the following, the main results of this work are summarized, with particular emphasis on those that have been submitted or accepted for publication in peer-reviewed journals. Most of these findings have been previously presented at numerous international conferences, either by the author or with the author as a co-author. A complete list of conference contributions, comprising over 50 participations, is provided at the beginning of this dissertation.

1. In the optimization of InGaAs-based MQWs, three critical aspects were investigated. First, the effect of post-growth annealing on InGaAs RTPL intensity was studied, revealing an optimal growth temperature of 510 °C. Higher temperatures improved AlAs and GaAs crystalline quality but induced In segregation, which strongly reduced emission intensity. Second, strain accumulation was modeled and found to cause MD formation in structures with more than three QWs separated by thin (7 nm) barriers. This model, however, failed when thick barriers (>100 nm) were introduced. As a result, for InGaAs-based VECSELs, only structures with quantum well pairs or single MQWs can be used to avoid dislocations. Third, the role of barrier composition was evaluated, identifying 12 % Al in AlGaAs as the optimal compromise between strong carrier confinement and high radiative efficiency for NIR emission at room temperature.

2. The optimization of technological parameters for GaAsBi-based MQWs growth established that GaAsBi layers with Bi contents up to 10 % can remain strain balanced even with a high number of wells. A precise growth window was identified, in which Bi incorporation is primarily controlled by substrate temperature (300–350 °C), Bi source temperature (500–530 °C), and an As/Ga BEPR in the range of 0.85–1.2. Furthermore, it was shown that high-temperature GaAs cap layers induce a ∼50 meV blue shift due to Bi segregation, while simultaneously enhancing PL intensity by reducing non-radiative recombination. Both effects must be accounted for

in the design of full devices.

3. To evaluate the IQE of GaAsBi structures, a modified ABC recombination model, which excludes Auger recombination and includes Trap-assisted Auger Recombination (TAAR) channels, was developed and validated. Application of this model to multiple GaAsBi samples consistently confirmed a high contribution of trap-assisted recombination, establishing the ABC model as a reliable tool for assessing internal efficiency in bismide structures.

4. For device-level optimization, GaAsBi-based LDs were fabricated with both rectangular and parabolically graded barrier geometries. Devices employing parabolic grading exhibited superior performance, including higher output power and reduced threshold currents, confirming the effectiveness of compositional grading in improving carrier confinement and reducing optical and electrical losses. Additionally, substrate thinning was shown to further enhance performance by lowering threshold currents and increasing output power.

5. Complete VECSELs were designed, grown, and characterized for four emission wavelengths. InGaAs-based devices targeted shorter wavelengths (976 nm and 1030 nm), while GaAsBi-based devices targeted longer wavelengths (1060 nm and 1160 nm). Characterization confirmed the validity of the design approach: RTPL and reflectance spectra exhibited the intended overlap between the emission and the center of the DBR photonic stopband. Temperature-dependent TDPL measurements (40–140 °C) demonstrated the superior thermal stability of GaAsBi-based devices compared to InGaAs. Finally, lasing was achieved in both material systems. The InGaAs-based VECSEL exhibited stimulated emission at 973 nm with spectral narrowing and the appearance of a longitudinal mode. The GaAsBi-based device lased at 1070 nm with a linewidth far narrower than typical PL, confirming strong optical gain. Power-dependent studies revealed only a small redshift of the lasing wavelength (1070–1073 nm), attributed to localized heating, further highlighting the thermal stability of GaAsBi-based VECSELs.

SANTRAUKA

3.4. Įvadas

Vertikalios išorinės ertmės paviršinės emisijos lazeris (VECSEL) yra optiškai kaupiniamas iš paviršiaus spinduliuojantis puslaidininkinis lazeris, kuris sulaukė didelio susidomėjimo dėl savo puikios pluošto kokybės, bangos ilgio derinimo galimybių ir galios keitimo. Skirtingai nei elektriškai kaupiniamas vertikalios ertmės paviršinės emisijos lazeris (VCSEL), kurio veikimą riboja būtinybė naudoti gaubiamuosius legiruotus Bragg'o veidrodžius (DBR) bei ribotas emisijos plotas, VECSEL vietoje viršutinio DBR naudoja išorinį veidrodį. Toks geometrijos sprendimas pašalina aktyviosios terpės žadinimą elektros srove, leidžia naudoti optinį kaupinimą ir suteikia galimybę įterpti išorinius optinius elementus į rezonatorių.
Medžiagų požiūriu, dažniausiai artimosios infraraudonosios spinduliuotės (NIR) srities VECSELs struktūrose aktyviajai terpei naudojami InGaAs/GaAs kvantiniai dariniai, t.y. daugybinės kvantinės duobės (MQW), išdėstytos stovinčios optinės bangos antinodėse. DBR dažniausiai sudaryti iš AlAs ir GaAs sluoksnių dėl jų didelio lūžio rodiklio kontrasto ir gardelės suderinamumo. InGaAs pagrindu pagaminti VECSELs sėkmingai veikia 920-1100 nm spektriniame intervale. Pavyzdžiui, 976 nm VECSELs naudojami antrajai harmonikai generuoti 488 nm bei kaip kaupinimo šaltiniai erbio stiprintuvams.
Vis dėlto, siekiant ilgesnių bangos ilgių, reikalingas didesnis indžio kiekis InGaAs QW, o tai didina gardelės neatitikimą su GaAs padėklu. Dėl to susidarantys įtempiai skatina dislokacijų formavimasi ir gesina spindulinę rekombinaciją bei generuoja lokalų struktūros kaitimą, kuris riboja įrenginio našumą, galią ir mažina veikos stabilumą. Nors yra taikomi įtempio kompensavimo metodai, pavyzdžiui, GaAsP/GaAsN sluoksnių įterpimas, vis tik jie apsunkina auginimo protokolą ir sumenkina struktūros kokybę.
Siekiant įveikti šiuos iššūkius, kaip alternatyva yra siūloma GaAsBi. Bismuto įterpimas į GaAs ženkliai sumažina draustinių juostų tarpą (apie 60-90 meV kiekvienam % Bi) ir leidžia pasiekti emisiją virš 1100 nm su mažesniais struktūros įtempiais nei InGaAs. Be to,

GaAsBi turi didelesnę spin–orbitino suskilimo energiją nei draustinių juostų tarpas, kai Bi kiekis viršija 10,5 %.Taip galima slopinti Ožė nuostolius. Taip pat GaAsBi pasižymi didesniu temperatūriniu stabilumu, todėl yra patrauklus NIR šaltinių veikiančių kambario temperatūroje be papildomo aušinimo kūrimui.
Vis dėlto GaAsBi QWs auginimas kelia daug iššūkių. Norint efektyviai įterpti Bi, būtina palaikyti žemą padėklo temperatūrą ir tiksliai valdyti As_2/Ga srautų santykį epitaksijos metu. Šios sąlygos dažnai inicijuoja defektų formavimąsi, cheminės kompozicijos netolygumą ir mažą emisijos intensyvumą. Todėl būtina optimizuoti augimo sąlygas.
Šiame darbe ypatingas dėmesys skiriamas GaAsBi MQWs optinei medžiagų kokybei, ypač vidinio kvantinio našumo (IQE) įvertinimui ir rekombinacijos mechanizmų analizei, įskaitant kruvininkų gaudyklių bei nespindulinės rekombinacijos mechanizmų interpretavimui.
Apibendrinant, VECSELs siūlo daugybę privalumų – lanksčią bangos ilgių kontrolę, didelę galią, aukštą pluošto kokybę ir galimybę integruoti optinius elementus – tačiau jų veikimas tiesiogiai priklauso nuo epitaksinių struktūrų kokybės. InGaAs pagrindu veikiančių įrenginių atveju pagrindinė problema yra įtempių valdymas, o GaAsBi atveju – defektų sukeltų nuostolių mažinimas. Šiame darbe nagrinėjami abu šie aspektai, siekiant tobulinti efektyvius ir termiškai stabilius VECSELs NIR spektriniam ruožui.

Tyrimo tikslas

Pagrindinis šio darbo tikslas – GaAsBi kvantinių darinių, skirtų naudoti artimosios infraraudonosios spinduliuotės VECSELs struktūrose, emituojančiose 1000–1200 nm spektriniame ruože, technologijos optimizavimas. Tam pasiekti buvo numatyti šie uždaviniai:

1. InGaAs daugybinių kvantinių duobių technologijos optimizavimas, skirtas nustatyti optimaliausią aktyviosios terpės dizainą. InGaAs MQWs panaudoti palyginimui su GaAsBi struktūromis.

2. GaAsBi MQWs technologinių parametrų optimizavimas, taikymams prietaisuose.

3. GaAsBi kvantinių darinių vidinio kvantinio našumo įvertinimas, siekiant išsiaiškinti rekombinacijos mechanizmus.

4. Lazerino diodo auginimas, siekiant įvertinti GaAsBi MQWs technologijos pritaikomumą VECSELs struktūroms.

5. VECSELs projektavimas ir epitaksija bei jų charakterizavimas.

Naujumas

1. Didėlės erdvinės skyros fotoliuminescencijos kambario temperatūroje (RTPL) žemėlapių skenavimas pademonstruotas kaip efektyvus metodas, skirtas gardelės nesutapimo inicijuotų dislokacijų tinklo aptikimui ir analizei MQW struktūrose.

2. Pasiūlytas naujas daugybinių kvantinių duobių porų su įterptais pakaitiniais barjerais dizainas, leidžiantis kurti kompaktiškesnius ir efektyvesnius VECSELs.

3. Pasiūlytas modifikuotas ABC modelis pritaikytas GaAsBi rekombinacijos kanalų tyrimui ir IQE skaičiavimams.

4. Išvystyta lazerinio diodo (LD) gamyba naudojant du skirtingus barjerų dizainus (stačiakampius ir parabolinius), siekiant palyginti prietaisų savybes.

5. Pirmą kartą pademonstruotas GaAsBi MQW VECSELs projektavimas, auginimas ir charakterizavimas.

Gynamieji teiginiai

1. Tiksli indžio kiekio ir kvantinės duobės storio kontrolė InGaAs-pagrindu struktūrose, epitaksiškai užaugintose ant GaAs, leidžianti pasiekti didelio ploto emisijos homogeniškumą, rodo jų perspektyvumą ateities fotoninių prietaisų masinei gamybai.

2. Vykdant molekulinių pluoštelių epitaksiją temperatūros apribotos kinetikos sąlygomis, galima užauginti GaAsBi daugybinių kvantinių duobių struktūras įvedant iki 10 % bismuto.

3. Novatoriškas dizainas, apimantis GaAsBi junginio daugybines kvantines duobes su paraboliniais AlGaAs barjerais ir šilumos nuvedimo strategiją, leidžia sumažinti lazerio slenkstinę įveikinimo srovę kambario temperatūroje mažiausiai 30 % ir padidinti stimuliuojamą emisiją daugiau nei 10 kartų.

4. Nauja VECSEL architektūra, kurioje naudojamos GaAsBi kvantinių duobių poros atskirtos plačiu GaAs barjeru, leidžia padidinti lazerio kaupinimo plotą, pagerina įveikinimo našumą ir supaprastina šilumos nuvedimą.

Autoriaus indėlis

Autorius reikšmingai prisidėjo prie analizuojamų struktūrų projektavimo, auginimo ir modeliavimo, taip pat buvo atsakingas už gautų duomenų analizę ir interpretavimą. Autorius taip pat dalyvavo visų straipsnių rengime ir aptarime bei aktyviai prisidėjo prie rezultatų sklaidos tarptautinėse konferencijose.

3.5. Disertacijos struktūra

Disertaciją sudaro įvadas ir trys dalys: literatūros apžvalga, metodai ir rezultatai, bei išvados. Literatūros apžvalga išsamiai pateikia pagrindinius GaAsBi ir InGaAs puslaidininkinių junginių ir kvantinių darinių pasiekimus, apžvelgia naujausius LD ir VECSEL gamybos bei parametrų pasiekimus, iššūkius ir problemas.
Šiame darbe struktūrų auginimui ir charakterizavimui buvo pasitelkti metodai: „Veeco GENxplor R&D“ Molekulinių pluoštelių epitaksija (MBE) su metaliniais Ga, Al, In, Bi, As, šaltiniais bei Si, Be legiravimui. Struktūros buvo charakterizuojamos naudojant:

- RTPL
- Fotoliuminescencijos temperatūrinę priklausomybę (TDPL)
- Mikrofotoliuminescenciją (µPL)
- Rentgeno spindulių difrakciją (XRD)
- Atominių jėgų mikroskopiją (AFM)

- Didelės skiriamosios gebos peršviečiamąją elektronų mikroskopiją (HR-TEM)
- Diferencinio interferencijos kontrasto (DIC) mikroskopiją

3.6. Pagrindiniai rezultatai

Toliau pateikiami pagrindiniai doktorantūros laikotarpiu gauti rezultatai, įskaitant:

- Atkaitinimo efektą InGaAs QWs.
- Gardelės neatitikimų susidarymą InGaAs MQWs, šios dalies rezultatai aprobuoti publikacijoje [A7].
- AlGaAs naudojimą kaip elektronų blokavimo sluoksnį InGaAs QWs, šie rezultatai aprobuoti publikacijoje [A4].
- Įtempių generacijos GaAsBi MQWs tyrimą, dalis šių rezultatų aprobuoti publikacijoje [A1].
- GaAsBi MQWs augimo parametrų optimizavimą.
- Atkaitinimo įtaką GaAsBi MQWs optinėms savybėms.
- GaAsBi IQE skaičiavimą, aprobuoti publikacijoje [A3].
- LDs augimą ir charakterizavimą, aprobuoti publikacijoje [A6].
- LDs charakterizavimo žemo dažnio triukšmo matavimais, aprobuoti publikacijose [A2] ir [A5].
- VECSEL projektavimą ir augimą
- VECSEL charakterizavimą, aprobuoti ESA projekto „Infraraudonųjų spindulių šaltiniai veikiantys bismidinių junginių pagrindu; Irbis“, sutarties Nr. 4000122271/NL/SC.

3.7. InGaAs optimizavimas

InGaAs vis dar išlieka artimosios infraraudonosios spinduliuotės šaltiniuose dažniausiai pritaikomas junginys bei našumo etalonas. Pirmiausia optimizavome InGaAs QWs auginimą. Pagrindiniai iššūkiai aptarti disertacijoje yra:

- In segregacija.
- gardelės neatitikimo dislokacijos.
- krūvininkų termalizacija.

3.7.1. Padėklo temperatūros poveikis

(Ga,In)(N,As) sistemose indžio segregacija, kaip žinoma, didėja kylant padėklo temperatūrai [52,58]. Arsenidų sistemose In segregaciją mažina kinetiniai apribojimai. [52] nurodo minimalią segregaciją esant 370 °C temperatūrai, tačiau dėka žemos temperatūros prastėja kristalinė darinio kokybė. Geriausias kompromisas tarp sudėties vienalytiškumo ir optinės kokybės pasiekiamas esant 520 °C, nes kai temperatūra viršija 570 °C prasideda intensyvi In desorbcija. Tai kelia iššūkį VECSEL struktūroms, kurios savyje turi GaAs ir AlAs sluoksnius, reikalaujančius žymiai aukštesnės augimo temperatūros – iki 720 °C AlAs atveju [76–80].
Norėdami įvertinti barjero auginimo temperatūros poveikį, auginome keturis bandinius su InGaAs QWs ir skirtingomis barjero sudėtimis (tuo pačiu ir temperatūromis). Fotoliuminescencijos (PL) spektruose buvo stebėtas mėlynasis poslinkis ir intensyvumo sumažėjimas, didėjant barjero temperatūrai, auginant tiek GaAs, tiek ir AlGaAs barjerus. Rezultatas buvo paaiškintas In segregacija ir kristalinės kokybės degradacija.

3.7.2. Dislokacijų tankio mažinimas

InGaAs/GaAs MQWs dislokacijos veikia kaip nespindulinės rekombinacijos centrai, sumažindamos PL ir didindamos lokalų įkaitimą. Šiame skyriuje nagrinėjamas deformacijų valdymas šešiose MQWs struktūrose, pritaikant teorinius deformacijų modelius eksperimentiniams duomenims paaiškinti.

Įtempių skaičiavimas

Vidutinė ir perteklinė deformacija MQW sistemose apskaičiuojama taip:

$$\langle f\rangle = f\cdot\frac{Nt_w}{Nt_w+(N-1)t_b}, \langle f_{\mathrm{eq}}\rangle = f\cdot\frac{T_{\mathrm{eq}}}{T_{\mathrm{MQW}}}, \langle f_{\mathrm{ex}}\rangle = \langle f\rangle - \langle f_{\mathrm{eq}}\rangle, \tag{3.39}$$

kur N yra kvantinių duobių skaičius, t_w ir t_b yra duobių ir barjerų storiai. Sluoksnio storiui ir In kiekiui nustatyti buvo naudojamas XRDs metodas. Bx0240 bandinyje naudojami 6 QW porų atskirtų pakaitomis 7,3 nm ir 119 nm barjerais, todėl vidutinis barjero storis yra 67,2 nm. 3.12 lentelėje apibendrinti deformacijos rezultatai, įskaitant dviejų QW konfigūraciją.

3.12 lentelė: Deformacijos ir kritinio storio analizė: t_w - kvatinės duobės storis, t_b - barjero storis, N - kvantinių duobių skaičius, $\langle f\rangle$ - vidutinis įtempis, T_{eq} - kritinis storis, f_{eq} - kritinis įtempis, $\langle f_{\mathrm{ex}}\rangle$ - perteklinis įtempis.

Bandinys	In (%)	t_w (nm)	t_b (nm)	N	$\langle f\rangle$ (%)	T_{eq} (nm)	f_{eq} (%)	$\langle f_{\mathrm{ex}}\rangle$ (%)
Ax0183	18,3	6,6	7,0	12	0,667	17,610	0,148	0,518
Ax0225	22,5	4,6	7,1	12	0,669	13,610	0,165	0,504
Ax0232	23,2	5,0	7,1	12	0,724	13,100	0,158	0,566
Ax0256	25,6	5,0	7,0	12	0,805	11,570	0,155	0,650
Ax0241	24,1	4,2	7,3	12	0,667	12,490	0,165	0,502
Bx0240	24,0	4,1	67,2	12	0,106	12,550	0,027	0,079
Cx0240	24,0	7,0	38,75	9	0,291	12,550	0,058	0,233

Tyrimo rezultatai parodė, kad stori tarpiniai barjerai Bx0240 žymiai sumažina vidutinę ir perteklinę deformaciją. Modelio prognozės nusako, kad tik struktūros, turinčios 1–3 QW, lieka žemiau kritinės įtempio ribos.

µPL žemėlapių sudarymas

µPL žemėlapių skenavimas patvirtino RTPL rezultatus ir atskleidė submikrometrinės skalės emisijos ypatybes (3.39 pav.). Emisijos

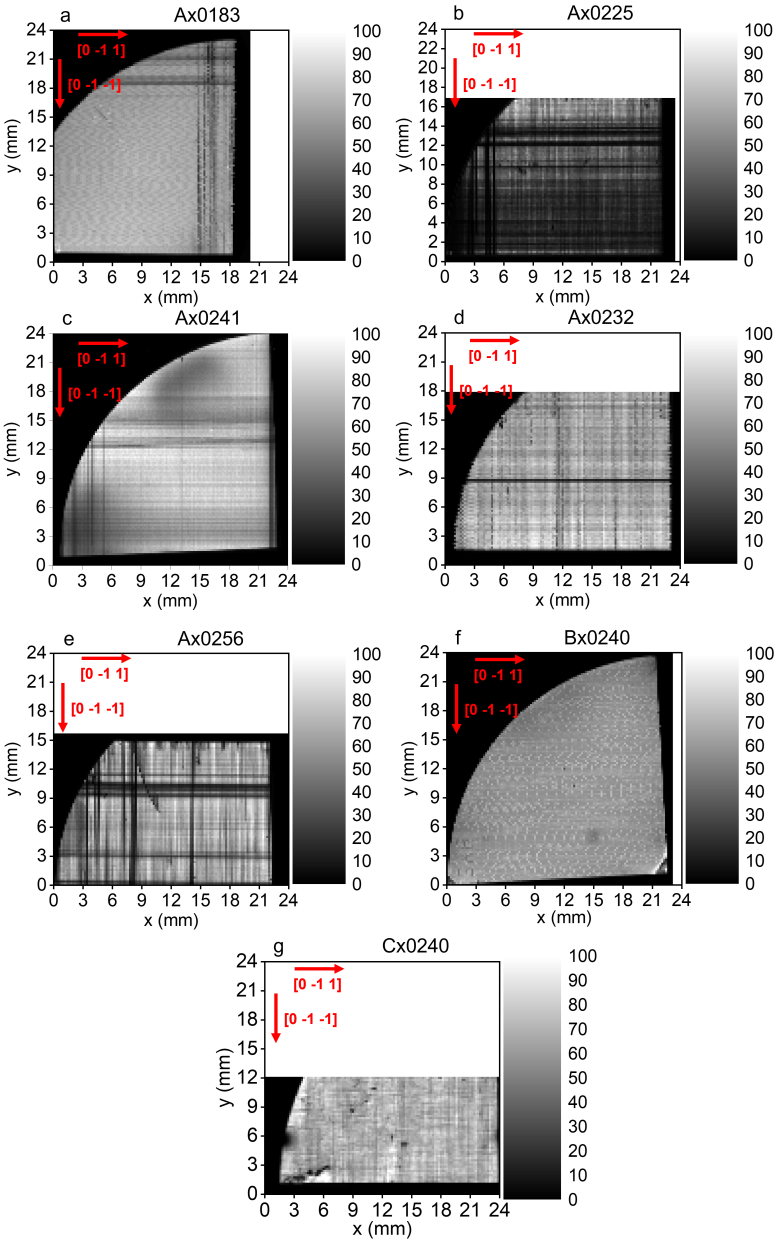

3.38 paveikslas: Septynių tirtų bandinių RTPL žemėlapiai: (a)–(e) bandiniuose naudojami ploni barjerai, po to – dvigubi ir trigubi barjerai. Rodyklės nurodo kristalografines kryptis.

slopinimo linijos, sulygiuotos su [0-11] ir [0-1-1] kryptimis, rodo gardelių neatitikimo dislokacijų (MD) tinklo buvimą. Bx0240 bandinys pasižymėjo mažesniu dislokacijų tankiu.

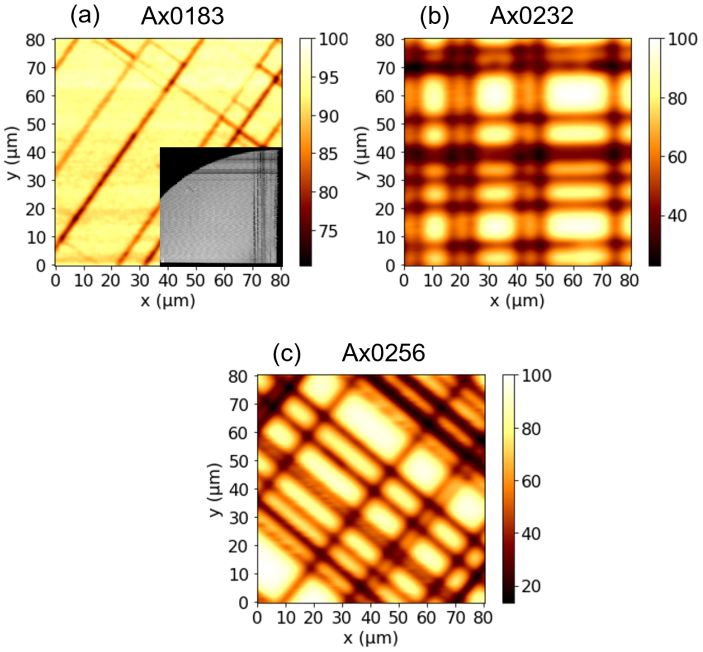

3.39 paveikslas: Ax0183, Ax0232 ir Ax0256 bandinių µPL žemėlapiai nuskenuoti iš 80×80 µm^2. Linijos išlygiuotos [0 -1 -1] ir [0 -1 1] kryptimis. Įklijoje pateiktas RTPL žemėlapis, nuskenuotas iš stačiakampiu pažymėto ploto bandinyje Ax0183.

Dislokacijų tinklo egzistavimui patvirtinti buvo atliekami AFM tyrimai. Abeji matavimai patvirtina modelio prognozę, kuri teigia, kad struktūros su 3 ir daugiau QWs atskirtų plonais barjerais viršija kritinę deformaciją. Struktūros, kuriose suprojektuotos duobių poros, atskirtos storais barjerais, elgiasi kaip izoliuotos duobės, efektyviai išeliminuodamos relaksaciją ir MDs susidarymą.
Taigi, optimali InGaAs QWs pagrindu VECSELs struktūra subalansuoja banginių funkcijų persidengimą ir deformacijų valdymą, sujungiant QWs poromis. Tripletai sukelia MDs ir netolygią emisiją, o tai mažina prietaiso našumą.

3.7.3. Al kiekis barjeruose

Siekdami pagerinti krūvininkų sąspraudą ir spinduliavimo efektyvumą, tyrėme Al įterpimą į barjerus. Modeliavimas ir eksperimentai parodė, kad didėjant Al kiekiui, kristalų kokybė pagerėja. Buvo įvertinta optimali Al vertė - 12 %, kuri užtikrina pakankamą kvantinę sąspraudą, išsaugant optinį našumą kambario temperatūroje. Viršijus šį Al kiekį, kristalų kokybė smarkia blogėja.

3.8. GaAsBi augimo optimizavimas

Antras disertacijoje tiriamas junginys yra GaAsBi. Pagrindiniai jo privalumai yra ženklus draustinių energijų juostos mažėjimas (artimojoje infraraudonojoje spektro srityje link ilgų bangų įvedant į GaAs nedidelį Bi kiekį), didelis spin-orbitinis suskilimas (kuris smarkiai slopina Ožė nuostolius) ir geresnis temperatūrinis stabilumas, palyginti su klasikiniais III–V puslaidininkiais.
Skirtingai nuo InGaAs, GaAsBi dar nebuvo panaudotas VECSEL struktūrų aktyviojoje terpėje. Todėl labai svarbu optimizuoti jo auginimą ir kvantinio darinio dizainą.
Šiame skyriuje daugiausia dėmesio skiriama:

- įtempių ir dislokacijų susidarymui
- auginimo temperatūros poveikiui
- atkaitinimo poveikiui emisijos intensyvumui ir energijai
- vidiniam kvantiniam našumui

3.8.1. GaAsBi įtempiai ir dislokacijos

Dėl eksperimentinių duomenų apie GaBi trūkumo, GaAsBi sluoksnių gardelės neatitikimas ir kritinis storis nėra gerai žinomi. Nuoroda [2] įvertina kritinį storį iki 3,1 % Bi, tačiau emisijai, viršijančiai 1 µm, reikalingas didesnis Bi kiekis. Įtempiams ir relaksacijai įvertinti ant itin plonų buferių buvo užauginti 100 nm storio GaAsBi sluoksniai, kuriuose Bi kiekis siekia iki 11,2 %. XRD svyravimo kreivės ir atvirkštinės gardelės žemėlapiai rodo, kad visi sluoksniai išlieka beveik visiškai įtempti, ir reikšmingos relaksacijos neaptikta. Šie rezultatai, paskelbti [A1], rodo, kad GaAsBi sluoksniai su Bi iki

11,2 %, išlieka pseudomorfiniai. RTPL žemėlapių skenavimas buvo panaudotas dislokacijų tyrimui GaAsBi MQW. Buvo išaugintos struktūros, turinčios 5 ir 12 QW su plonais (7 nm) GaAs barjerais. Kaip matome 3 paveiksle emisijos intensyvumo pokyčio, priešingai nei InGaAs MQW, nėra. Tai rodo, kad GaAsBi sluoksniai, net kai Bi kiekis artėja prie 10 %, turi didesnį kritinį storį nei $In_{0,2}Ga_{0,8}As$.

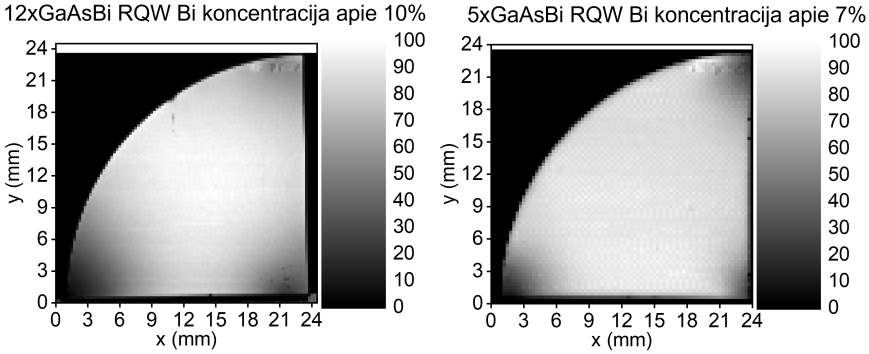

3.40 paveikslas: RTPL MQWs GaAsBi žemėlapiai: (a) 12 QWs, pasižyminčių emisija ties 1,084 eV ir (b) 5 QWs, pasižyminčių emisija ties 1,128 eV.

3.8.2. Augimo parametrų optimizavimas

Bi įterpimą daugiausia lemia As_2/Ga santykis ir padėklo temperatūra. Auginome struktūras su trimis GaAsBi/GaAs QW (5,5 nm duobėmis ir 7 nm barjerais), keitėme As_2/Ga ir Bi šaltinio temperatūrą, išlaikydami pastovų Ga srautą. Pastebėta, kad optimizuotuose diapazonuose Bi įterpimo neriboja As_2/Ga ar Bi srautas, daugiausia įtakos daro padėklo temperatūra.

Atkaitinimo efektai

Bandiniai su 3 GaAsBi QW, užauginti 350 °C temperatūroje, buvo padengiami GaAs sluoksniu. Tyrimas buvo atliekamas keičiant dengiamojo sluoksnio auginimo temperatūrą, tuo pačiu imituojant pilno prietaiso auginimo protokolą: 350 °C aktyviajai sričiai ir 570 °C dengiamiesiams sluoksniams. RTPL rezultatai pateikti 3.41 paveiksle. Stebimi du pagrindiniai efektai:

- 50 meV mėlynasis poslinkis struktūrose su aukštoje temperatūroje užaugintu GaAs dengiamuoju sluoksniu priskiriamas

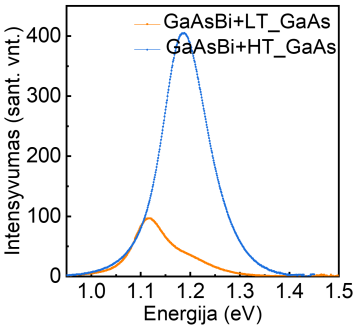

3.41 paveikslas: Liuminescencijos spektrai matuoti GaAsBi MQW su GaAs dengiamuoju sluoksniu, užaugintu esant skirtingoms temperatūroms.

Bi segregacijai ir dėl jos sumažėjusiam Bi kiekiui viršutiniuose QW sluoksniuose.

- daugiau nei dvigubai padidėjęs PL intensyvumas atkaitinant (auginant GaAs dengiamąjį sluoksnį aukštoje temperatūroje) rodo defektų sumažėjimą ir pagerėjusį kristališkumą.

Dar aukštesnėse temperatūrose buvo stebimas Bi kvantinių taškų (QDs) susidarymas [84], kuris nepatenka į šio darbo taikymo sritį. Todėl vėlesni augimai siekiant subalansuoti struktūros kokybę ir Bi kiekį apsiribojo 570–580 °C temperatūrų sritimi.

3.8.3. Vidinis kvantinis efektyvumas

GaAsBi/GaAs MQWs IQE buvo įvertintas naudojant du 12-QW bandinius. Pirmajame bandinyje buvo pakaitomis naudojami 7 nm ir 150 nm GaAs barjerai, suderinti su optinio lauko antinodėmis, auginami 425 °C temperatūroje. Antrajame bandinyje buvo naudojami visi vienodi 7 nm barjerai, auginami 435 °C temperatūroje. Abu bandiniai buvo padengti GaAs sluoksniu užaugintu aukštoje temperatūroje.
Buvo pasiūlytas modifikuotas ABC modelis, siekiant paaiškinti šių struktūrų labai nedidelį IQE. Nors tęsiamas IQE skaičiavimo optimizavimas, šie pradiniai rezultatai patvirtina GaAsBi potencialą kaip aktyviosios terpės VECSEL struktūrose.

3.9. LD augimas

Buvo sukurtos ir ištirtos dvi aktyviųjų sričių geometrijos: standartinės stačiakampės GaAsBi kvantinės duobės (RBi) ir duobės apgaubtos paraboliškai graduotais barjerais (PBi) [A2]. Abiejų struktūrų modeliavimas, pagrįstas 8×8 $\mathbf{k}\cdot\mathbf{p}$ metodu, atliktas naudojant `nextnano`[3]. Modeliavimas apėmė eksitoninius ir nuo temperatūros priklausomus efektus. Deformacija buvo neįskaičiuojama dėl pseudomorfinio sluoksnio esant mažoms Bi koncentracijoms. Medžiagos parametrai buvo paimti iš literatūros [72–75]. Lazeriavimo spektrai buvo registruojami žadinant impulsais (50 ns impulsai esant 1 kHz dažniui). Emisijos spektrai ir galios priklausomybė nuo srovės parodyti 3.42 paveiksle. RBi diodas pasižymėjo emisija ties 1106 nm, o PBi – ties 1024 nm, kas atitinka didesnį Bi kiekį RBi kvantinėse duobėse (apytiksliai 7 % RBi ir 5 % PBi).
Pastebėta, kad PBi dizainas žymiai pagerino našumą: maksimali galia padvigubėjo (nuo 10mW iki 20 mW esant 3 A), o slenkstinė srovė sumažėjo nuo 2,5 A iki 1,3 A. Tolesnis pagerėjimas buvo pasiektas ploninant padėklą (juoda kreivė 3.42c paveiksle), kas padidino išėjimo galią iki 130 mW ir sumažino slenkstinę srovę iki 250 mA. Tai sąlygojo dų veiksniai: (i) geresnis šilumos nuvedimas ir aukštesnė epitaksinių sluoksnių kristalinė kokybė, (ii) pašalinus dalį padėklo, sumažėjo krūvininkų nuostoliai ir padidėjo šiluminis bei elektrinis našumas. Žemo dažnio triukšmo matavimai RBi LD atskleidė GaAs pakaitinių defektų sukeltus pagavimo lygmenis, kurių aktyvacijos energija kito nuo 0,31 eV iki 0,33 eV. Be to, buvo stebėta, kaip žemos temperatūros augimas paskatino generacijos–rekombinacijos (g-r) centrų formavimąsi, kurie veikia kaip nuotėkio veiksniai ir mažina krūvininkų patekimo į QW efektyvumą. Šie rezultatai išsamiai aprašyti [A2, A5, A6]. Nepaisant mažo IQE buvo pasiektas lazeriavimo efektas patvirtinantis GaAsBi pagrindu VECSEL struktūrų galimybės įgyvendinimą.

3.10. VECSEL

Šiame skyriuje išsamiai aprašomas VECSEL lustų, skirtų spinduliuotei 976, 1030, 1060 ir 1160 nm bangos ilgiuose, projektavimas ir auginimas. Trumpesniems bangos ilgiams buvo naudojamas InGaAs, o ilgesniems – GaAsBi. Rezultatai gauti vykdant

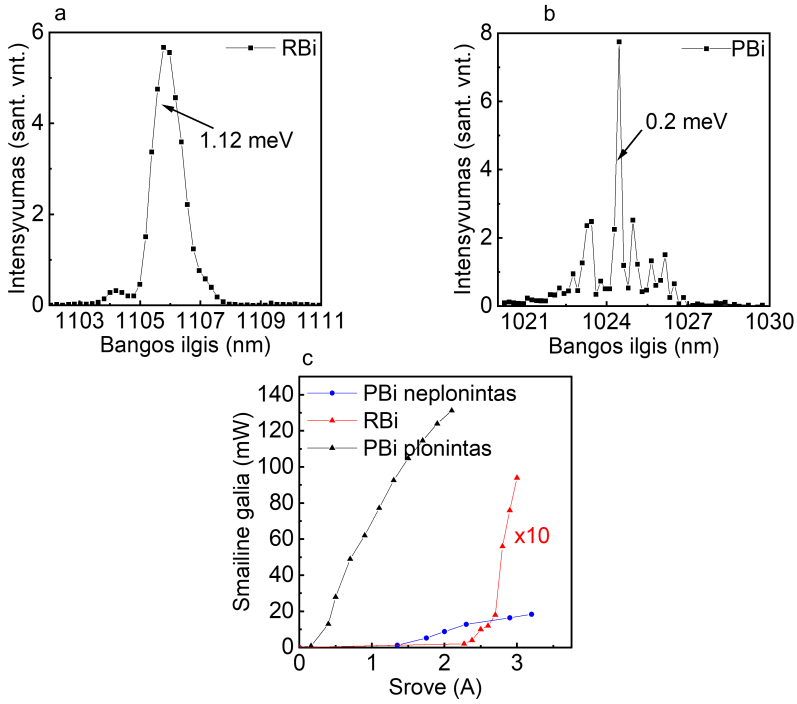

3.42 paveikslas: Lazerinių diodų lazeriavimo spektrai: a) prietaisui, veikiančiam standartinių stačiakampių kvantinių duobių pagrindu; b) prietaisui su paraboliškai graduotais barjerais (spektruose a) ir b) 1,12 meV ir 0,2 meV atitinka centrinės emisijos linijos FWHM); c) lazerinių diodų smailinės galios priklausomybė nuo įveikinimo srovės: stačiakampių kvantinių duobių lazeriui (raudona) ir lazeriams su paraboliškai graduotais barjerais – neplonintu padėklu (mėlyna) bei plonintu padėklu (juoda).

ESA projektą IR Bi pagrindu veikiančių šaltinių Irbis (sutarties Nr. 4000122271/NL/SC) ir buvo patikrinti nepriklausomų ekspertų.

3.10.1. DBR projektavimas ir augimas

Apskaičiuoti GaAs/AlAs DBR projektavimo parametrai keturiuose emisijos bangos ilgiuose yra apibendrinti 3.13 lentelėje. Atspindžiui apie 100 % ir šilumos laidumui subalansuoti buvo pasirinkta 30 periodų struktūra.

3.13 lentelė: GaAs/AlAs DBR projektavimo parametrai įvairiems bangos ilgiams.

Parametras	976 nm	1030 nm	1060 nm	1160 nm
n_{GaAs}	3,5253	34926	3,4779	3,4413
n_{AlAs}	2,9680	2,9577	2,9526	2,9389
d_{GaAs} (nm)	69,21	73,73	76,20	84,27
d_{AlAs} (nm)	82,21	87,06	89,75	98,68
Bendras storis (nm)	4536,30	4841,70	4988,55	5490,00
Juostos plotis (nm)	106,79	108,88	110,37	116,42

3.10.2. Aktyviosios terpės dizainas

Kiekvieną stiprinimo sritį sudaro 12 QW. InGaAs QW buvo naudojamos 976 ir 1030 nm VECSEL, o GaAsBi – 1060 ir 1160 nm VECSEL. Norint sulygiuoti optinio lauko antinodes su QW, pirmoji antinodė buvo sutapatinama su pirmosios QW centru, todėl tikslus pirmojo barjero storis buvo labai svarbus (žr. 3.43(a) paveikslą). Siekiant sumažinti bendrą storį ir pagerinti šilumos nuvedimą, buvo pasitelktas dizainas, kuriame naudojamos QW poros, atskirtos plonais barjerais (3.43(b) paveikslas). Antinodės tuo atveju buvo sulygiuojamos su plono barjero centru.
Kiekvieno dizaino sluoksnių storiai pateikti 3.14 lentelėje.

3.10.3. Auginimas

Auginimas prasideda nuo DBR ant 2 colių GaAs padėklo esant 600 °C temperatūrai, po to aktyvi terpė buvo auginama žemes-

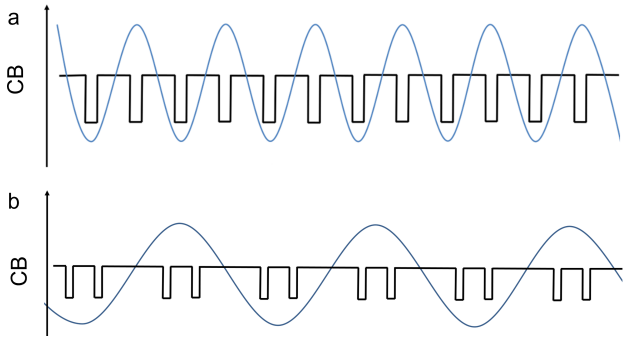

3.43 paveikslas: Dviejų VECSEL stiprinimo sričių laidumo juostų profiliai ir optinės stovinčios bangos projektavimas: (a) pavienėms QW, (b) susietoms poromis QW ir atskirtoms storais barjerais.

3.14 lentelė: VECSEL struktūros parametrai įvairiems emisijos bangos ilgiams: n - lūžio rodiklis, d - kvantinių duobių ir barjerų storiai.

λ (nm)	Medžiaga	n_{qw}	d_{qw} (nm)	d_{plono} (nm)	d_{tarpinio} (nm)	$d_{\mathrm{pirm./\ paskut.}}$(nm)	Bendras (nm)
976	InGaAs	3,56	5,7	7	123,34	130,88	988,9
1030	InGaAs	3,53	7,6	12	119,58	133,52	1028,1
1060	GaAsBi	3,51	5,5	7	134,30	143,34	1066,2
1160	GaAsBi	3,54	5,5	7	150,23	159,39	1177,9
1160	GaAsBi	3,54	5,5	–	162,89	165,72	2145,3

nėje temperatūroje, optimizuotoje InGaAs ir GaAsBi kvantinėms duobėms. Toje pat temperatūroje buvo formuojamas dengiamasis lango sluoksnis, kuris tarnauja šviesos ekstrakcijai.

Charakterizavimas

Visos struktūros buvo charakterizuojamos RTPL ir atspindžio matavimais (3.44 pav.). 3.15 lentelėje pateiktos RTPL smailių Gauso aproksimacijos. Buvo nustatyta kad GaAsBi struktūrų puspločio FWHM vertės yra žymiai siauresnės nei tikėtasi.
TDPL buvo matuotas 40–140 °C temperatūroje InGaAs ir GaAsBi struktūroms (žr. 3.45 pav.). Iš matavimų spektrų buvo įvertintas maždaug -0.1 meV °C^{-1} tiesinis poslinkis (3.46 pav.).

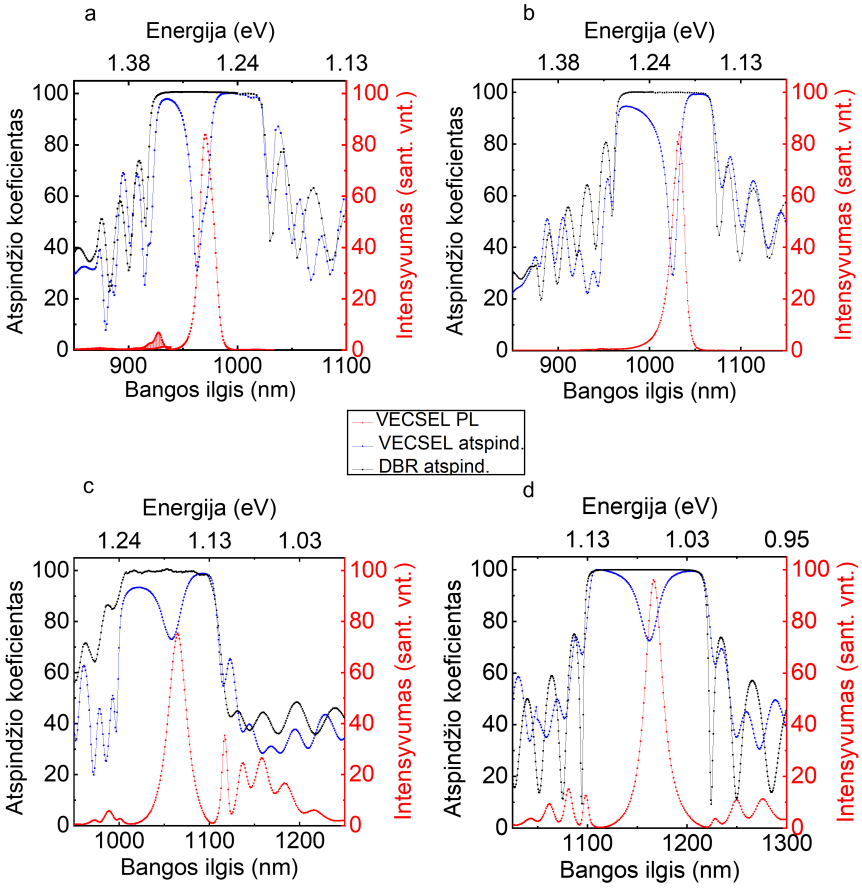

3.44 paveikslas: RTPL (raudona) ir atspindys (mėlyna) išmatuoti skirtingoms VECSEL struktūroms; juoda kreivė žymi DBR be MQW atspindį.

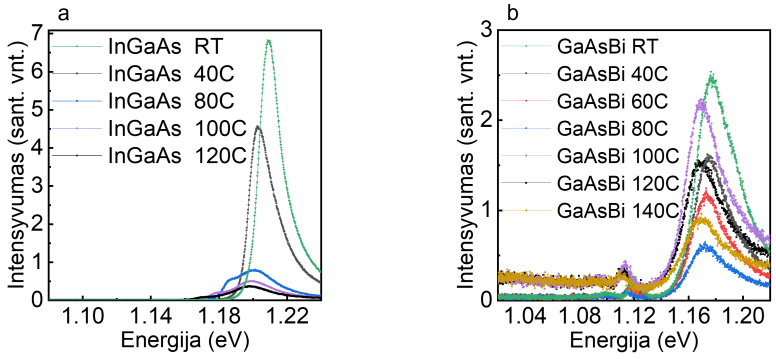

3.45 paveikslas: InGaAs ir GaAsBi pagrindu sukurtų VECSELs TDPL spektrai.

3.15 lentelė: RTPL spektrų Gauso aproksimacijos rezultatai.

Bandinys	Centrinė energija (eV)	Centrinis bangos iligis (nm)	FWHM (meV)
VECSEL975	1,27607	971,24	19,82
VECSEL1030	1,20247	1031,08	19,66
VECSEL1060	1,16451	1064,12	22,50
VECSEL1160	1,06242	1166,37	21,14

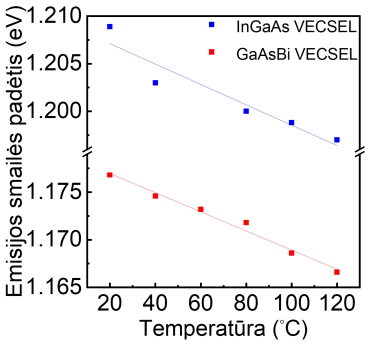

3.46 paveikslas: Emisijos energijos priklausomybė nuo temperatūros, pritaikyta tiesinė aproksimacija.

3.11. Lazerinis spinduliavimas

Lazerinio spinduliavimo bandymai buvo atlikti Vilniaus universiteto Lazerinių tyrimų centre. Lustai buvo sumontuoti ant vario plokštelių ir Peltje elementu aušinami iki 16–22 °C. Kaupinimas buvo vykdomas naudojant 808 nm lazerinį diodą, sufokusuotą į 300 µm dėmę. Dėl riboto išorinio rezonatoriaus veidrodžio diapazono (1020–1080 nm) buvo įvertintos tik 1060 nm ir 976 nm struktūros. Lazerinio spinduliavimo pagrindinė moda InGaAs VECSEL struktūrai buvo užregistruota ties 973 nm, o antrinė emisija ties 1005 nm (3.47 pav.). GaAsBi pagrindu suformuoto VECSEL lazerinė spinduliuotė siekė ilgesnes bangas ties 1070 nm, o spektrinės linijos pusplotis siekėvos 10 meV.

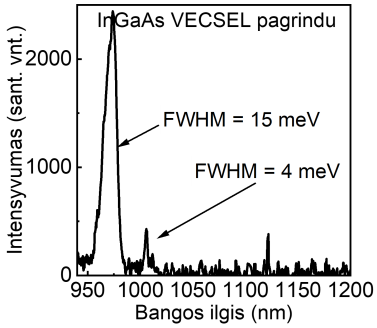

3.47 paveikslas: InGaAs pagrindu 976 nm bangos ilgiui sukurto VECSEL lazerio spektras, užregistruotas esant kambario temperatūrai.

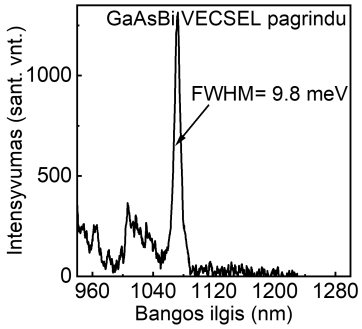

3.48 paveikslas: GaAsBi MQW pagrindu sukurto VECSEL lazerio spektras, užregistruotas kambario temperatūroje.

3.12. Išvados

Toliau apibendrinami pagrindiniai šio darbo rezultatai, ypatingą dėmesį skiriant tiems, kurie buvo pateikti arba priimti publikuoti recenzuojamuose žurnaluose. Dauguma šių išvadų anksčiau buvo pristatytos tarptautinėse konferencijose paties autoriaus arba bendraautorių. Išsamus konferencijų, kuriose dalyvavo daugiau nei 50 dalyvių, sąrašas pateikiamas šios disertacijos pradžioje.

1. Optimizuojant InGaAs pagrindu daugybinių kvantinių duobių technologiją buvo atskleisti trys svarbūs aspektai. Pirma, po auginimo buvo tirtas atkaitinimo poveikis InGaAs RTPL intensyvumui, ir nustatyta, kad optimali augimo temperatūra yra 510 °C. Aukštesnė temperatūra pagerino AlAs ir GaAs

kristalų kokybę, tačiau sukėlė In segregaciją, kuri labai sumažino emisijos intensyvumą. Antra, buvo sumodeliuota deformacijų generacija ir nustatyta, kad MQW struktūrose, turinčiose daugiau nei tris QW, atskirtas plonais (7 nm) barjerais, vyksta MD formavimąsis. Tačiau šis modelis nepasiteisino, kai buvo įvesti stori barjerai (> 100 nm). Dėl to InGaAs pagrindu veikiantiems VECSEL, siekiant išvengti dislokacijų, galima naudoti struktūras su kvantinių duobių poromis arba viena QW. Trečia, buvo įvertintas barjerų sudėties vaidmuo, nustatant 12 % Al kaip optimalią kompromisinę sudėtį tarp stipraus krūvininkų koncentravimo duobėje ir didelio kambario temperatūros spinduliavimo artimojoje infraraudonojoje srityje našumo.

2. Optimizavus GaAsBi MQW technologinius parametrus, nustatyta, kad GaAsBi sluoksniai, kuriuose yra iki 10 % Bi, gali išlikti pseudomorfiniai deformacijos atžvilgiu net ir esant dideliam QW skaičiui. Buvo nustatytas tikslus augimo langas, kuriame Bi įterpimą daugiausia kontroliuoja padėklo temperatūra (300–350 °C), Bi šaltinio temperatūra (500–530 °C) ir As_2/Ga BEPR 0,85–1,2 diapazone. Be to, buvo parodyta, kad dengiamojo GaAs sluoksnio auginimas aukštoje temperatūroje sukelia ∼50 meV mėlynąjį poslinkį dėl Bi segregacijos, tuo pačiu metu padidina PL intensyvumą, sumažina nespindulinę rekombinaciją. Projektuojant pilną lazerio struktūrą būtina atsižvelgti į abu efektus.

3. Norint įvertinti GaAsBi struktūrų IQE, buvo sukurtas modifikuotas ABC rekombinacijos modelis, kuris neįtraukia Auger rekombinacijos bet apima krūvininkų gaudyklių sukeltos Auger rekombinacijos mechanizmą. Šio modelio taikymas keliems GaAsBi bandiniams patvirtino didelį krūvininkų gaudyklių indėlį, todėl ABC modelis tapo patikimu pirmos iteracijos įrankiu bismido struktūrų vidiniam našumui įvertinti.

4. Siekiant optimizuoti GaAsBi MQW technologiją VECSEL struktūroms buvo pagaminti LD naudojant skirtingas kvantinių struktūrų geometrijas tiek stačiakampes QW, tiek ir QW su paraboliniais barjerais. LD su GaAsBi QWs apsuptomis paraboliniais barjerais aktyviojoje terpėje pasižymėjo geresniais rezultatais, įskaitant didesnę išėjimo galią ir mažesnes

slenkstines sroves. Be to, buvo įrodyta, kad padėklo ploninimas dar labiau pagerina charakteristikas.

5. Buvo suprojektuoti, išauginti ir charakterizuoti VECSEL keturiems emisijos bangos ilgiams. InGaAs pagrindu sukurti lazeriai buvo skirti trumpesniems bangos ilgiams (976 nm ir 1030 nm), o GaAsBi pagrindu sukurti lazeriai – ilgesniems 1060 nm ir 1160 nm. Testavimas patvirtino projektavimo metodo pagrįstumą: RTPL ir atspindžio spektrai parodė numatytą emisijos ir DBR fotoninės stabdymo juostos centro persidengimą. Nuo temperatūros priklausantys TDPL matavimai (40–140 °C) atskleidė geresnį GaAsBi pagrindu pagamintų lazerių terminį stabilumą, lyginant su InGaAs. Lazerinis spinduliavimas buvo pasiektas abiejose medžiagų sistemose: InGaAs pagrindu sukurtas VECSEL parodė stimuliuojamą emisiją ties 973 nm su ženkliu spektro susiaurėjimu ir išilginės modos atsiradimu, o GaAsBi pagrindu sukurtas lazeris veikė ties 1070 nm. Nuo galios priklausantys tyrimai atskleidė tik nedidelį lazerio bangos ilgio (1070–1073 nm) raudonąjį poslinkį, priskiriamą lokaliam kaitinimui, kas dar labiau patvirtino GaAsBi pagrindu sukurtų VECSEL terminį stabilumą.

Bibliography

[1] R. D. Richards, N. J. Bailey, Y. Liu, T. B. O. Rockett, A. R. Mohmad, GaAsBi: from molecular beam epitaxy growth to devices, Physica Status Solidi (b) **259**(2), 2100330 (2022), https://doi.org/10.1002/pssb.202100330.

[2] S. Tixier, M. Adamcyk, T. Tiedje, S. Francoeur, A. Mascarenhas, P. Wei, F. Schiettekatte, Molecular beam epitaxy growth of $GaAs_{1-x}Bi_x$, Applied Physics Letters **82**(14), 2245–2247 (2003), https://doi.org/10.1063/1.1565499.

[3] H. Li, S. Wang, Molecular Beam Epitaxy Growth and Properties of GaAsBi and AlAsBi, in *Molecular Beam Epitaxy* (Springer, Singapore, 2019), 29–58.

[4] K. Oe, H. Okamoto, New Semiconductor Alloy $GaAs_{1-x}Bi_x$ Grown by Metal Organic Vapor Phase Epitaxy, Japanese Journal of Applied Physics **37**(11A), L1283 (1998), https://doi.org/10.1143/JJAP.37.L1283.

[5] H. Fitouri, I. Moussa, A. Rebey, A. Fouzri, B. El Jani, AP-MOVPE of thin $GaAs_{1-x}Bi_x$ alloys, Journal of Crystal Growth **295**(2), 114–118 (2006), https://doi.org/https://doi.org/10.1016/j.jcrysgro.2006.06.052.

[6] B. Fluegel, S. Francoeur, A. Mascarenhas, S. Tixier, E. C. Young, T. Tiedje, Giant Spin-Orbit Bowing in $GaAs_{1-x}Bi$, Phys. Rev. Lett. **97**(6), 067205 (2006), https://doi.org/10.1103/PhysRevLett.97.067205.

[7] Z. Batool, K. Hild, T. J. C. Hosea, X. Lu, T. Tiedje, S. J. Sweeney, The Electronic Band Structure of GaAsBi/GaAs Layers: Influence of Strain and Band Anti-Crossing, J. Appl. Phys. **111**(11), 113108 (2012), https://doi.org/10.1063/1.4728028.

[8] Ł. Gelczuk, J. Kopaczek, T. B. O. Rockett, R. D. Richards, R. Kudrawiec, Deep-level defects in n-type GaAsBi alloys grown by molecular beam epitaxy at low tempera-

ture, Journal of Applied Physics **113**(13), 133708 (2013), https://doi.org/10.1063/1.4798237.

[9] S. Francoeur, M.-J. Seong, A. Mascarenhas, S. Tixier, M. Adamcyk, T. Tiedje, Band gap of $GaAs_{1-x}Bi_x$, 0 <x <3.6 %, Applied Physics Letters **82**, 3874 – 3876 (2003), https://doi.org/10.1063/1.1581983.

[10] Y. Liu, X. Yi, N. Bailey, Z. Zhou, T. Rockett, L. Lim, C. Tan, R. Richards, J. David, Valence band engineering of GaAsBi for low noise avalanche photodiodes, Nature Communications **12**, 4784 (2021), https://doi.org/10.1038/s41467-021-24966-0.

[11] V. Pačebutas, K. Bertulis, G. Aleksejenko, A. Krotkus, Molecular-beam-epitaxy grown GaBiAs for terahertz optoelectronic applications, Journal of Materials Science: Materials in Electronics **20**, 363–366 (2009), https://doi.org/10.1007/s10854-008-9625-1.

[12] H. Wei, K. Oe, G. Feng, M. Yoshimoto, Molecular-beam epitaxy and characteristics of $GaN_yAs_{1-x-y}Bi_x$, Journal of Applied Physics - J APPL PHYS **98**, 053505–053505 (2005), https://doi.org/10.1063/1.2032618.

[13] I. P. Marko, S. J. Sweeney, Progress Toward III–V Bismide Alloys for Near- and Midinfrared Laser Diodes, IEEE Journal of Selected Topics in Quantum Electron. **23**(6), 150–1512 (2017), https://doi.org/10.1109/JSTQE.2017.2719403.

[14] X. Lu, D. A. Beaton, R. B. Lewis, T. Tiedje, Y. Zhang, Composition dependence of photoluminescence of $GaAs_{1-x}Bi_x$ alloys, Applied Physics Letters **95**(4), 041903 (2009), https://doi.org/10.1063/1.3191675.

[15] O. Kunishige, Characteristics of Semiconductor Alloy $GaAs_{1-x}Bi_x$, Jpn. J. Appl. Phys. **41**(5R), 2801 (2002), https://doi.org/10.1143/JJAP.41.2801.

[16] I. Vurgaftman, J. R. Meyer, L. R. Ram-Mohan, Band parameters for III–V compound semiconductors and their alloys, Journal of Applied Physics **89**(11), 5815–5875 (2001), https://doi.org/10.1063/1.1368156.

[17] S. Mazzucato, T. T. Zhang, H. Carrère, D. Lagarde, P. Boonpeng, A. Arnoult, G. Lacoste, A. Balocchi, T. Amand, C. Fontaine, X. Marie, Electron spin dynamics and g-factor in GaAsBi, Applied Physics Letters **102**(25), 252107 (2013), https://doi.org/10.1063/1.4812660.

[18] T. Fuyuki, R. Yoshioka, K. Yoshida, M. Yoshimoto, GaAsBi laser diodes with low temperature dependence of lasing wavelength, in *2014 Conference on Lasers and Electro-Optics (CLEO) - Laser Science to Photonic Applications* (2014), 1–2.

[19] K. Alberi, O. Dubon, W. Walukiewicz, K. Yu, K. Bertulis, A. Krotkus, Valence Band Anticrossing in $GaBi_xAs_{1-x}$, Applied Physics Letters - APPL PHYS LETT **91** (2007), https://doi.org/10.1063/1.2768312.

[20] T. Thomas, A. Mellor, N. P. Hylton, M. Führer, D. Alonso-Álvarez, A. Braun, Requirements for a GaAsBi 1 eV Sub-Cell in a GaAs-based Multi-Junction Solar Cell, Semicond. Sci. Technol. **30**(9), 094010 (2015), https://doi.org/10.1088/0268-1242/30/9/094010.

[21] L. Yu, D. Li, S. Zhao, G. Li, K. Yang, First Principles Study on Electronic Structure and Optical Properties of Ternary GaAs:Bi Alloy, Materials **5**(12), 2486 (2012), https://doi.org/10.3390/ma5122486.

[22] X. Lu, D. A. Beaton, R. B. Lewis, T. Tiedje, M. B. Whitwick, Effect of molecular beam epitaxy growth conditions on the Bi content of $GaAs_{1-x}Bi_x$, Applied Physics Letters **92**(19), 192110 (2008), https://doi.org/10.1063/1.2918844.

[23] R. B. Lewis, M. Masnadi-Shirazi, T. Tiedje, Growth of high Bi concentration $GaAs_{1-x}Bi_x$ by molecular beam epitaxy, Applied Physics Letters **101**(8), 082112 (2012), https://doi.org/10.1063/1.4748172.

[24] G. Vardar, S. W. Paleg, M. V. Warren, M. Kang, S. Jeon, R. S. Goldman, Mechanisms of droplet formation and Bi incorporation during molecular beam epitaxy of GaAsBi, Applied Physics Letters **102**(4), 042106 (2013), https://doi.org/10.1063/1.4789369.

[25] C. Foxon, B. Joyce, Interaction kinetics of As_4 and Ga on 100 GaAs surfaces using a modulated molecular beam technique, Surface Science **50**(2), 434–450 (1975), https://doi.org/https://doi.org/10.1016/0039-6028(75)90035-7.

[26] C. Foxon, B. Joyce, Interaction kinetics of As_2 and Ga on 100 GaAs surfaces, Surface Science **64**(1), 293–304 (1977), https://doi.org/https://doi.org/10.1016/0039-6028(77)90273-4.

[27] R. D. Richards, F. Bastiman, C. J. Hunter, D. F. Mendes, A. R. Mohmad, J. S. Roberts, J. P. David, Molecular beam epitaxy growth of GaAsBi using As_2 and As_4, Journal of Crystal Growth **390**, 120–124 (2014), https://doi.org/https://doi.org/10.1016/j.jcrysgro.2013.12.008.

[28] M. Masnadi-Shirazi, D. Beaton, R. Lewis, X. Lu, T. Tiedje, Surface reconstructions during growth of $GaAs_{1-x}Bi_x$ alloys by molecular beam epitaxy, Journal of Crystal Growth **338**(1), 80–84 (2012), https://doi.org/https://doi.org/10.1016/j.jcrysgro.2011.09.055.

[29] H. Ye, Y. Song, Y. Gu, S. Wang, Light emission from InGaAs:Bi/GaAs quantum wells at 1.3 µm, AIP Advances **2**(4), 042158 (2012), https://doi.org/10.1063/1.4769102.

[30] F. Bastiman, A. Mohmad, J. Ng, J. David, S. Sweeney, Non-stoichiometric GaAsBi/GaAs (100) molecular beam epitaxy growth, Journal of Crystal Growth **338**(1), 57–61 (2012), https://doi.org/https://doi.org/10.1016/j.jcrysgro.2011.07.036.

[31] N. Ben Sedrine, I. Moussa, H. Fitouri, A. Rebey, B. Jani, R. Chtourou, Spectroscopic ellipsometry study of $GaAs_{1-x}Bi_x$ material grown on GaAs substrate by atmospheric pressure metal-organic vapor-phase epitaxy, Applied Physics Letters **95** (2009), https://doi.org/10.1063/1.3167359.

[32] I. P. Marko, C. A. Broderick, S. Jin, P. Ludewig, W. Stolz, K. Volz, J. M. Rorison, E. P. O'Reilly, S. J. Sweeney, Optical Gain in GaAsBi/GaAs Quantum Well Diode Lasers, Sci. Rep. **6**, 28863 (2016), https://doi.org/10.1038/srep28863.

[33] J. Liu, W. Pan, x. wu, C. Cao, L. Yaoyao, C. Xiren, Y. Zhang, L. Wang, J. Yan, D. Zhang, Y. Song, J. Shao, S. Wang, Electrically injected GaAsBi/GaAs single quantum well laser diodes, AIP Advances **7**, 115006 (2017), https://doi.org/10.1063/1.4985231.

[34] R. Butkutė, A. Geižutis, V. Pačebutas, B. Čechavičius, V. Bukauskas, R. Kundrotas, P. Ludewig, K. Volz, A. Krotkus, Multi-quantum well Ga(AsBi)/GaAs laser diodes with more than 6% of bismuth, Electronics Letters **50**(16), 1155–1157 (2014), https://doi.org/https://doi.org/10.1049/el.2014.1741.

[35] M. Guina, A. Rantamäki, A. Härkönen, *Optically pumped VECSELs: review of technology and progress*, volume 50 (IOP Publishing, 2017).

[36] B. Heinen, T.-L. Wang, M. Sparenberg, A. Weber, B. Kunert, J. Hader, S. Koch, J. Moloney, M. Koch, W. Stolz, 106 W continuous-wave output power from vertical-external-cavity surface-emitting laser, Electronics Letters **48**, 516–517 (2012), https://doi.org/10.1049/el.2012.0531.

[37] A. Laurain, J. Hader, Y.-Y. Lai, T.-L. Wang, M. Yarborough, G. Balakrishnan, T. J. Rotter, P. Ahirwar, J. V. Moloney, Influence of non-radiative carrier losses on pulsed and continuous VECSEL performance, in A. C. Tropper (ed.), *Vertical External Cavity Surface Emitting Lasers (VECSELs) II*, International Society for Optics and Photonics (SPIE, 2012), volume 8242, 82420S.

[38] J. Chilla, Q.-Z. Shu, H. Zhou, E. Weiss, M. Reed, L. Spinelli, Recent advances in optically pumped semiconductor lasers, in H. J. Hoffman, R. K. Shori, N. Hodgson (eds.), *Solid State Lasers XVI: Technology and Devices*, International Society for Optics and Photonics (SPIE, 2007), volume 6451, 645109.

[39] A. Kemp, G. Valentine, J.-M. Hopkins, J. Hastie, S. Smith, S. Calvez, M. Dawson, D. Burns, Thermal management in vertical-external-cavity surface-emitting lasers: finite-element analysis of a heatspreader approach, IEEE Journal of Quantum Electronics **41**(2), 148–155 (2005), https://doi.org/10.1109/JQE.2004.839706.

[40] H. Lindberg, M. Strassner, E. Gerster, J. Bengtsson, A. Larsson, Thermal management of optically pumped long-wavelength InP-based semiconductor disk lasers, IEEE Journal of Selected Topics in Quantum Electronics **11**(5), 1126–1134 (2005), https://doi.org/10.1109/JSTQE.2005.853730.

[41] D. T. D. Childs, J. R. Orchard, D. Williams, L.-C. Lin, B. J. Stevens, J. Roberts, R. A. Hogg, Trade-offs in the realization of electrically pumped vertical external cavity surface emitting lasers, in *22nd IEEE International Semiconductor Laser Conference* (2010), 87–88.

[42] D. Findlay, R. A. Clay, The measurement of internal losses in 4-level lasers, Physics Letters **20**(3), 277–278 (1966), https://doi.org/10.1016/0031-9163(66)90363-5.

[43] U. Keller, A. C. Tropper, Passively mode-locked surface-emitting semiconductor lasers, Physics Reports **429**(2), 67–120 (2006), https://doi.org/https://doi.org/10.1016/j.physrep.2006.03.004.

[44] S. Y. Hu, D. B. Young, S. W. Corzine, A. C. Gossard, L. A. Coldren, High-efficiency and low-threshold InGaAs/AlGaAs quantum-well lasers, Journal of Applied Physics **76**(6), 3932–3934 (1994), https://doi.org/10.1063/1.357408.

[45] F. Beffa, H. Jäckel, M. Achtenhagen, C. Harder, D. Erni, High-temperature optical gain of 980 nm InGaAs/AlGaAs quantum-well lasers, Applied Physics Letters **77**(15), 2301–2303 (2000), https://doi.org/10.1063/1.1317541.

[46] L. Han, M. Zhao, X. Tang, W. Huo, Z. Deng, Y. Jiang, W. Wang, H. Chen, C. Du, H. Jia, Luminescence study in InGaAs/AlGaAs multi-quantum-well light emitting diode with p-n junction engineering, Journal of Applied Physics **127**(15), 153102 (2020), https://doi.org/10.1063/1.5136300.

[47] H. Yang, Y. Zheng, Z. Tang, N. Li, X. Zhou, P. Chen, J. Wang, MBE growth of high performance very long wavelength InGaAs/GaAs quantum well infrared photodetectors, Journal of Physics D: Applied Physics **53**(13), 135110 (2020), https://doi.org/10.1088/1361-6463/ab66d7.

[48] K. Chan, M. Lightner, G. Patterson, K. Yu, Growth studies of pseudomorphic GaAs/InGaAs/AlGaAs modulation-doped field-effect transistor structures, Applied Physics Letters **56**(20), 2022–2024 (1990), https://doi.org/10.1063/1.103005.

[49] M. Motyka, G. Sęk, R. Kudrawiec, P. Sitarek, J. Misiewicz, J. Wojcik, B. J. Robinson, D. A. Thompson, P. Mascher, Probing the indium clustering in InGaAs/GaAs quantum wells by room temperature contactless electroreflectance and photoluminescence spectroscopy, Journal of Applied Physics **101**(11), 116107 (2007), https://doi.org/10.1063/1.2745400.

[50] Zheng, Walker, Salmerón, Weber, Interface segregation and clustering in strained-layer InGaAs/GaAs heterostructures studied by cross-sectional scanning tunneling microscopy, Physical review letters **72 15**, 2414–2417 (1994), https://doi.org/10.1103/PHYSREVLETT.72.2414.

[51] S. S. Bhat, S. Bhattacharjee, J.-H. Choi, S.-C. Lee, Influence of surface structure and strain on indium segregation in InGaAs: a first-principles investigation (2020), https://arxiv.org/abs/2010.14106.

[52] K. Muraki, S. Fukatsu, Y. Shiraki, R. Ito, Surface segregation of In atoms and its influence on the quantized levels in InGaAs/GaAs quantum wells, Journal of Crystal Growth **127**(1), 546–549 (1993), https://doi.org/10.1016/0022-0248(93)90680-U.

[53] C. M. Yee-Rendón, A. Perez-Centeno, M. Meléndez-Lira, G. G. de la Cruz, M. Lopez-Lopez, K. Furuya, P. O. Vaccaro, Interdiffusion of Indium in piezoelectric InGaAs-GaAs quantum wells grown by molecular beam epitaxy on (11n) substrates, Journal of Applied Physics **96**(7), 3702–3708 (2004), https://doi.org/10.1063/1.1783611.

[54] R. Kaspi, K. R. Evans, Improved compositional abruptness at the InGaAs on GaAs interface by presaturation with In during molecular-beam epitaxy, Applied Physics Letters **67**(6), 819–821 (1995), https://doi.org/10.1063/1.115454.

[55] M. Choubani, H. Maaref, F. Saidi, Indium segregation and In–Ga inter-diffusion effects on the photoluminescence measurements and nonlinear optical properties in lens-shaped $In_xGa_{1-x}As/GaAs$ quantum dots, Journal of Physics and Chemistry of Solids **160**, 110360 (2022), https://doi.org/10.1016/J.JPCS.2021.110360.

[56] F. Lelarge, C. Constantin, K. Leifer, A. Condó, V. Iakovlev, E. Martinet, A. Rudra, E. Kapon, Effect of indium segregation on optical properties of V-groove InGaAs/GaAs strained quantum wires, Applied Physics Letters **75**, 3300–3302 (1999), https://doi.org/10.1063/1.125331.

[57] F. Ishikawa, E. Luna, A. Trampert, K. H. Ploog, Critical parameters for the molecular beam epitaxial growth of (Ga,In)(N,As) multiple quantum wells, Journal of Applied Physics **89**(19), 191907 (2006), https://doi.org/10.1063/1.2372760.

[58] E. Luna, F. Ishikawa, P. Batista, A. Trampert, Indium distribution at the interfaces of (Ga, In)(N, As)/ GaAs quantum wells, Applied Physics Letters **92**(14) (2008), https://doi.org/10.1063/1.2907508.

[59] J. Gerard, G. Roux, Growth of InGaAs/GaAs quantum wells with perfectly abrupt interfaces by molecular beam epitaxy, Applied Physics Letters **62**, 3452–3454 (1993), https://doi.org/10.1063/1.109046.

[60] P. R. Griffin, J. Barnes, K. Barnham, G. Haarpaintner, M. Mazzer, C. Zanotti-Fregonara, E. Grünbaum, C. Olson, C. Rohr, J. David, et al., Effect of strain relaxation on forward bias dark currents in GaAs/InGaAs multiquantum well p–i–n diodes, Journal of Applied Physics **80**(10), 5815–5820 (1996), https://doi.org/10.1063/1.363574.

[61] E. Fitzgerald, D. Ast, P. Kirchner, G. Pettit, J. Woodall, Structure and recombination in InGaAs/GaAs heterostructures, Journal of applied physics **63**(3), 693–703 (1988), https://doi.org/10.1063/1.340059.

[62] J. Jiménez, Laser diode reliability: crystal defects and degradation modes, Comptes Rendus

Physique **4**(6), 663–673, dossier: Semiconductor lasers (2003), https://doi.org/https://doi.org/10.1016/S1631-0705(03)00097-5.

[63] S. Ranta, T. Hakkarainen, M. Tavast, J. Lindfors, T. Leinonen, M. Guina, Strain compensated 1120nm GaInAs/GaAs vertical external-cavity surface-emitting laser grown by molecular beam epitaxy, Journal of Crystal Growth **335**(1), 4–9 (2011), https://doi.org/https://doi.org/10.1016/j.jcrysgro.2011.08.044.

[64] Y. Ohizumi, T. Tsuruoka, S. Ushioda, Formation of misfit dislocations in GaAs/InGaAs multiquantum wells observed by photoluminescence microscopy, Journal of Applied Physics **92**, 2385–2390 (2002), https://doi.org/10.1063/1.1496121.

[65] J. Wang, J. W. Steeds, D. A. Woolf, The study of misfit dislocations in $In_xGa_{1-x}As$/GaAs strained quantum well structures, Philosophical Magazine A **65**(4), 829–839 (1992), https://doi.org/10.1080/01418619208205592.

[66] D. Houghton, M. Davies, M. Dion, Design criteria for structurally stable, highly strained multiple quantum well devices, Applied physics letters **64**(4), 505–507 (1994), https://doi.org/10.1063/1.111111.

[67] J.-M. Hopkins, et al., 0.6 W CW GaInNAs vertical external-cavity surface emitting laser operating at 1.32 µm, Electronics Letters **40**, 30–31 (2004), https://doi.org/10.1049/el:20040049.

[68] M. Guina, T. Leinonen, A. Härkönen, M. Pessa, High-power disk lasers based on dilute nitride heterostructures, New Journal of Physics **11**(12), 125019 (2009), https://doi.org/10.1088/1367-2630/11/12/125019.

[69] V.-M. Korpijärvi, T. Leinonen, J. Puustinen, A. Härkönen, M. D. Guina, 11 W single gain-chip dilute nitride disk laser emitting around 1180 nm, Optics express **18**(25), 25633–25641 (2010), https://doi.org/10.1364/OE.18.025633.

[70] V.-M. Korpijärvi, E. L. Kantola, T. Leinonen, R. Isoaho, M. Guina, Monolithic GaInNAsSb/GaAs VECSEL operating at 1550 nm, IEEE Journal of Selected Top-

ics in Quantum Electronics **21**(6), 480–484 (2015), https://doi.org/10.1109/JSTQE.2015.2415200.

[71] N. Derriche, S. Godin, R. Greenwood, A. Mercado, A. N. Warner, Reflection High-Energy Electron Diffraction (2019).

[72] M. Mahtab, R. Synowicki, V. Bahrami-Yekta, L. C. Bannow, S. W. Koch, R. B. Lewis, T. Tiedje, Complex dielectric function of $GaAs_{1-x}Bi_x$ as a function of Bi content, Phys. Rev. Mater. **3**(5) (2019), https://doi.org/10.1103/PhysRevMaterials.3.054601.

[73] M. Ferhat, A. Zaoui, Structural and electronic properties of III-V bismuth compounds, Phys. Rev. B Condens. Matter Mater. Phys. **73**(11) (2006), https://doi.org/10.1103/PhysRevB.73.115107.

[74] A. Janotti, S.-H. Wei, S. B. Zhang, Theoretical study of the effects of isovalent coalloying of Bi and N in GaAs, Phys. Rev. B Condens. Matter **65**(11) (2002), https://doi.org/10.1103/PhysRevB.65.115203.

[75] V. Karpus, R. Norkus, R. Butkutė, S. Stanionytė, B. Čechavičius, A. Krotkus, THz-excitation spectroscopy technique for band-offset determination, Opt. Express **26**(26), 33807–33817 (2018), https://doi.org/10.1364/OE.26.033807.

[76] K. Chang, J.-S. Wu, D. Liu, D. Liou, C. Lee, High quality AlGaAs layers grown by molecular beam epitaxy at low temperatures, Journal of Materials Science: Materials in Electronics **3**, 11–15 (1992).

[77] W. Liu, Investigation of electrical and photoluminescent properties of MBE-grown $Al_xGa_{1-x}As$ layers, Journal of materials science **25**, 1765–1772 (1990).

[78] Y. Yazawa, T. Kitatani, J. Minemura, K. Tamura, K. Mochizuki, T. Warabisako, AlGaAs solar cells grown by MBE for high-efficiency tandem cells, Solar Energy Materials and Solar Cells **35**, 39–44 (1994), https://doi.org/https://doi.org/10.1016/0927-0248(94)90120-1.

[79] A. Chin, K. Lee, High quality Al(Ga)As/GaAs/Al(Ga)As quantum wells grown on (111)A GaAs substrates, Applied Physics Letters **68**(24), 3437–3439 (1996), https://doi.org/10.1063/1.115785.

[80] S. Miyazawa, Y. Sekiguchi, M. Okuda, High-reliability GaAs/AlGaAs multiquantum well lasers grown at a low temperature (375°C), Applied Physics Letters **63**(26), 3583–3585 (1993), https://doi.org/10.1063/1.110104.

[81] A. Álvarez, F. Calle, J. Valtueña, J. Faura, M. Sánchez, E. Calleja, E. Muñoz, J. Morante, D. González, D. Araujo, R. García Roja, Influence of interface dislocations on surface kinetics during epitaxial growth of InGaAs, Applied Surface Science **123-124**, 303–307 (1998), https://doi.org/https://doi.org/10.1016/S0169-4332(97)00483-2.

[82] Y. Varshni, Temperature dependence of the energy gap in semiconductors, Physica **34**(1), 149–154 (1967), https://doi.org/https://doi.org/10.1016/0031-8914(67)90062-6.

[83] J. Puustinen, J. Hilska, M. Guina, Analysis of GaAsBi growth regimes in high resolution with respect to As/Ga ratio using stationary MBE growth, Journal of Crystal Growth **511**, 33–41 (2019), https://doi.org/https://doi.org/10.1016/j.jcrysgro.2019.01.010.

[84] A. Vaitkevičius, A. Špokas, A. Zelioli, U. Cibulskaitė, A. Bičiūnas, E. Dudutienė, B. Čechavičius, M. Skapas, A. Čerškus, M. Talaikis, P. Baranowski, P. Wojnar, R. Butkutė, Segregation-driven formation of bismuth quantum dots in parabolic GaAsBi/AlGaAs quantum structures, Surfaces and Interfaces **68**, 106586 (2025), https://doi.org/https://doi.org/10.1016/j.surfin.2025.106586.

[85] P. G. Eliseev, P. Perlin, J. Lee, M. Osiński, "Blue" temperature-induced shift and band-tail emission in InGaN-based light sources, Applied Physics Letters **71**(5), 569–571 (1997), https://doi.org/10.1063/1.119797.

[86] T. Wilson, N. P. Hylton, Y. Harada, P. Pearce, D. Alonso-Álvarez, A. Mellor, R. D. Richards, J. P. David, N. J. Ekins-Daukes, Assessing the nature of the distribution of localised states in bulk GaAsBi, Scientific Reports **8**(1), 6457 (2018).

[87] Y.-S. Yoo, T.-M. Roh, J.-H. Na, S. J. Son, Y.-H. Cho, Simple analysis method for determining internal quantum efficiency and relative recombination ratios in light emitting diodes, Applied Physics Letters **102**(21), 211107 (2013), https://doi.org/10.1063/1.4807485.

[88] N. Mott, Recombination; a survey, Solid-State Electronics **21**(11), 1275–1280 (1978), https://doi.org/https://doi.org/10.1016/0038-1101(78)90192-2.

[89] A. C. Espenlaub, D. J. Myers, E. C. Young, S. Marcinkevičius, C. Weisbuch, J. S. Speck, Evidence of trap-assisted Auger recombination in low radiative efficiency MBE-grown III-nitride LEDs, Journal of Applied Physics **126**(18), 184502 (2019), https://doi.org/10.1063/1.5096773.

[90] P. Ludewig, N. Knaub, N. Hossain, S. Reinhard, L. Nattermann, I. P. Marko, S. R. Jin, K. Hild, S. Chatterjee, W. Stolz, S. J. Sweeney, K. Volz, Electrical injection Ga(AsBi)/(AlGa)As single quantum well laser, Appl. Phys. Lett. **102**(24), 242115 (2013), https://doi.org/10.1063/1.4811736.

[91] M. Leszczynski, M. Micovic, C. A. C. Mendonca, A. Ciepielewska, P. Ciepielewski, Lattice Constant of AlAs, Crystal Research and Technology **27**(1), 97–100 (1992), https://doi.org/10.1002/crat.2170270118.

[92] S. Adachi, GaAs, AlAs, and $Al_xGa_{1-x}As$: Material parameters for use in research and device applications, Journal of Applied Physics **58**(3), R1–R29 (1985), https://doi.org/10.1063/1.336070.

[93] Z. L. Bushell, R. M. Joseph, L. Nattermann, P. Ludewig, K. Volz, J. L. Keddie, S. J. Sweeney, Optical functions and critical points of dilute bismide alloys studied by spectroscopic el-

lipsometry, Journal of Applied Physics **123**(4), 045701 (2018), https://doi.org/10.1063/1.5006974.

[94] J. Muszalski, A. Broda, A. Jasik, A. Wójcik-Jedlińska, A. Trajnerowicz, J. Kubacka-Traczyk, I. Sankowskaa, VECSELs emitting at 976 nm designed for second harmonic generation in the blue wavelength region, Proceedings of SPIE - The International Society for Optical Engineering **8702** (2013), https://doi.org/10.1117/12.2014757.

[95] R. Haring, R. Paschotta, A. Aschwanden, E. Gini, F. Morier-Genoud, U. Keller, High-power passively mode-locked semiconductor lasers, Quantum Electronics, IEEE Journal of **38**, 1268 – 1275 (2002), https://doi.org/10.1109/JQE.2002.802111.

[96] M. Jacquemet, M. Domenech, G. Lucas-Leclin, P. Georges, J. Dion, M. Strassner, I. Sagnes, A. Garnache, Single-Frequency CW Vertical External Cavity Surface Emitting Semiconductor Laser at 1003 nm and 501 nm by Intracavity Frequency Doubling, Applied Physics B **86**, 503–510 (2007), https://doi.org/10.1007/s00340-006-2499-0.

Author CV

Andrea Zelioli

Personal Data

Date of Birth:	1st of February, 1994
Address:	Room D202, Saulėtekio al. 3, 10257, Vilnius, Lithuania
Phone:	+370 618 56 760
Mobile:	+39 3409937692
email:	andrea.zelioli@ftmc.lt
ORCID:	0000-0001-6829-3549

Education

Postgraduate studies (PhD):

2021 – now

Joint PhD: Vilnius University & FTMC Center for Physical Sciences and Technology

Topic: "Growth and investigation of A3B5 quantum structures for VECSELs"

Supervisor: prof. dr. Renata Butkutė

Master studies (M.S):

2018 – 2020

Faculty of Physics, Informatics, and Mathematics, University of Modena and Reggio Emilia (IT)

Thesis: “Impact of GaInAs/GaAs quantum structures design on near-infrared vertical-external-cavity surface-emitting laser optical properties”
Supervisor: dr. Alberto Rota

Bachelor studies (B.S):
2013 – 2017
Faculty of Physics, Informatics, and Mathematics, University of Modena and Reggio Emilia (IT)
Tesi: “Caratterizzazione spettroscopica del processo di trasferimento di nano-ribbon di grafene dalla superficie di crescita ad un altro substrato.”
Thesis: “Characterization of the transfer procedure of graphene nano-ribbons from the growth substrate to a target one via spectroscopic techniques.”
Supervisor: dr. Roberto Biagi

Professional experience

2021 – now
Engineer, FTMC Center for Physical Sciences and Technology, Vilnius, Lithuania
Growth of A3B5 semiconductors via molecular beam epitaxy for light sources and detectors.
Device design and performance evaluation through data analysis.
Participation in scientific articles and conference papers.

2021.01 – 2021.09
R&D Engineer, Neos srl, R&D Department, Fiorano Modenese, Italy
Optimization of ink circulation via hydrodynamic calculations.

Design of electrical signals for piezoelectric print head components.
General optimization of industrial printing processes (material transport, thermal isolation, electrostatic management).

2020 – 2021

Lecturer, University of Modena and Reggio Emilia, Department of Natural Sciences, Italy
Delivered lectures on basic physics for bachelor courses in geology, natural sciences, and pharmacy.

Projects

2024 – 2025

Participation in the project "GaAsBi-based photonics solutions for hybrid photonics integrated circuits."

2024 – 2025

Participation in the project "Investigation of optical properties of bismuth quantum dots."

2022 – 2025

Participation in the project "Research Council of Lithuania A3B5 Nanostructure-Based Near Infrared Lasers 2022-2025."

2022 – 2025

COST Action "European Network for Innovative and Advanced Epitaxy," OPERA, MC member, LT.

2018 – 2020

ESA project IR Bi-based sources Irbis, Contract No. 4000122271/NL/SC.

Languages

Italian: native language

English: fluent

Spanish: intermediate (speaking, reading)

Additional information

Scholarship:

Erasmus Plus Program Scholarship (2019-2020)

Summer schools:

24th International Conference-School Advanced Materials and Technologies, 22 – 26 August, 2022, Palanga, Lithuania

25th International Conference-School Advanced Materials and Technologies, 21 – 25 August, 2023, Palanga, Lithuania

52nd International School & Conference on the Physics of Semiconductors "Jaszowiec 2024" Szczyrk, Poland, 14 - 22 June 2024

Cost action CA20116 OPERA for innovative and advanced epitaxy, training school on the physical principles and theory of advanced epitaxial growth methods, Cyprus, 25 - 27 September 2024

Awards:

Prize sponsored by 'Brolis Semiconductors' for the presentation *"Optimization of quantum well growth technology for applications in near infrared Vertical-External-Cavity Surface-Emitting-Laser"*. Open readings 2022, Vilnius, Lithuania, 15-18 March, 2022

Best oral presentations of the 14th Conference of Doctoral Students and Young Researchers FizTech2024 Oct. 2024 for the presentation: *"Fabrication of the first GaAsBi based Vertical-External-Cavity Surface-Emitting Laser for NIR "*

AI statement

During the writing of this dissertation ChatGPT was used as a tool to improve the clarity and the phrasing of certain sentences. The usual prompt used and conversation were as follows:

- Prompt: "During the writing of this dissertation ChatGPT was used as a tool to improve the clarity and the phrasing of certain sentences. Give me 3 versions which are clearer and more fluent"

- Reply: "Here are three polished alternatives, each a bit different in tone but clearer and more fluent than the original:
  “ChatGPT was used during the writing of this dissertation to enhance clarity and improve sentence phrasing.”
  “In preparing this dissertation, ChatGPT was employed as a tool to refine phrasing and improve clarity.”
  “This dissertation made use of ChatGPT to assist in improving clarity and refining the phrasing of certain sentences.”
  Would you like me to make one of them sound more neutral/technical (like a disclosure in the methods) and one more personal (like in acknowledgments)?"

NOTES

NOTES

NOTES

NOTES

Vilnius University Press
Saulėtekio al. 9, LT-10222 Vilnius
e-mail: info@leidykla.vu.lt,
www.leidykla.vu.lt
Print run copies 24